NOTE TO USERS

Experimental and Numerical Investigation of Passive Two-Phase Heat Transfer Devices for Space Applications

by

Erin MacDonald
B. Eng., Carleton University
B.Sc., Saint Mary's University

A thesis submitted to the Faculty of Graduate Studies and Research in partial fulfillment of the requirements for the degree of
Master of Applied Science

Ottawa-Carleton Institute for Mechanical and Aerospace Engineering

Department of Mechanical and Aerospace Engineering

Carleton University

Ottawa, Ontario

Canada

August 2004

PAGINATION ERROR.

ERREUR DE PAGINATION.

TEXT COMPLETE.

LE TEXTE EST COMPLET.

Abstract

An experimental investigation of the thermal performance characteristics of a loop heat pipe (LHP) was performed. A series of tests was conducted under ambient and vacuum conditions to investigate LHP characteristics during both steady-state and transient operation including start-up and constant power operation. Power cycling was performed to examine performance in both environments. LHP operation was also examined for possible temperature hysteresis behaviors during large power changes. The effects of ambient interactions on LHP performance were examined through comparison of ambient and vacuum data. A discussion of the start-up mechanism and LHP operational characteristics was provided.

A finite element numerical model for LHP simulation was developed at Carleton University using the existing MMO Framework platform. The phenomena associated with the operation of the LHP, such as the evaporation of the working fluid that provides the driving force for the operation of the loop, are largely concentrated within the evaporator section of the loop. Development of the computational LHP model described in this work therefore focused heavily on the description of the behaviors and phenomena associated with the evaporator. Descriptions of meshing techniques and solution algorithms were discussed, and the initial predictions of the LHP temperature distribution due to conduction, mass flux due to evaporation, and vapour velocity in the evaporator were also presented.

Acknowledgements

My advice to anyone writing a thesis would be to prepare the Acknowledgements section first. It is difficult to give due thanks when you find yourself at the height of crankiness. That being said I would like to thank my supervisor Professor Tarik Kaya for giving me opportunity and guidance above and beyond the call of duty.

I would also like to thank Professor John Goldak, whose knowledge and guidance made the numerical section of this work possible. Thanks also to Lijiang Bai and Stanislav Tchernov for their insight on the MMO Framework.

The Canadian Space Agency contributed heavily to the experimental portion of this work. Above and beyond their financial contribution, several people at CSA made my life a lot easier. Many thanks to Darius Nikanpour, Stéphane Lapensée, Guanghan Wang, and Dontatas Mishkinis for their time, interest, and assistance.

Finally, I owe the completion of this project and my remaining sanity to the love and support of my family and friends. Thank You.

Table of Contents

Figures

Tables

Nomenclature

ΔP_{tot}	total pressure drop across the LHP
ΔP_{groove}	pressure drop in the grooves
ΔP_{vap}	pressure drop across the vapour line
ΔP_{con}	pressure drop across the condenser
ΔP_{liq}	pressure drop across the liquid line
ΔP_{wick}	pressure drop across the wick
ΔP_{w}	capillary pressure developed by the wick
ΔP_{g}	static pressure drop across the wick due to gravity or accelerations
ΔP_{cap}	capillary pressure developed by the wick
σ	surface tension
θ	angle of contact between the liquid and the wick
$\Delta P_{cap,\max}$	maximum capillary pressure developed by the wick
R_p	pore radius
T_e	saturation temperature of vapour in the evaporator
T_{cc}	saturation temperature of the fluid in the compensation chamber
$\dot{m}$	mass flow rate

h_{fg} latent heat of vaporization

$G_{e,cc}$ thermal conductance between the evaporator and compensation chamber

C_p specific heat

R_{eff} effective thermal resistance

Q_e net heat load applied to the evaporator

N_j shape functions

[R] matrix of shape functions

k coefficient of thermal conductivity

T temperature

$\dot{Q}$ rate of internal heat production

ϕ_i Galerkin coefficients

$\{F^e\}$ element load vector

$[K^e]$ element stiffness matrix

$\{x^e\}$ element field vector

$[K]$ global stiffness matrix

$\{F\}$ flow variable for each node in the domain

$\{x\}$ flow variable for each node in the domain

h enthalpy

q heat flux

$\overline{V}_L$ liquid velocity

$\overline{V}_G$ vapour velocity

$\overline{V}_I$ interface velocity

ρ	density
$\hat{n}$	outward normal unit vector
κ	permeability of the porous material
μ	dynamic viscosity of the liquid
g	acceleration due to gravity
ϕ	potential
h_c	convective heat transfer coefficient
T_∞	ambient temperature
T_s	surface temperature

Chapter 1

Introduction

The Loop Heat Pipe (LHP) is a passive two-phase thermal transport device that uses latent heat of vaporization to accomplish heat transfer between a heat source and a lower temperature heat sink. The LHP is both self-priming and self-sustaining as its working fluid is circulated entirely by surface tension forces developed in a porous wick structure that lines a portion of the device. The LHP therefore requires no external work input, except the waste heat that it is transferring, for start up or operation. The LHP was invented in Russia in the early 1980s, and with patents on LHP designs filed in the US in 1985. Although similar to conventional heat pipes, the LHP overcomes some of the heat pipe's limitations by incorporating separate lines for the transport of liquid and vapour phases. Due to the presence of a secondary wick, the LHP can function against gravity, allowing for ground based testing of space applications.

The typical LHP contains an evaporator, compensation chamber, condenser and liquid and vapour transport lines. An illustration of a typical LHP is provided in Figure 1.1.

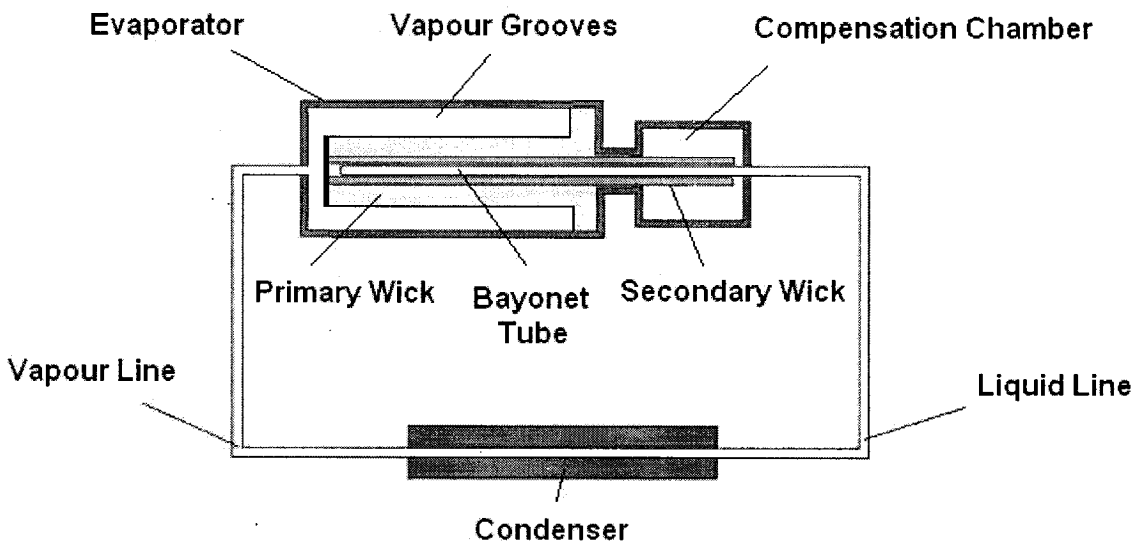

Figure 1.1: Schematic of a Typical LHP

The LHP is a sealed system charged with a working fluid, the circulation and phase change of which provide the primary mechanism for the transfer of heat across the device. The evaporator and compensation chamber are lined with a porous wicking material that links the two components both thermally and hydrodynamically. In addition to this primary wick, many LHPs contain a secondary wick to ensure that liquid is available to the evaporator at all times. The secondary wick also increases the tolerance of the evaporator to the formation of bubbles in the evaporator core. Evaporation of the working fluid may take place in the evaporator core because the sintered metal wick usually possesses a high thermal conductivity. As a result of this evaporation, vapour

pockets may be present in the core during operation. In order to prevent an accumulation of vapour within the evaporator core, the secondary wick is equipped with arteries that allow the vapour to vent to the compensation chamber. The secondary wick also provides the advantage that the loop may be started with power applied solely to the evaporator, without the need for active preconditioning (preheating) of the compensation chamber.

Typical operation of an LHP begins with application of heat to the evaporative region of the device, raising the temperature of both the evaporator and compensation chamber. The LHP starts when the temperature difference, and therefore pressure difference, between the evaporator and compensation chamber is adequate to initiate the circulation of the working fluid. Increased pressure due to the boiling of the working fluid in the evaporator pushes the vapour through grooves in the wick into the vapour line. The vapour is then forced through the vapour line to the condenser where it condenses, rejecting its latent heat of vaporization to the heat sink. The resulting liquid is then pumped back to the compensation chamber through the liquid line. The two-phase compensation chamber stores the excess working fluid and controls the operating temperature of the LHP.

1.1 Background

The LHP was developed in the early 1980's at the Laboratory of Heat Transfer Devices, Institute of Thermal Physics, Ural Branch of the USSR Academy of Sciences by a group of scientists and engineers led by Maidanik, and was patented in 1985 (Maidanik, 1985).

The first successful flight test was conducted aboard the Russian spacecraft Garant in 1989. The prototype transported a maximum heat rate of 100 W during ground

based testing, and nearly 1.4 kW in space. The prototype was concluded to be reliable in both ground and flight testing (Maidanik, 1991). Further flight testing experiments were conducted during the 1990's including the flight test of an American LHP on the STS-83 and STS-94 missions in 1997 (Lashley et al., 1998). During these flights, the LHP demonstrated perfect on orbit operation. The LHP has since been widely accepted as a baseline technology for spacecraft thermal design including that of Boeing-702 bus used for Telesat's ANIK F1 and ANIK F2 satellites.

Further experimental work conducted throughout the 1990's focused on LHP characterization. Dickey and Peterson (1994) tested an LHP and compared the results to those generated from a conventional heat pipe. Constant condenser temperature was maintained during the tests while evaporator heat input was incrementally increased. The tests were performed at sink temperatures of 0 °C and 3 °C. Evaporator position relative to the condenser was also considered. The evaporator height varied from 0 to 60 cm above the condenser during the tests. Ernst (1994) performed vacuum testing on a Soviet built LHP. The condenser was fitted with a radiator and the device was installed in a vacuum chamber, the walls of which were held at a constant temperature of -80 °C. The experiments showed a variation in temperature from the evaporator to the condenser of 5.9 °C with an input power of 25 W and a radiator temperature of 24 °C. Vacuum testing was also performed with powers reaching 120 W.

Several features of the LHP make it an attractive device for space-based applications. LHPs can transport large thermal power loads over long distances through a relatively small temperature gradient. Through active control of the compensation chamber temperature, the evaporator temperature may be maintained within a very

narrow range. LHPs can be constructed in many different shapes and sizes, and may incorporate flexible and/or very compact lightweight fluid transport lines. This characteristic is particularly beneficial for space-based applications where the design of a thermal control system may be restricted by rigorous mass and geometric constraints. Due to the presence of the secondary wick, the LHP can function against gravity, allowing for ground based testing for space applications. The LHP has gained the attention of the spacecraft thermal control community because of its attractive features including very high heat transfer density, passive operation, robustness, stable and reliable performance, and long life (Nikitkin and Cullimore, 1998).

The LHP is very closely related to another thermal control device, the capillary pumped loop (CPL). CPLs were invented in the 1960's in the US with active development beginning in the early 1980's. The CPL is composed of the same components as an LHP except that in a CPL the liquid returning from the condenser does not directly pass through the reservoir. One major disadvantage of the CPL is that it must be primed prior to start-up by heating the reservoir to a temperature higher than that of the evaporator. Unlike the CPL, the LHP starts as soon as the temperature gradient between the evaporator and compensation chamber is high enough to build up the necessary pressure difference to initiate circulation. The LHP is typically thought to be more robust than the CPL. If the returning liquid is not sufficiently subcooled, the evaporator core of the CPL will become blocked by vapour causing it to deprime. In the case of the LHP, a decrease in return liquid subcooling is balanced by an increase in operating (saturation) temperature. The LHP is therefore autoregulating and adjusts itself to maintain adequate subcooling (Nikitkin and Cullimore, 1998). Because the CPL

reservoir may be placed anywhere in relation to the evaporator, CPLs typically offer increased geometric flexibility over LHPs. Multiple evaporators can also easily be integrated into CPL design, presenting another significant advantage of the device.

With the continued drive towards smaller spacecraft and the use of miniaturized technologies including Micro-Electro-Mechanical systems (MEMS), there is a need for the transport high heat flux densities within small geometric constraints. The development of miniature loop heat pipes (MLHPs) is currently under investigation to fulfil these requirements. Pastukhov et al. (1999) investigated two ammonia/stainless steel MLHPs with 6 mm diameter cylindrical evaporators. Tests were performed under atmospheric conditions with heat removal at the sink using both free convection and forced air-cooling at ambient temperature. The first specimen possessed a heat transportation capacity of 50 W, but demonstrated unreliable start-up and operation in unfavorable orientations. The second MLHP tested was shown to provide reliable start-up and stable operation with a heat transportation capacity up to 20 W in all orientations. Pastukhov et al. (2003) published the results of an experimental investigation on the use of MLHPs for electronics applications. The study examined the integration of several prototype MLHPs into remote heat exchanger systems under various conditions including variations in tilt angle and sink cooling methods. The tests demonstrated that MLHPs with evaporator diameters less than 6mm were capable of transporting up to 80 W, proving MLHPs to be promising devices for electronics and computer cooling. Batturkin et al. (2002) studied the integration of flat evaporator or "heating wall-wick" structures into MLHPs. The study examined the heat transfer characteristics of the MLHP including the influence of applied heat flux and orientation. The experimental results

showed heat transfer capabilities up to 30 kW/m^2, stable operations in orientations against gravity, and start ups at powers below 10 W. Lin et al. (2002) investigated the use of high performance miniature heat pipes for US Air force and Space programs. The study examined the performance of MLHPs containing enhanced capillary structures constructed of a notched folded copper fin. The enhanced wick structure was shown to achieve a heat transfer coefficient up to 120% greater than traditional wicking structures, and allowed for the transfer of fluxes higher than 140 W/cm^2 in some cases.

Due to the complexity of the physical phenomena associated with the LHP, the use of numerical methods is imperative when implementing these devices within a thermal design. However, the numerical modeling of LHPs presents considerable challenges including the modeling of two-phase flows with heat transfer and phase change in porous media. As such, many past modeling efforts relied heavily on simplifying assumptions and have focussed largely on the balance of the steady state energy equation. Maidanik et al. (1994) developed a closed form pressure and energy balance based analytical model of the LHP. In this case, ambient interactions and pressure losses in the liquid line were not considered. Also, the pressure distribution in the vapour line was assumed to be linear. Dickey and Peterson (1994) developed a steady state LHP model based on energy balances across the evaporator and condenser sections. The model predicted values that were in good agreement with experimental results including average liquid temperature, average vapour temperature, and mass flow rates. Wirsch and Thomas (1996) developed a steady state two-dimensional finite element model of conduction within the evaporator section of an LHP. Delil and Baturkin (2002) developed a numerical model to determine LHP temperature and

pressure distributions based on a methodology of idealized elements, where physical components of the LHP were replaced with one or more idealized elements. The equations of continuity, energy conservation, momentum conservation, and thermal conductivity were then solved for each element using standard numerical methods.

By examining the two-phase phenomena present during LHP operation, improvements in LHP model accuracy have been attained. Hoang and Kaya (1999) developed a steady state energy balance model that incorporated correlations for two-phase pressure drop and heat transfer. The predicted results showed marked improvement over those generated using single-phase correlation, particularly at higher applied powers.

Additionally, to fully model LHP behaviour within a spacecraft, transient models are required. Transient models can be used to accurately assess LHP performance during spacecraft operating conditions including LHP start-up, LHP operation with varying evaporator or sink loads, and LHP operation with active temperature control. Wrenn and Krein (1999) developed a transient subroutine, to be integrated with a thermal solver. The ability of the model to predict the performance of the LHP under varying heat input and sink conditions was verified, with evaporator temperature predicted within 3 K of the measured operating temperature.

Increased interest in industrial LHP applications has been a major driver to implement heat pipe/LHP modeling tools in the existing commercial thermal analyzers. This interest is driving attempts by software developers to implement heat pipe/LHP modeling tools in their commercial FEM and CFD packages. Several manufacturers have already developed energy balance based models using the SINDA/FLUINT solver.

Cullimore and Baumann (2000) published work that discussed the use of the SINDA/FLUIINT solver to address the unique challenges associated with the numerical modeling of LHPs; including the modeling of two phase flows with heat transfer, simulating the effects of noncondensible gasses, capillary flow modeling, and phase interface tracking. The software was determined to be capable of predicting of both steady state performance and start up transients; however, the use of the SINDA/FLUINT package requires extensive knowledge of LHPs and the thermal-physical processes associated with them. Simpler "off the shelf" models may be required to assist potential LHP users. Cullimore and Johnson (2003) presented a procedure whereby 1D CAD methods can be used to rapidly generate 1D heat pipe and cooling loops components within a 3D thermal model generated by commercial FEM and/or CFD packages.

1.2 Applications

The use of LHPs as the primary elements thermal control systems for both space and electronics applications is expected to rise steadily. In the near future, LHPs may be used in a myriad of ground applications, including aircraft anti-icing systems, electronics cooling, emission reduction schemes for automobile engines, and solar power applications.

The LHP technology lends itself particularly well to spacecraft thermal control. With the continued drive towards smaller spacecraft and miniaturization technologies, there is a need to transport an ever-increasing heat flux density and variable heat loads with autonomy in thermal control of spacecraft. The use of LHPs will allow for the development of thermal control systems with decreased cost and reduced mission risk.

LHP technology may also enable further innovation in spacecraft thermal control such as the use of deployable radiators, and chemisorption cooling techniques. The LHP offers an interesting thermal control solution for spacecraft carrying multiple payloads such as CASSIOPE.

1.3 Objectives

This thesis presents an experimental and numerical investigation of two-phase heat transfer devices. Specifically, the work focuses on the LHP, and contrasts this technology with similar two phase heat transfer devices including the heat pipe and the capillary pumped loop. The objectives of the study were to gain an overall understanding of LHP technology as well as the ability to numerically simulate LHP behavior during normal operation. Three primary activities were targeted to achieve this goal:

1. Establishment of an LHP laboratory
2. Performance testing of a breadboard LHP
3. Preliminary development of a computational LHP model

Testing of the breadboard LHP was performed in both ambient and thermal vacuum environments and sought to identify the critical performance issues including:

1. Performance of heat transport capabilities
2. Unsteady state heat transfer and power cycles
3. Start-up transients
4. Presence of temperature hysteresis behaviors
5. Effects of ambient interactions on LHP performance

A finite element numerical model for LHP simulation was developed at Carleton University using the existing MMO Framework platform. The task of numerically modeling LHPs presents considerable challenges including the modeling of two-phase flows with heat transfer and phase change in porous media; the realization of which lie well beyond the scope of a Masters thesis. The modeling efforts presented in this study were therefore heavily focused on the evaporator section of the LHP, providing the foundation for a future detailed LHP model. Overtime the requirements of the LHP model will be redefined with respect to the current state of the art. As such, the model will develop in complexity and sophistication in later stages of work.

1.4 Organization

This thesis presents an experimental and numerical investigation of two-phase heat transfer devices, including heat pipes, capillary pumped loops, and LHPs, and is organized as follows:

Chapter 1 Introduction: Introduces the LHP concept and compares the device with similar two phase heat transfer technologies including heat pipes and capillary pumped loops. Also provides a brief history of the subject, and presents the scope of the thesis.

Chapter 2 Theory: Presents the basic principles and characteristics of LHP operation.

Chapter 3 Experimental Investigation of LHP: Provides details of the experimental investigation, including a description of the test specimen, test set-

ups, and experimental procedures. Results from both ambient and vacuum testing are presented and discussed.

Chapter 4 Computational LHP model: Presents basic theory of the finite element method for heat transfer, and introduces the MMO framework and solvers used in the numerical model. This chapter discusses the creation of an evaporator based LHP model and presents the predicted results.

Chapter 5 Conclusions and Recommendations: Presents the conclusions of the thesis and discusses future work

Chapter 2

Loop Heat Pipe Theory

2.1 Heat Pipe Operation

Like the LHP, heat pipes are passive thermal control devices that transmit heat from one location to another through a small temperature gradient. A typical heat pipe consists of a closed tube of arbitrary cross section whose inner surface is lined with a porous wicking material. The pipe contains a two phase working fluid, the liquid phase saturating the porous wick, and the vapour phase occupying the hollow inner core. A typical heat pipe is illustrated in Figure 2.1.

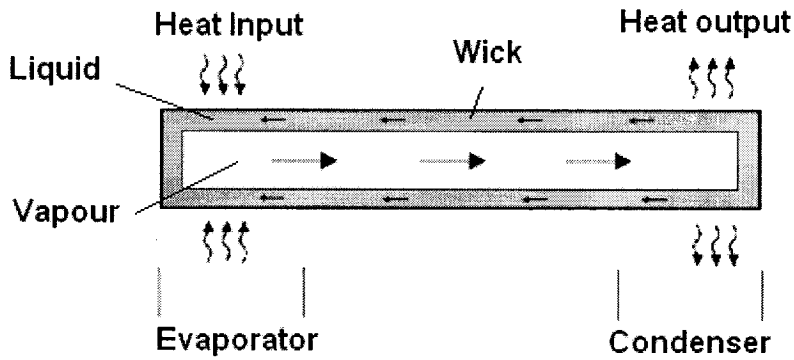

Figure 2.1: Schematic of a Typical Heat Pipe

External heat is applied at the evaporator end of the pipe, and the working fluid in this section is vaporized. The pressure difference resulting from the addition of vapour to one end of the core drives the vapour to the opposite end where it condenses and the latent heat of vaporization is transferred to the sink. Because liquid is removed from the wick in the evaporator, the liquid vapour interface enters the wick in that section of the pipe resulting in the development of capillary pressure that pumps the liquid through the wick towards the condenser. This phenomenon is illustrated in Figure 2.2.

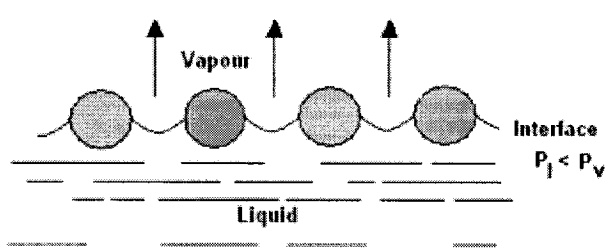

Figure 2.2: Development of Capillary Pressure

The amount of heat transferred through latent heat is often several times larger than the heat that may be transferred through conduction or by a typical convection system. Heat pipe characteristics are dependant on size, shape, working fluid, and heat transfer rate. Additionally, heat pipes also possess several characteristic dependant heat transfer limitations. These characteristics and limitations play an important role in the analysis, design and implementation of heat pipes.

Along with the design characteristics of a heat pipe, the operating conditions to which it is subjected determine its ability to transport heat. Several additional factors limit the circulation of fluid within a heat pipe thereby limiting the heat transport capability of the device. These include: capillary pumping ability (capillary limitation), chocking of vapour flow (sonic limitation), removal of liquid at the vapour-liquid interface due to high velocity vapour (entrainment limitation), and the disruption of liquid flow in the wick due to the presence of vapour pockets (boiling limitation) (Chi, 1976).

The vapour phase of the working fluid flows continuously from the evaporator to the condenser while the liquid phase flows continuously from the condenser to the evaporator during steady state operation of the heat pipe. There exist therefore pressure gradients along the vapour and liquid passages. The capillary pressure developed within a heat pipe is caused by a pressure difference between the vapour side and the liquid side of the vapour-liquid interface established by the menisci that form there (Chi, 1976). If a certain maximum capillary pressure is exceeded, more liquid leaves the wick at the evaporator than enters the wick at the condenser leading to wick dryout, and the heat pipe will cease to function. The capillary limit is therefore a limit on the liquid velocity within the wick.

The sonic limitation of a heat pipe can be understood by first recognizing the similarity of the flow in a heat pipe to that in a convergent-divergent nozzle. While velocity variations in a nozzle result from a constant mass flux through a channel of variable cross sectional area, velocity variations in a heat pipe result from a variable mass flux through a (typically) constant cross-sectional area (Chi, 1976). In conventional heat pipe operation, the heat flux carried by the pipe, and subsequently the vapour velocity, may be increased by increasing the heat rejection rate at the condenser. At a certain rejection rate the vapour velocity becomes sonic and the flow is chocked. Further increases in the heat rejection rate from the condenser does not increase the total heat flux but only reduces the temperature of the condenser. The sonic limit is therefore a limit on the vapour velocity in the core.

A shear force exists at the liquid-vapour interface because the vapour and liquid are moving in opposite directions. If the vapour velocity is high enough, the shear force may cause the liquid to be torn from the wick and entrained in the vapour flow causing dryout of the wick (Chi, 1976). The maximum vapour velocity achieved before the onset of entrainment is therefore known as the entrainment limitation.

The boiling limitation is reached when pockets of vapour form in the evaporator section of the wick, impeding the radial heat flux through the wick. These pockets form because the vapour saturation temperature at the liquid-vapour interface is greater than the liquid temperature at the same point. Because this temperature difference increases with increased heat flux, the radial heat flux conducted through the wick in the evaporation section is limited by the boiling limitation.

2.2 LHP Operating Principles

2.2.1 LHP Operation

The start-up and operation of the LHP require that the wick develop adequate capillary pressure to overcome the total pressure drop across the loop. The total pressure drop across the loop is defined as the sum of the frictional drops in the vapour grooves, vapour line, condenser, liquid line, evaporator wick, as well as any static pressure drop caused by gravity and or accelerations:

$$\Delta P_{tot} = \Delta P_{groove} + \Delta P_{vap} + \Delta P_{con} + \Delta P_{liq} + \Delta P_{wick} + \Delta P_g \tag{2.1}$$

where:

ΔP_{tot} is the total pressure drop across the LHP

ΔP_{groove} is the pressure drop in the grooves

ΔP_{vap} is the pressure drop across the vapour line

ΔP_{con} is the pressure drop across the condenser

ΔP_{liq} is the pressure drop across the liquid line

ΔP_{wick} is the pressure drop across the wick

ΔP_g is the static pressure drop across the wick due to gravity or accelerations

One of the advantages of the LHP, or any capillary loop, is that the meniscus inside the wick automatically adjusts itself and establishes a pressure head equivalent to the total pressure drop, including losses, across the LHP. The pressure that the wick can develop is inversely related to the radius of curvature of the menisci and is given by:

$$\Delta P_{cap} = 2\sigma \frac{\cos\theta}{R} \tag{2.2}$$

where:

ΔP_{cap} is the capillary pressure developed by the wick

σ is the surface tension of the working fluid

θ is the angle of contact between the liquid and the wick

Figure 2.3 illustrates a meniscus inside a cylindrical pore of radius R_p.

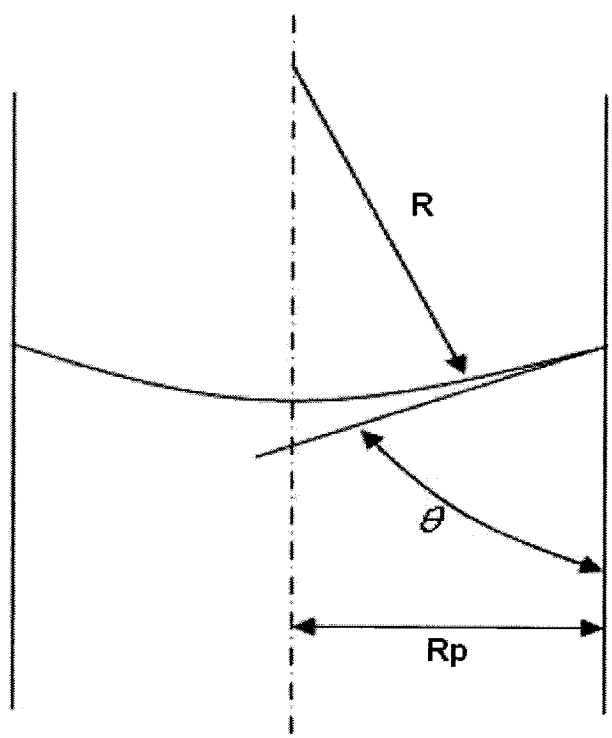

Figure 2.3: Meniscus in a Cylindrical Pore (Bai, 2004)

As the heat load applied to the evaporator increases, the mass flow rate of the working fluid through the loop and the total pressure drop of the system also increase. As a result, the radius of curvature of the menisci decreases and a higher capillary pressure is developed to balance the increased pressure drop. With increasing heat loads, the radius of the menisci will continue to increase until it equals the radius of the wick pores, and the maximum capillary pumping capacity of the wick is reached:

$$\Delta P_{cap,\max} = 2\sigma \frac{\cos\theta}{R_p} \tag{2.3}$$

where:

$\Delta P_{cap,\max}$ is the maximum capillary pressure developed by the wick

R_p is the pore radius of the wick

If the heat load is further increased, the capillary pressure will no longer balance the pressure drop across the loop and the LHP will deprime. Therefore, for continued operation of the LHP the following condition applies:

$$\Delta P_{tot} \leq \Delta P_{cap} \tag{2.4}$$

2.2.2 LHP Thermohydraulics

The pressure gradient between the evaporator and the compensation chamber provides the driving force for the circulation of the working fluid. For the operation of the LHP the following condition must be satisfied:

$$\Delta P_{tot} - \Delta P_w = \left(\frac{dP}{dT}\right)(T_e - T_{cc}) \tag{2.5}$$

where:

ΔP_w is the capillary pressure developed by the wick

T_e is the saturation temperature of vapour in the evaporator

T_{cc} is the saturation temperature of the fluid in the compensation chamber

$\left(\frac{dP}{dT}\right)$ is the slope of the saturation line at T_{cc}

Equation (2.5) states that for a given pressure between the evaporator and compensation chamber, there must exist a corresponding temperature difference between the two components.

The thermal and hydraulic processes involved in LHP operation may be better understood through a simple thermodynamic analysis of a typical LHP. Figure 2.4 illustrates the pressure-temperature diagram of steady-state LHP operation.

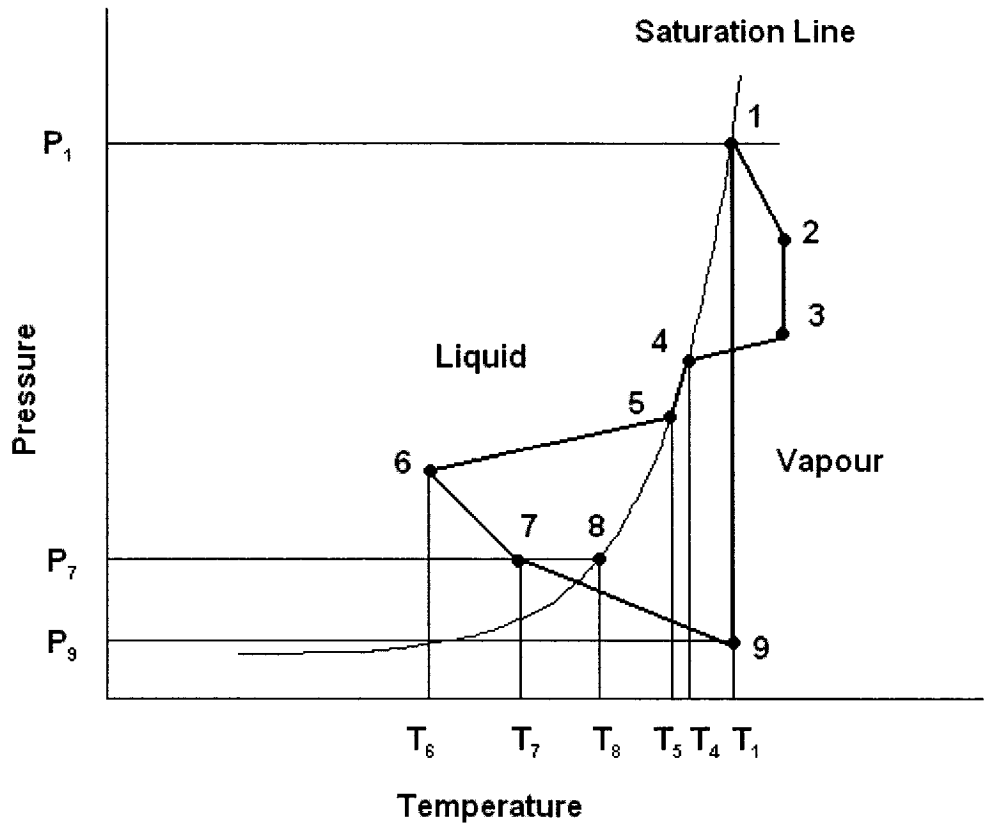

Figure 2.4: P-T Diagram of Steady-state LHP Operation (Adapted from Ku, 1999)

The cycle begins as liquid evaporates at the outer surface of the wick; the working fluid is therefore saturated (point 1). Due to heating and a loss in absolute pressure, the vapour becomes super-heated as it is pushed along the wick through the vapour grooves towards the vapour line (point 2). Although the pressure of the vapour decreases as the vapour passes through the vapour line to the condenser, its temperature remains constant (assuming that the vapour line is perfectly insulated). The vapour therefore becomes increasingly superheated (relative to the local saturation condition) until it reaches the entrance of the condenser (point 3). While inside the condenser, the vapour cools to

saturation and begins to condense (point 4). Both pressure and temperature decrease as the fluid condenses. Point 5 marks the end of condensation. Depending on the location of the interface within the condenser, the fluid may be subcooled as it travels through the condenser to the liquid line (Point 6). Depending on weather the liquid gains or looses heat to the ambient, the temperature of the liquid may increase, decrease, or remain constant as it travels through the liquid line to the evaporator core (Point 7). Because there is no exchange of fluid between the compensation chamber and the evaporator core during steady-state operation, the saturation pressure in the compensation chamber must be equal to T_7. The compensation chamber is noted on Figure 2.4 as Point 8. Equation (2.5) can now be rewritten as:

$$P_1 - P_8 = \left(\frac{dP}{dT}\right)(T_1 - T_8) \tag{2.6}$$

where:

P_1 is the saturation pressure in the vapour grooves

P_8 is the saturation pressure in the compensation chamber

T_1 is the saturation temperature of vapour in the evaporator

T_8 is the saturation temperature of the fluid in the compensation chamber

$\left(\frac{dP}{dT}\right)$ is the slope of the saturation line at T_8

The derivative (dP/dT) is related to the physical properties of the working fluid through the Clausius-Clapeyron equation:

$$\frac{dP}{dT} = \frac{h_{fg}}{T_8 \Delta v} \tag{2.7}$$

where

h_{fg} is the latent heat of vaporization of the working fluid

T_8 is the saturation temperature of the fluid in the compensation chamber

Δv is the difference between vapour and liquid specific volumes

Therefore, for a given pressure difference between the evaporator and compensation chamber, there must be a corresponding difference in the saturation temperatures of the two components. When external conditions change, the locations of points 1 and 8 may shift along the saturation line until a new equilibrium (satisfying equations (2.1) through (2.5)) is achieved. This determines the operating temperature of the LHP (Ku, 1999).

2.3 LHP Operating Characteristics

2.3.1 Loop Operating Temperature

The temperature of the compensation chamber is a function of evaporator heat load, sink temperature, as well as the ambient effects on the liquid line; and is the primary condition that affects the operating temperature of the loop. The compensation chamber is located adjacent to the evaporator. The primary or secondary wick links the two components thermally and hydrodynamically, and the working fluid passes through the compensation chamber as it returns from the condenser to the evaporator. The temperature of the compensation chamber therefore is primarily related to the operating temperature of the evaporator and the enthalpy of the liquid returning from the condenser. A simplified thermal network of a typical LHP is illustrated in Figure 2.5.

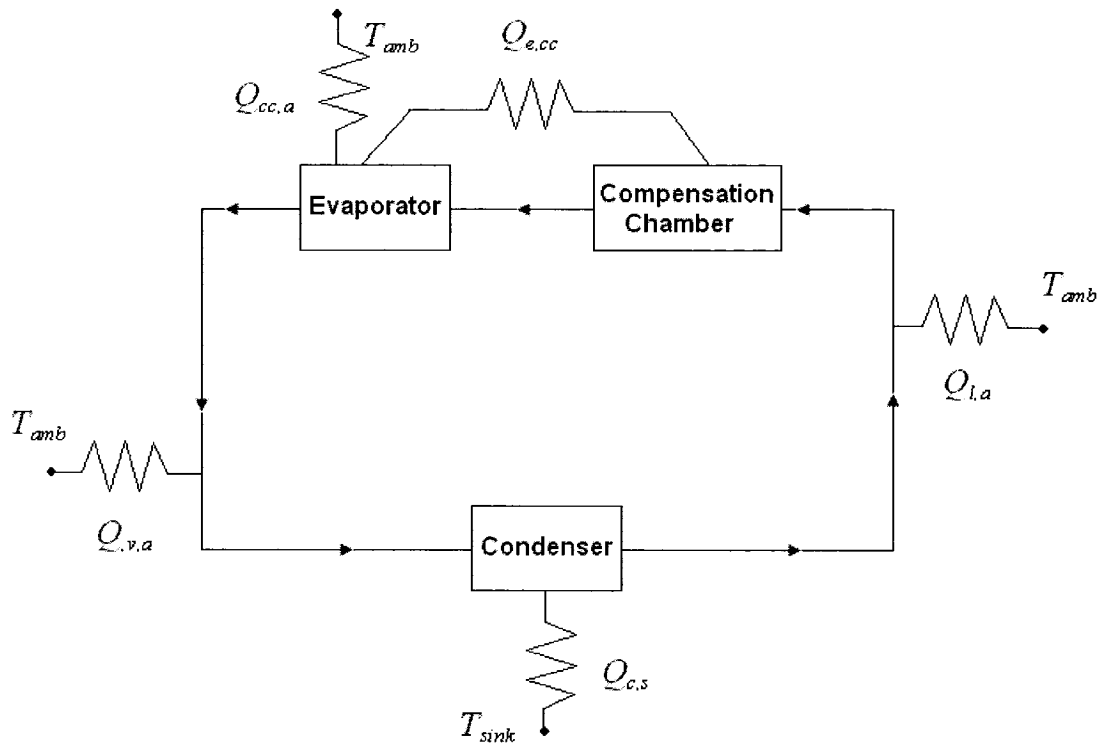

Figure 2.5: Thermal Network Diagram of Typical LHP (Adapted from (Ku, 1999))

There is an exchange of energy between the compensation chamber and the evaporator, surroundings, and the returning liquid. When heat is applied to the evaporator, part of the heat vaporizes the working fluid, and part of the heat is exchanged with the compensation chamber:

$$Q_e = Q_{e,cc} + Q_{e,evap} \tag{2.8}$$

where:

Q_e is the net heat load applied to the evaporator

$Q_{e,evap}$ is the heat absorbed during the vaporization of the working fluid and is defined as follows:

$$Q_{e,evap} = \dot{m}h_{fg} \tag{2.9}$$

where:

$\dot{m}$ is mass flow rate

h_{fg} is latent heat of vaporization

The heat transfer from the evaporator to the compensation chamber is known as heat leak and is given by:

$$Q_{e,cc} = G_{e,cc}(T_e - T_{cc}) \tag{2.10}$$

where:

$G_{e,cc}$ is the thermal conductance between the evaporator and compensation chamber

T_{cc} is the temperature of the compensation chamber

T_e is the evaporator temperature

This internal heat leak occurs through two mechanisms. When the evaporator core is completely liquid filled, the heat travels to the compensation chamber through conduction, and the thermal conductance is relatively small. If vapour is present within the evaporator, this convective heat transfer is enhanced by evaporation and condensation of the fluid within the vapour arteries of the secondary wick, and the thermal conductance becomes relatively large. Under this condition, the secondary wick acts much like a conventional heat pipe as heat is transferred from the evaporator to the compensation chamber. This is the primary mechanism for heat leak, and the evaporator heat load directly affects the quantity of heat leaked to the compensation chamber.

Heat exchange can also occur between the compensation chamber and the surroundings via convection and/or radiation (and is sometimes applied through active

means e.g. a control heater/starter heater). Through fluid mixing, the enthalpy of the liquid returning from the condenser can also affect the temperature of the compensation chamber. Assuming that the environmental affects on the compensation chamber are negligible, the heat leaked to the compensation chamber must be balanced by subcooled liquid returning from the condenser for steady state operation. The following condition must therefore apply:

$$Q_{e,cc} = \dot{m}C_p\Delta T = \dot{m}C_p(T_{cc} - T_{in}) \tag{2.11}$$

where:

C_p is the specific heat of the liquid

ΔT is the subcooling of the returning liquid

T_{cc} is the temperature of the compensation chamber

T_{in} is the temperature of the liquid at the entrance to the compensation chamber

The temperature of the liquid as is travels through the liquid line from the condenser to the compensation chamber is typically influenced by the ambient surroundings. The temperature difference caused by heat exchange between the liquid and the surroundings is expressed as:

$$T_{in} - T_c = \frac{Q_{l,a}}{\dot{m}C_p} \tag{2.12}$$

where:

T_c is the temperature of the liquid as it exits the condenser

$Q_{l,a}$ is the heat exchanged between the liquid and the surroundings

$\dot{m}$ is the mass flow rate of liquid through the liquid line

Because of the link between the evaporator and the compensation chamber, the LHP operating temperature is highly dependant on the enthalpy of the liquid returning from the condenser. As seen from equation (2.12) the heat exchange between the liquid and the surroundings is inversely proportional to the mass flow rate. At lower power loads, the condenser is only partially active and the mass flow rate of fluid through the liquid line is relatively small. As a result, the heat exchange between the liquid traveling through the liquid line and the surroundings is relatively large, and the temperature of the liquid as it enters the compensation chamber (T_{in}) is therefore close to the ambient temperature. This decrease in subcooling causes an increase in compensation chamber temperature. Therefore, at lower powers the LHP may actually operate at a higher temperature. As the power load is increased, the mass flow rate increases and the heat exchange between the liquid and the surroundings decreases, resulting in a lower compensation chamber temperature. This trend continues until the condenser is fully active and the operating temperature reaches a minimum. In this low power range, the LHP is said to operate in variable conductance mode. Above this point, the condenser is fully active, and cannot dissipate more heat when the load is increased. As a result, warmer liquid flows back to the compensation chamber and the operating temperature increases. In this range, the operating temperature increases almost linearly with applied power and the LHP is said to operate in fixed conductance mode. The transition from variable to fixed conductance modes is dependant on the sink temperature and the thermal coupling between the LHP and the environment. Depending on these factors, the both modes may or may not be present during the operation of the LHP (Ku, 1999).

2.3.2 Start-up

LHP start-up depends on the design of the compensation chamber and evaporator, the heat load applied to the evaporator as well as the operating conditions prior to start-up. In addition to these factors, the initial state of the working fluid inside the evaporator greatly influences LHP start-up. If liquid fills the vapor grooves, a liquid superheat will be required to initiate boiling; while if vapor fills the grooves, evaporation my commence as soon as power is applied to the evaporator. If the evaporator core is filled with liquid, the heat exchange between the evaporator and the condenser is relatively small as the heat is transferred through conduction alone. However, if there is vapor in the core, the core acts as an extension of the compensation chamber and heat is readily exchanged from the evaporator to the compensation chamber (Ku, 1999).

There are four possibilities for the state of fluid inside the evaporator depending on whether the core and grooves are liquid or vapor filled prior to start-up. These scenarios are illustrated in Figure 2.6.

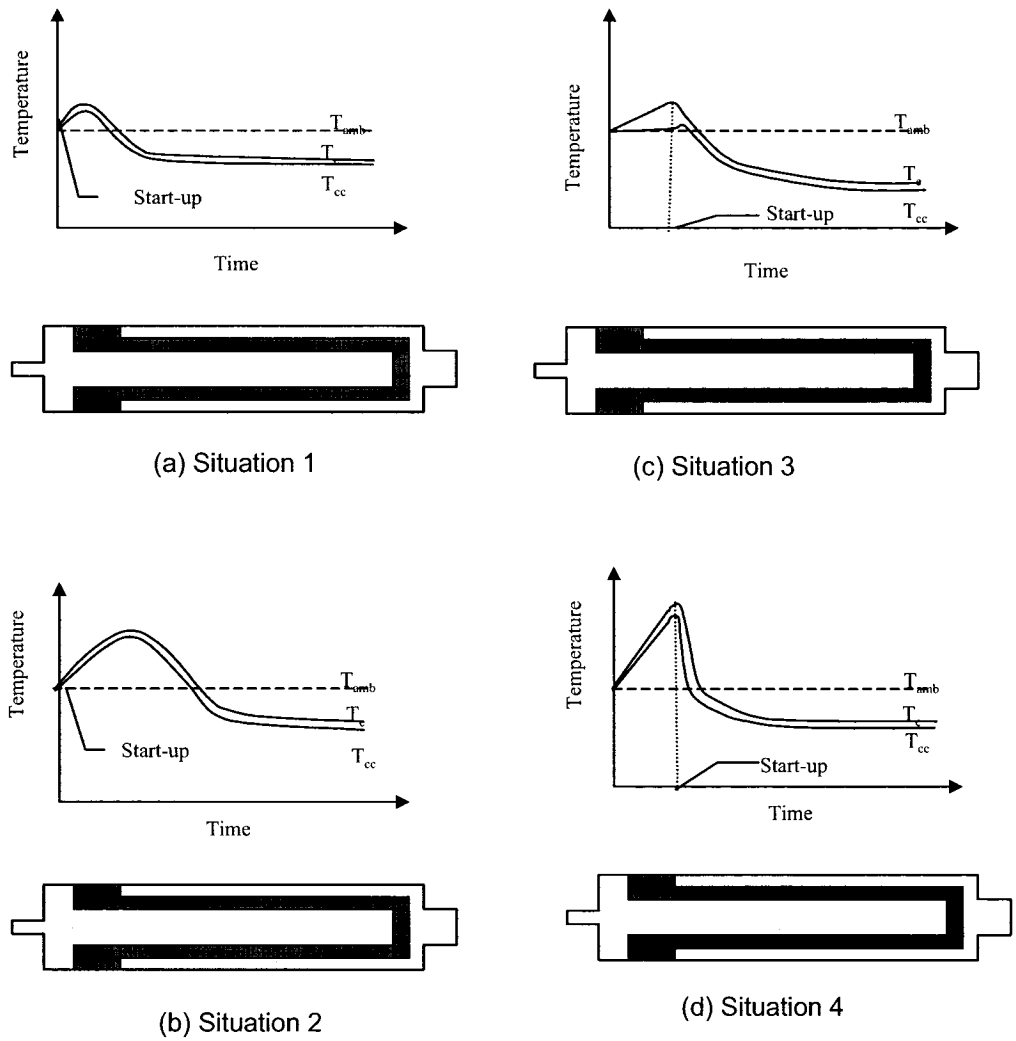

Figure 2.6: LHP Start-up Scenarios (Ku, 1999)

The situation in which vapor exists in the vapor grooves and liquid fills the evaporator core (a) represents the best-case scenario for start-up. In this case, evaporation will begin as soon as there is an application of heat to the evaporator as no superheat is required. The presence of liquid in the core minimizes the heat leak from the evaporator to the compensation chamber. Some time after start-up, the cool liquid from the condenser will

reach the compensation chamber and the temperature of the evaporator will gradually decrease before reaching equilibrium.

If there is vapor present in both the grooves and core (b), evaporation will start immediately with the application of power as in the previous case. However, the vapor in the evaporator core allows for a much larger heat exchange between the evaporator and the compensation chamber. In this case, the temperature of the evaporator and compensation chamber continue to increase after start-up until cool liquid from the condenser can compensate for the heat leak.

When liquid fills the vapor grooves, a superheat of the liquid is required to initiate nucleate boiling and initiate start-up. If liquid fills the evaporator core, the heat leak to the compensation chamber will be small and the temperature of the compensation chamber remains close to ambient temperature (c). After start-up, the evaporator temperature drops sharply and the temperature of the compensation chamber begins to control the loop.

The case in which liquid fills the vapor grooves while vapor fills the core represents the least advantageous start-up scenario (d). A liquid superheat is required to initiate start-up, and the vapor present in the evaporator core allows for a relatively high heat exchange from the evaporator to the compensation chamber. The temperature of the compensation chamber therefore rises steadily as the evaporator is heated. If the temperature of the liquid rises faster than that of the reservoir, the required superheat can be achieved and boiling is initiated starting the LHP. Otherwise, if the superheat is not achieved, the loop will never start. This situation is characterized by a steady increase in both the evaporator and compensation chamber temperatures followed by a rapid

temperature drop if the LHP starts successfully. If the LHP does not start, the temperatures will continue to increase until the applied heat load is dissipated to the surroundings through convection and radiation.

Because small and miniature LHPs are designed for applications involving low heat loads, starter heaters are sometimes employed to ensure start-up. However, such components increase the complexity and reduce the reliability of the thermal system. Additionally, for space applications, power for a starter heater may not be readily available. It is therefore advantageous that an LHP possess start-up capabilities at even very low power levels (Kaya and Ku, 2003).

2.3.4 Temperature Hysteresis

Past experimental investigations have reviled that LHP operating temperature depends on the recent history of applied power even when all other conditions, e.g. ambient temperature and sink temperature, remain unchanged. This phenomenon is referred to as temperature hysteresis. Occurrences of hysteresis behaviors in LHP operation could limit LHP applications because there may be a difference operating temperature at a given applied power despite constant ambient and sink conditions (Kaya and Ku, 1999).

Temperature hysteresis is typically associated with large decreases in applied power and is thought to be closely related to the void fraction in the evaporator core. As power is decreased, the vapor-liquid interface may move towards the entrance of the condenser, and liquid will be from the compensation chamber through the secondary wick. During small to moderate decreases in power, only liquid is supplied via the secondary wick. However, during large decreases in power, the pressure required to transport the liquid from the compensation chamber to the condenser may exceed the

capillary limit of the secondary wick. This may cause a partial dry-out of the secondary wick where by one or more vapor bubbles may become trapped within the secondary wick. As previously discussed, the presence of vapour in the significantly increases the heat leak from the evaporator to the compensation chamber, increasing the overall operating temperature of the LHP.

Chapter 3

Experimental Investigation of LHP Characteristics

3.1 Test Specimen

The LHP examined in this work was constructed by TAIS, Russia. It contained ammonia as a working fluid and consisted of stainless steel evaporator and condenser housings, surrounded by aluminum saddles. The evaporator had a total length of 200 mm and the condenser had a total length of 250 mm. The compensation chamber was also constructed of stainless steel and was linked to the evaporator. Two separate fluid transport lines connected the evaporator and condenser and were constructed of 3 mm outer diameter and 2 mm inner diameter stainless steel tubing, and had a total length of 500 mm each. The centre of each fluid line was wound in a coil to allow structural flexibility when transporting and handling the test unit.

The evaporator contained a sintered nickel primary wick with an effective pore radius of 0.9 microns. Axial grooves linked by several circumferential groves were present in the outer surface of the wick to allow for the transportation of vapour through the evaporator. A secondary wick linked the evaporator to the compensation chamber contained a network of arteries to allow vapour formed within the evaporator core to vent to the compensation chamber. Further details on the composition and structure of the wicks were not provided by the manufacturer as this information was deemed proprietary.

The total volume of the LHP was approximately 37 cc and it had a total mass, including charge, of approximately 330 g. Data provided by the manufacturer suggested maximum and minimum operational temperatures of 70 °C and -20 °C respectively, and a maximum transport capability of 400 W with a level orientation during ambient operation. Figures 3.1(a) and 3.1(b) show a photograph and schematic of the test-unit.

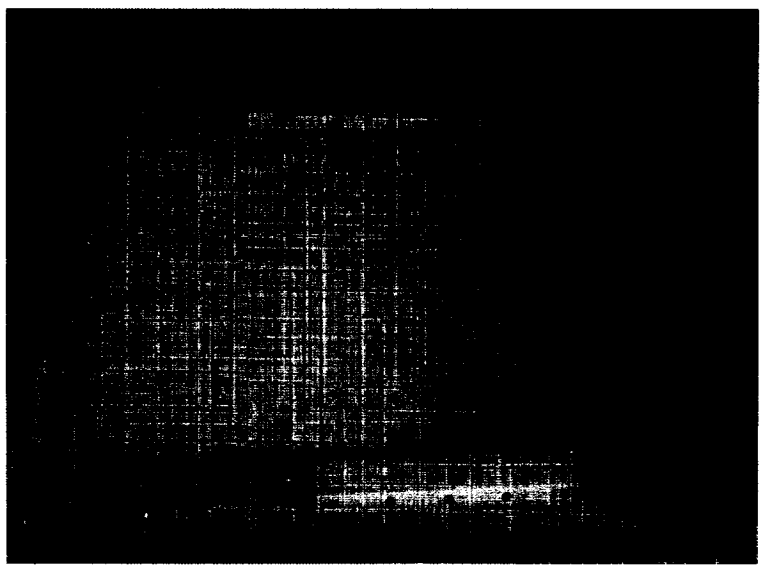

Figure 3.1(a): Photograph of TAIS Test Unit

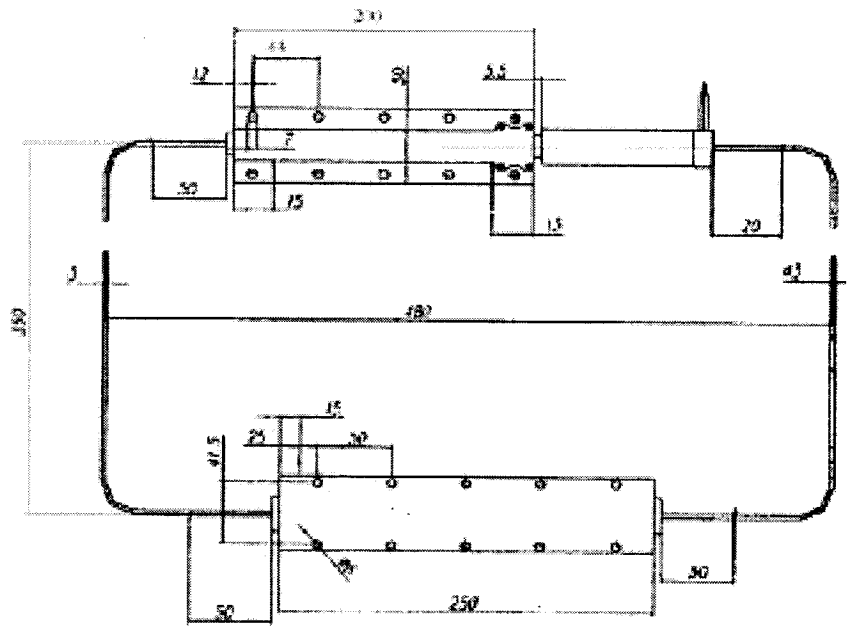

Figure 3.1(b): Schematic of TAIS Test Unit (Manufacturer's Data)

3.2 Experimental Set-up

All tests were performed using a test platform assembled at the Canadian Space Agency Thermal Technologies and Materials Laboratory at the John H. Space Centre in St. Hubert, Quebec. The test platform was assembled for the purpose of LHP characterization and is described in the following sections.

3.2.1 Evaporator Heating

In order to simulate the heat normally applied to (and transferred by) the LHP, a 500 W electric cartridge heater was used. A copper saddle was constructed to the house the heater and serve as a means of fixing the heater to the evaporator saddle. A silicone thermal epoxy was used between the heater and the saddle to facilitate conduction. The copper heater block also provided a small amount of thermal mass and the high thermal

conductivity of copper ensured a uniform heat flux was applied to the evaporator. The heater block was fixed to the evaporator saddle using ten steel bolts were tightened to 65 in-lb to achieve a uniform surface contact. A Calgraph carbon gasket was placed between the two components to reduce contact resistance and increase thermal conductivity across the joint. Power was applied to the heater using an Agilent 6035 high voltage power supply, and it was estimated that the uncertainty in applying the power to the heater was less than +/- 1%.

3.2.2 Condenser Cooling

In many cases, particularly for space applications, active cooling of the condenser region is not necessary for LHP operation. The TAIS LHP examined in this study was capable of operating with a condenser cooled only by free convection (assuming a suitable ambient condition); however, it was necessary to actively cool the condenser section of the LHP in order to perform tests over a range of applied powers and operating temperatures. An existing aluminum base plate installed in the vacuum chamber was used as a sink for the LHP condenser. To regulate the sink temperature, a Kinetics RC311 ultra low temperature chiller was used to circulate refrigerant in lines below the plate. The sink plate temperature was maintained within +/- 0.5 ^{o}C during chiller operation.

3.2.3 Test Frame

An aluminum test frame was constructed to support the LHP during testing and to serve as an interface between the condenser saddle and the sink plate. The condenser saddle was supported by an aluminum riser that allowed heat to be dissipated from the condenser to the sink. Four low conductivity Ultem posts supported the evaporator saddle and isolated it from the interface. A large aluminum interface plate supported the posts and riser and allowed for connection to the sink. To maximize thermal conductivity

between the condenser and the sink, Calgraph carbon gaskets were used in all joints between the two components. A schematic of the test frame is provided in Figure 3.2.

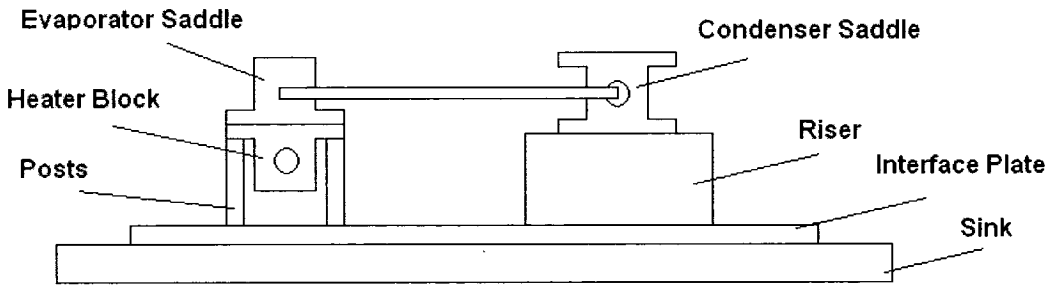

Figure 3.2: Schematic of Test Frame

The performance of the LHP is strongly affected by the level of the evaporator from end to end (tilt). To a lesser extent, performance is affected by the height of the evaporator with respect to the condenser (level). It was therefore imperative that the LHP or its frame be leveled accurately. The test frame was designed such that the axis of the evaporator was situated at the same elevation as the axis of the condenser. It was estimated that this level was achieved within +/- 1.0 mm. To ensure that there was minimal gravitational contribution to the pressure gradient across the wick, the evaporator and compensation chamber were levelled from end to end within +/- 2.0 mm, by adjusting the level of the sink plate. As such, the test frame provided adequate and accurate support for level testing; however the frame did not allow for testing at various tilts and elevations.

3.2.4 Insulation and Shielding

Insulation and Kapton were used to control ambient interactions and parasitic heating/cooling during testing. Because the gap between the heater block and the cooled

interface plate was identified as a region with a high potential for radiative heat transfer, a sheet of Kapton MLI was placed in this location.

In the ambient environment, the whole of the LHP, including evaporator, condenser, and fluid lines, was insulated against convective interactions with the surroundings using 1/2" NOMEX insulation. Care was taken to insulate the LHP components separately so as to reduce any external heat paths between them. Figure 3.3 shows a photograph of the LHP prepared for ambient testing.

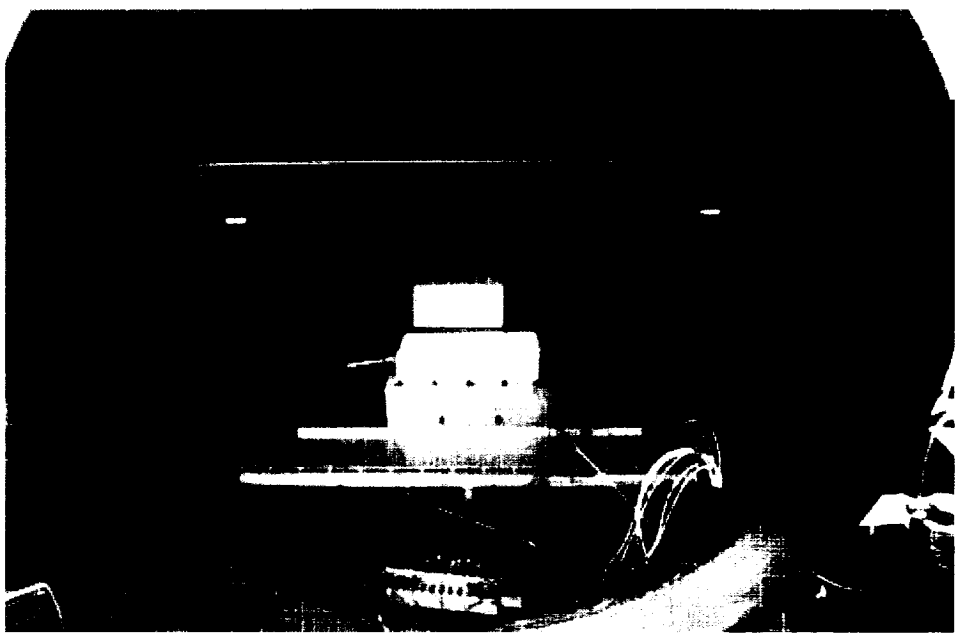

Figure 3.3: LHP Prepared for Ambient Testing

During vacuum testing, the NOMEX insulation was removed, and the LHP was covered with Kapton MLI to prevent radiative heat transfer between the test specimen and the inner wall of the chamber. A small sheet of MLI was wrapped around the heater/evaporator assembly. A single sheet of MLI was then applied over the test-set up. No MLI was applied between the LHP and the cooled interface plate.

3.2.5 Vacuum Chamber

The vacuum chamber employed in these tests was cylindrical with a length of 1.20 m and a 1.05 m diameter, and possessed a pumping system capable of maintaining a pressure of 10^{-5} torr. The chamber did not contain a thermally controlled shroud; therefore the walls of the chamber remained near ambient temperature during testing. The chamber contained a support frame for the chiller-cooled sink plate. Vacuum feed-through valves where used to allow connections with the heater, thermocouples, and chiller lines inside the chamber.

3.2.6 Instrumentation

Sixteen T-type copper/constantan thermocouples were used to monitor the LHP temperatures, ambient temperature, and the temperature of the heat sink (or cooling fluid) during testing. The thermocouples were placed at critical locations on the LHP using Kapton and aluminium tapes. Four thermocouples were placed on the evaporator, and three thermocouples each were placed on the vapour line, liquid line, condenser, and compensation chamber. The precision of the thermocouples was estimated to be +/- 0.5 ^{o}C, and their locations are illustrated in Figure 3.4.

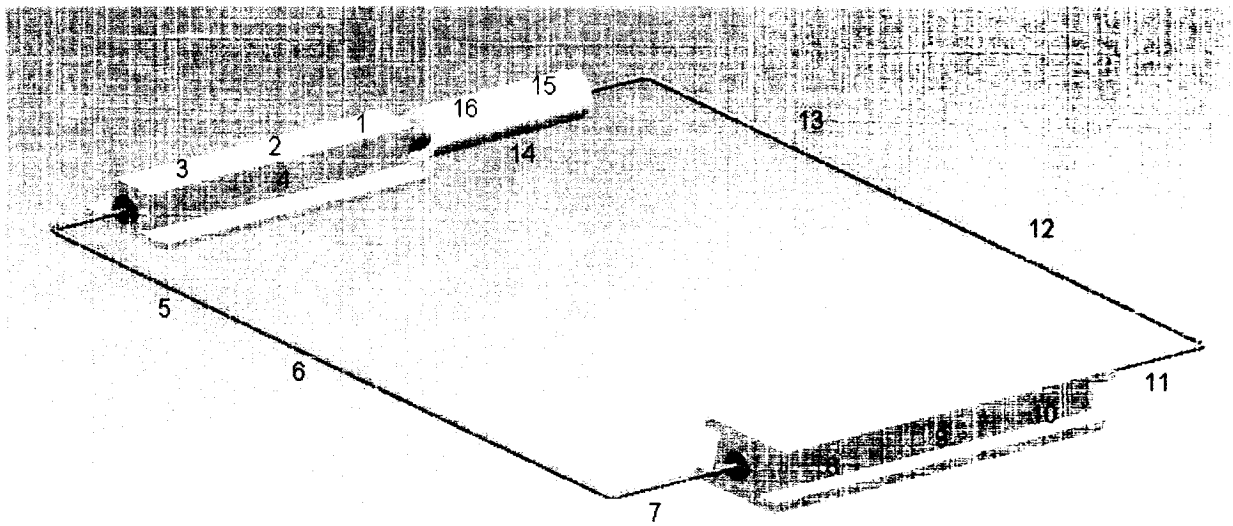

Figure 3.4: Thermocouple Locations on Test Unit

During ambient testing, the sink and ambient temperatures were monitored with a hand held thermocouple reader. During vacuum testing, thermocouples 6 and 12 were removed from the LHP and applied to the sink plate and inner wall of the vacuum chamber.

3.2.7 Data Acquisition

The potential from the thermocouples and voltage from the power supply were measured and recorded using a National Instruments SXCI -1000 data acquisition system. The precision for this system was estimated at +/- 1%. A LabVIEW Virtual Instrument (VI) was created to support the data acquisition system and log the data. The VI also visualized the data in real-time plot to allow for the verification of start up and proper operation of the LHP during testing. Figure 3.5 provides a schematic of the overall test set-up.

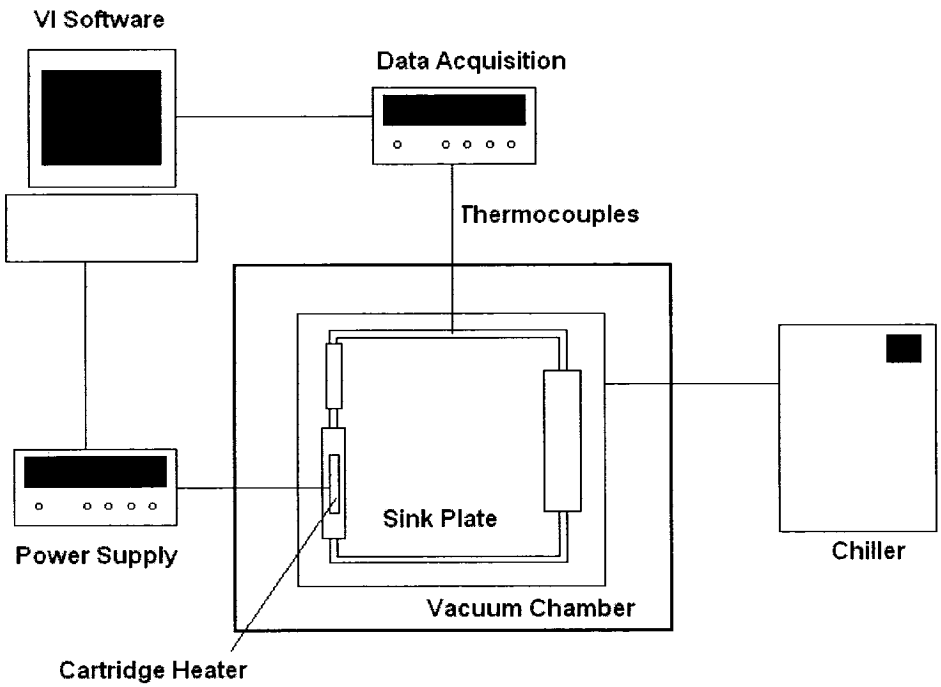

Figure 3.5: Test Set-up

3.3 Ambient Testing

A series of tests was conducted in the ambient environment to investigate the characteristics of the LHP during both steady-state and transient operation. Specifically, start-up, steady operation, power cycling, and temperature hysteresis characteristics were investigated.

3.3.1 Start-up

Testing was performed to verify the start-up capabilities of the LHP. Reliability and time to start-up was compared at both high and low power levels. LHP start-up is characterized by the initialization of circulation within the LHP and is typically visible on a temperature plot by a sudden drop in liquid line temperature as cold liquid is pushed

from the cooled condenser into the ambient temperature liquid line, and a sudden increase in vapour line temperature as warm vapour is pushed in from the evaporator. These features are clearly visible in Figure 3.6, which illustrates a 10 W start-up with a sink temperature of 15 °C.

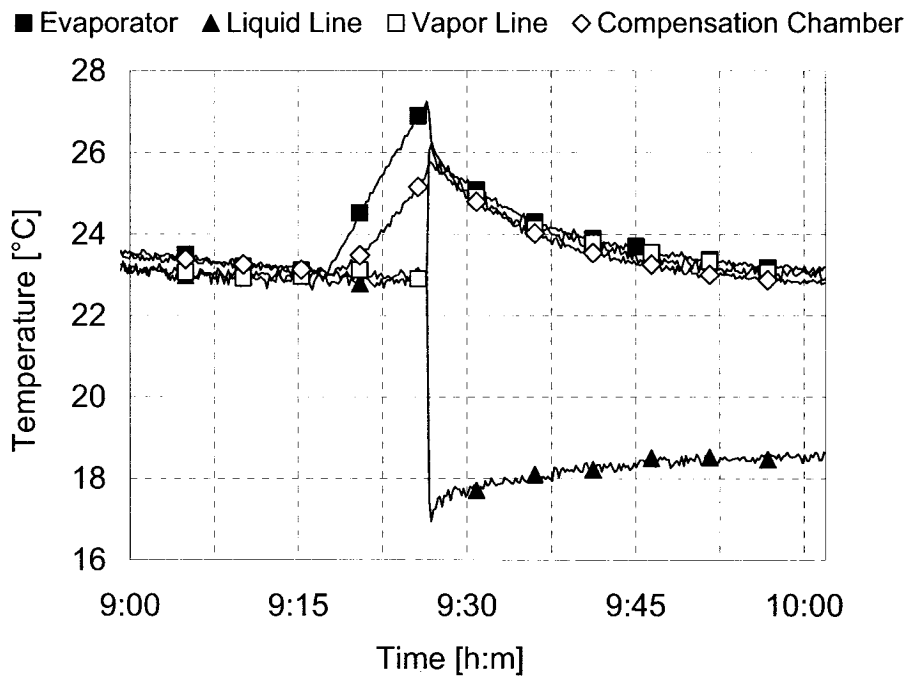

Figure 3.6: 10 W Start-up

Several start-ups were attempted at various heat loads with sink temperature of 15 °C. Under these conditions, the LHP showed reliable start-up capabilities at powers ranging from 2 W to 100 W. Through comparison of start-up data generated under similar conditions, it was noted that the temperature reached by the evaporator prior to start-up varied between tests. Two such examples are presented in Figures 3.7 and 3.8, where the temperature measured by thermocouple 1 is plotted against time since the application of power. In Figure 3.7, both tests were initiated with the application of 100

W to the evaporator, and were conducted with identical sink temperatures (14.5 +/- 0.25 °C), and under identical ambient temperatures (24.9 +/- 0.3 °C). In Figure 3.8, both tests were initiated with the application of 10 W to the evaporator, and were conducted with identical sink temperatures (15.2 +/- 0.4 °C), and under identical ambient temperatures (24.5 +/- 0.2 °C).

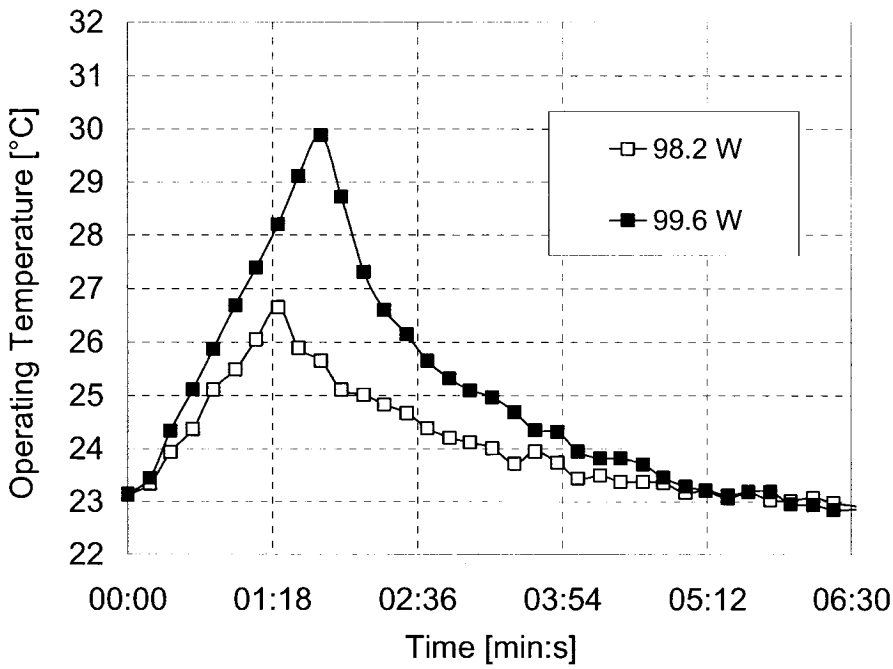

Figure 3.7: Difference in Evaporator Temperature Prior to 100 W Start-up

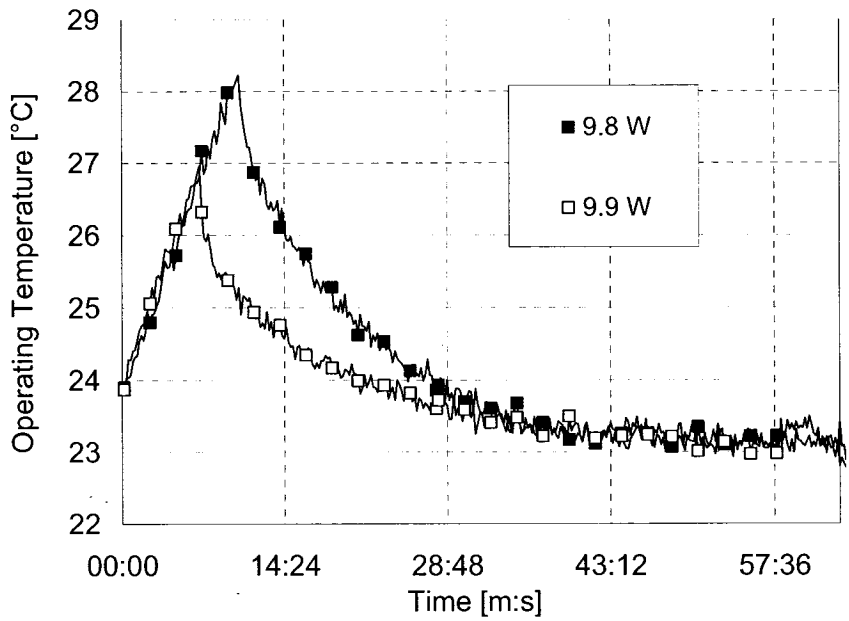

Figure 3.8: Difference in Evaporator Temperature Prior to 10 W Start-up

Here it can be observed that under seemingly identical conditions the operating temperature before start-up varied by as much as 3 °C. It is important to note that although the temperatures before start-up varied, the steady-state temperatures reached after start-up were identical in both cases.

In addition to the power applied to the evaporator, initial conditions within the evaporator greatly influence start-up. If the evaporator grooves are liquid filled prior to start-up, a superheat will be required to initiate nucleate boiling; however, if the grooves already contain vapour prior to start-up, liquid will begin to evaporate as soon as power is applied to the LHP. If the evaporator core is filled with liquid prior to start-up, the heat leak to the evaporator will be minimized. However, if there is vapour present in the evaporator core prior to start-up, the evaporator core becomes an extension of the compensation chamber and the heat is transferred to the reservoir more effectively. These factors influence the time required to initiate start-up as well as the temperature of

the evaporator prior to start-up (Ku, 1999). A summary of start-up tests and results is presented in Table 1, where T_{max} refers to the maximum average evaporator temperature prior to start-up. The results presented in Table 3.1 are consistent with the previous explanation regarding the state to the evaporator core prior to start-up.

Table 3.1: Summary of Start-up Results

Applied Power [W]	Average Sink Temperature [°C]	Average Ambient Temperature [°C]	Time to Start-up [min:s]	T_{max} Before Start-up [°C]
196.6	15.1	25.0	0:33	25.5
197.7	14.6	24.7	0:34	24.6
98.8	15.1	24.5	0:46	25.6
98.2	14.4	24.8	1:33	26.9
99.6	14.5	23.7	1:44	29.9
9.8	14.8	24.5	11:20	28.6
9.9	15.6	24.8	7:06	27.1
4.9	14.6	24.7	19:13	27.5

3.3.2 Power Cycling

Power cycling was performed to generate a performance curve for the LHP in the ambient environment. Tests involving the successive application of various heat loads were performed to obtain performance curves for LHP operation. Power cycling was performed at atmospheric pressure and a sink temperature of 15 °C. The LHP was allowed to reach steady-state before each increase, and the criterion for steady-state was defined as a temperature change no grater that 0.5 °C over a period of 30 minutes. Performance curves generated through successive increases in power were compared to those generated through successive decreases in power. Figures 3.9, 3.10, and 3.11 show the temperature profiles of the LHP during the power cycling tests.

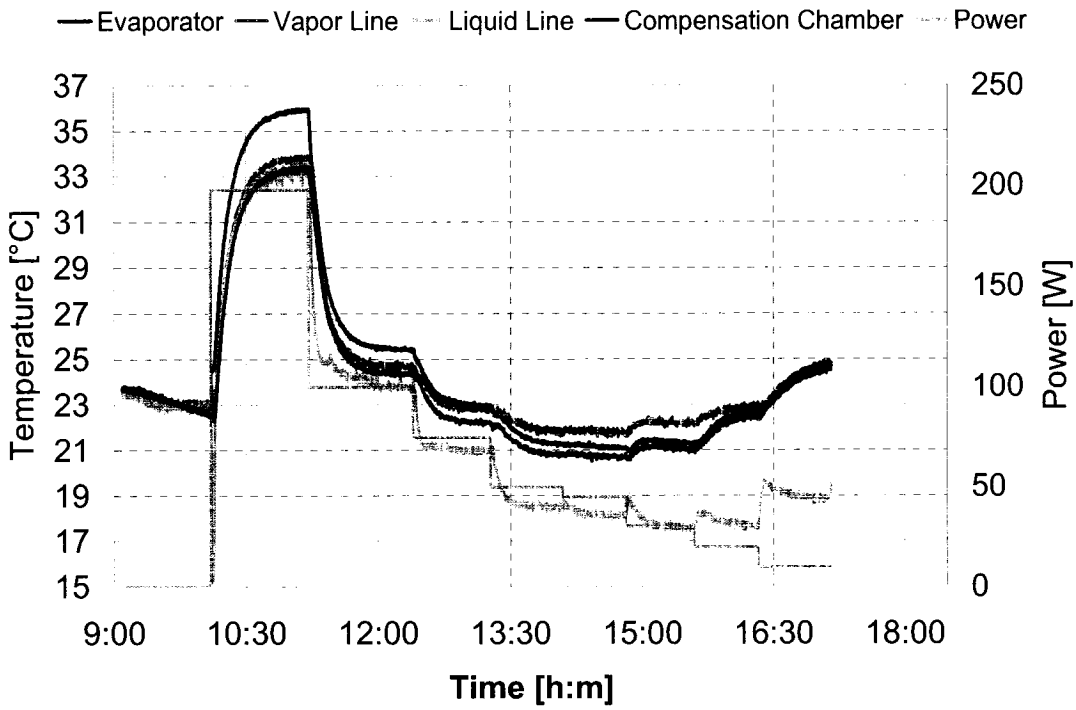

Figure 3.9: Temperature Profile for 197.7 W Start Power Cycle

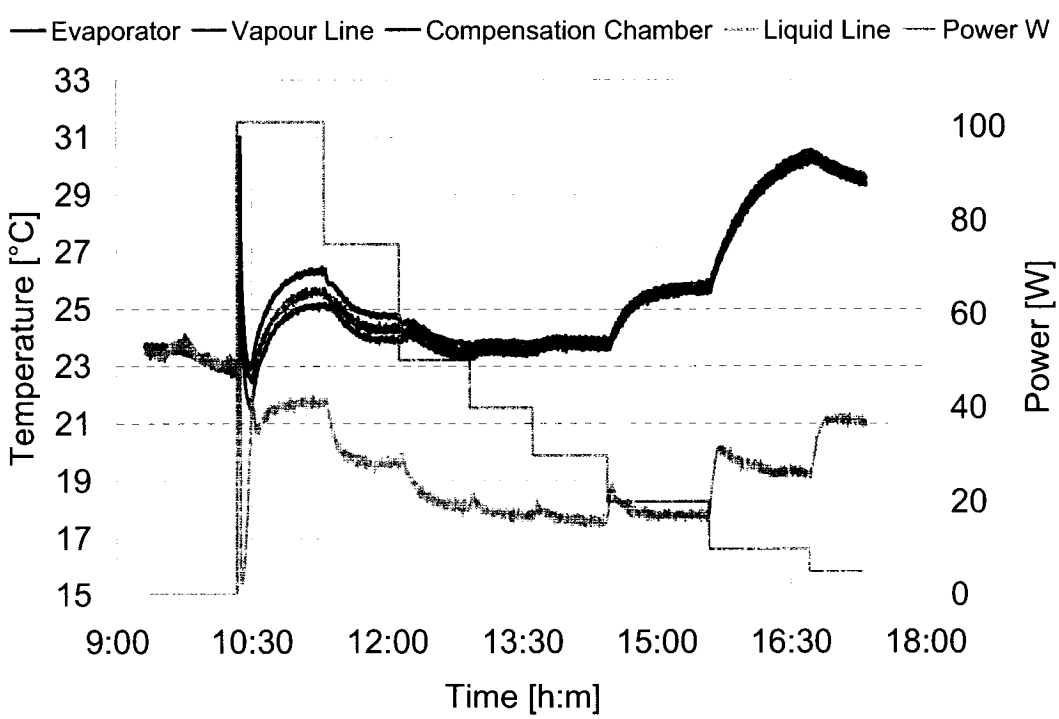

Figure 3.10: Temperature Profile for 101.0 W Start Power Cycle

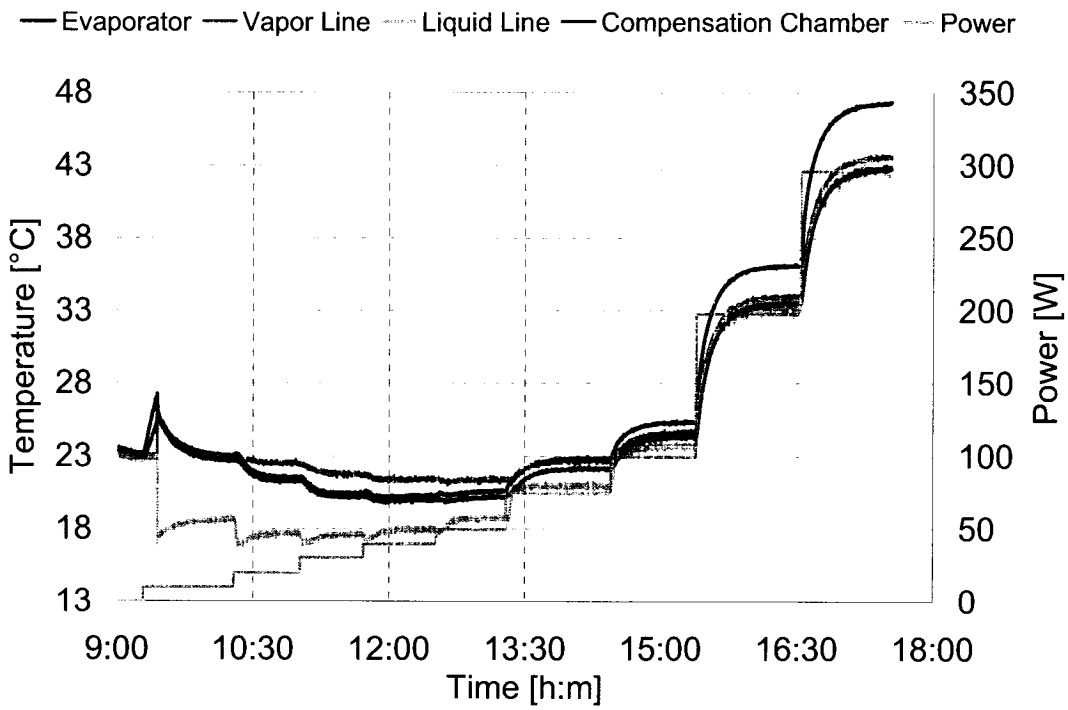

Figure 3.11: Temperature Profile for 9.9 W Start Power Cycle

The steady-state operating temperature is presented as a function of applied power in Figure 3.12.

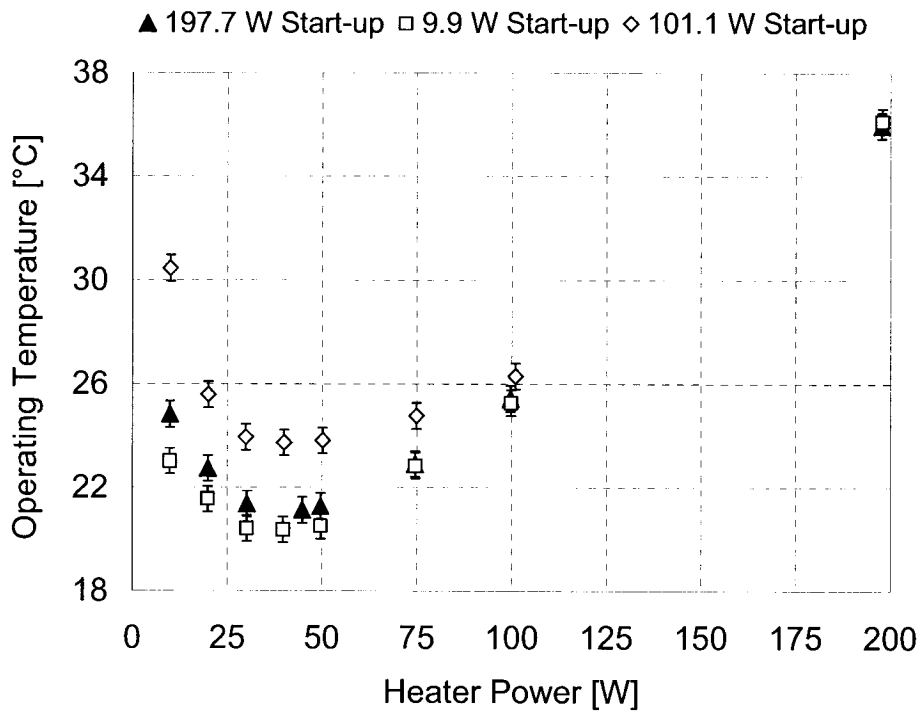

Figure 3.12: Operating Temperature as a Function of Applied Power
Error bars represent +/- 0.5 °C thermocouple precision

All three curves indicate that operating temperature increases with input power at high power loads, while at low power loads operating temperature decreases as input power is increased. This is consistent with the expected behavior of and LHP operating with a sink temperature lower than that of the surroundings. At low power loads the condenser of the LHP is only partially active, and the LHP operates in variable conductance mode in this range. Although liquid leaving the condenser is close to the sink temperature, heat leak from the ambient increases the temperature of the fluid as it travels through the liquid line to the compensation chamber. Under steady-state conditions, the heat leak from the evaporator to the compensation chamber must be balanced by the subcooled liquid returning from the condenser. As the power load increases, the mass flow through the LHP increases and the liquid returning to the compensation chamber is less affected

by heat exchange with ambient; as a result, the operating temperature decreases. This trend continues until the condenser is fully active and the operating temperature reaches a minimum. In this range, the operating temperature of the LHP is primarily dependant on the heat gain of the liquid returning to the compensation chamber, and is said to operate in variable conductance mode. At higher power loads, the condenser can no longer dissipate excess energy and warmer fluid flows back to the compensation chamber. The operation temperature increases allowing the condenser to reject additional heat. Within this range, the operation temperature increases almost linearly with power load and the LHP is said to operate in fixed conductance mode (Ku, 1999). From Figure 3.12 the transition between variable and fixed conductance modes is seen to occur between 40 and 50 W for all tests. A significant variation in operating temperature in the variable conductance region is also noted. This is likely related to the condition of the fluid in the evaporator core. One of the main advantages of the LHP is that the liquid passing through the evaporator core from the condenser helps prevent the accumulation of vapour. However, at very low applied powers, the mass flow of liquid returning from the condenser may be insufficient to prevent vapour formation in the evaporator core, causing an increased heat leak to the compensation chamber and resulting in an elevated operating temperature. The slight variance between the 9.9 and 197.7 W start curves was likely due to the fact that the tests were completed on different days, and had slightly different sink and ambient temperatures. This variance suggests the sensitivity of LHP performance to parasitic heating due to ambient interactions, particularly in the variable conductance region. At high powers, the influence of the parasitic heat exchange on the operating temperature is much less because of the increased mass flow rates and the

operating temperatures are seen to converge in this range despite the differences in sink and ambient temperatures.

3.3.3 Temperature Hysteresis Investigation

Power cycling was used to investigate the possibility of temperature hysteresis during LHP operational cycles. Past testing of LHPs has revealed that the loop operating temperature depends on the recent history of the applied heat, even when all other test conditions (i.e. ambient temperature and sink temperature) remain unchanged. This discrepancy is known as temperature hysteresis. Previous work on the subject may be found in Kaya and Ku (1999). Although temperature hysteresis behaviors in LHP operation are not well understood, they are thought to be strongly related to the void fraction of vapour in the evaporator core. As the heat load applied to the evaporator is decreased the active condensation area within the condenser is reduced as fluid from the compensation chamber is pushed into the condenser through the evaporator core. During small or moderate decreases in power, only liquid is supplied from the compensation chamber. However, during large decreases in power, the pressure required to transport the liquid from the compensation chamber to the condenser may exceed the capillary limit of the secondary wick. This may cause a partial dry-out of the secondary wick where by one or more vapour bubbles may become trapped within the secondary wick. The presence of vapour within the secondary wick increases the thermal coupling between the evaporator and the compensation chamber and therefore, the heat leak and corresponding operating temperature also increase.

The LHP was examined for possible temperature hysteresis by cycling between two power loads. Two such tests were performed: power was cycled between 20 and 100 W during the first test, while power was cycled between 5 and 200 W during the second

test. In both cases the operating temperature was allowed to reach steady-state before the power load was changed. The results of these large step hysteresis tests are summarized in Table 3.2.

Table 3.2: Test Results Obtained Using Large Power Steps

Test 1		Test 2	
Power [W]	**Steady-state Operating Temperature [°C]**	**Power [W]**	**Steady-state Operating Temperature [°C]**
98.2	26.3	196.6	35.8
19.7	26.0	4.9	24.6
98.4	27.1	196.9	36.0
19.7	26.7	4.9	24.4

At all large step test powers, the variation between operating temperatures at each power level was smaller than the precision of the thermocouples. No evidence of temperature hysteresis was observed during these tests.

3.3.4 Stable Operation

The LHP was tested for operational stability at 100 W and 10 W. In these tests the LHP was allowed to operate for six hours under a constant sink temperature of 15 °C and a constant applied power. The LHP demonstrated stable operation at both power levels as the operating temperature of the LHP varied less than +/- 0.5 °C (a variation smaller than the estimated precision of the thermocouples) after reaching steady-state in both cases.

3.3.5 Effective Thermal Resistance

LHP thermal transport capability is sometimes examined in terms of thermal resistance. In this study an effective thermal resistance was defined as:

$$R_{eff} = (T_e - T_c)/Q_e \tag{3.1}$$

where:

R_{eff} is effective thermal resistance

T_e is evaporator temperature

T_c is condenser temperature

Q_e is the net heat load applied to the evaporator

Figures 3.13, 3.14, and 3.15 show the thermal resistance of the LHP during the power cycles discussed in section 3.3.2.

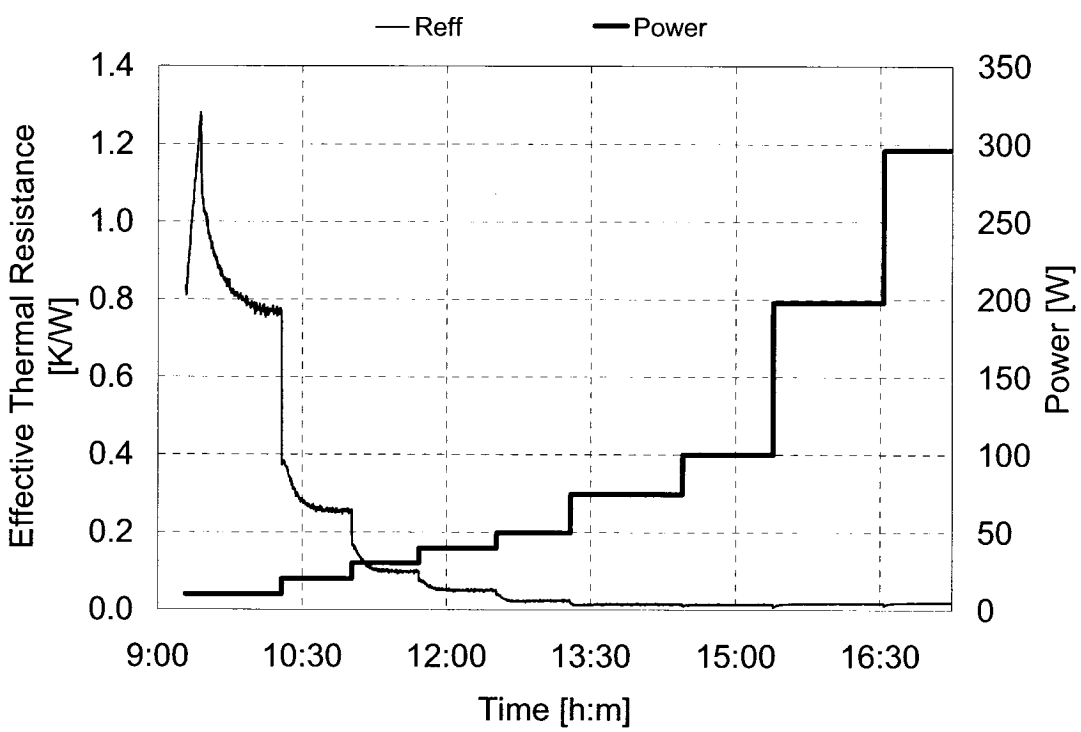

Figure 3.13: Effective Thermal Resistance During 9.9 W Start Power Cycle

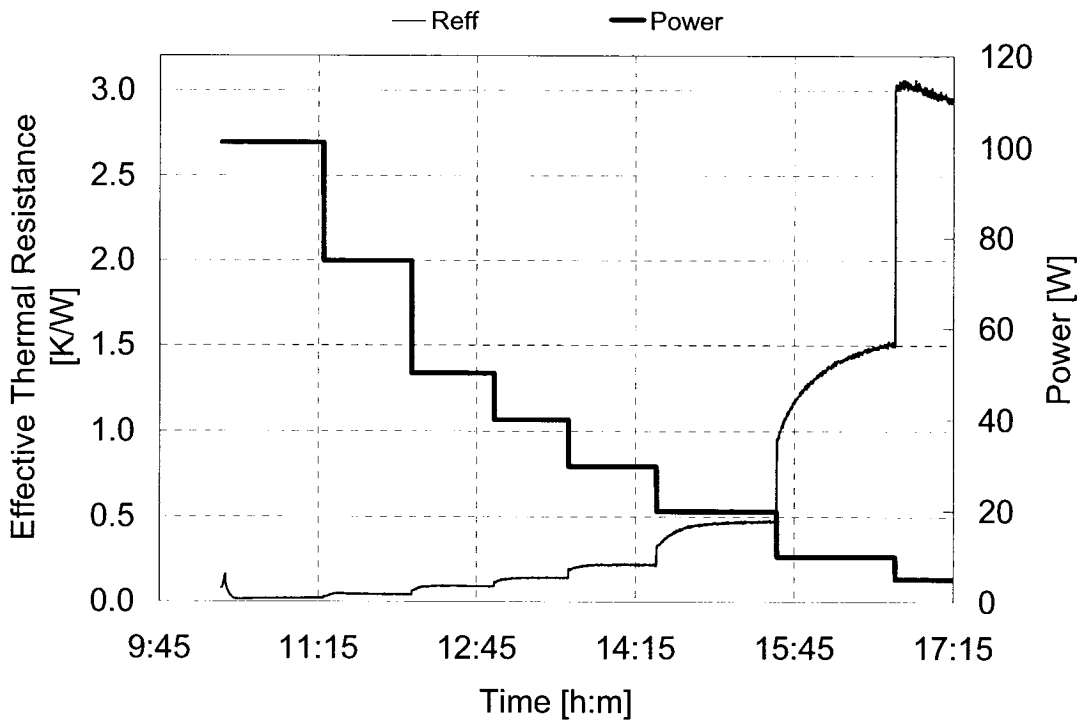

Figure 3.14: Effective Thermal Resistance During 101.0 W Start Power Cycle

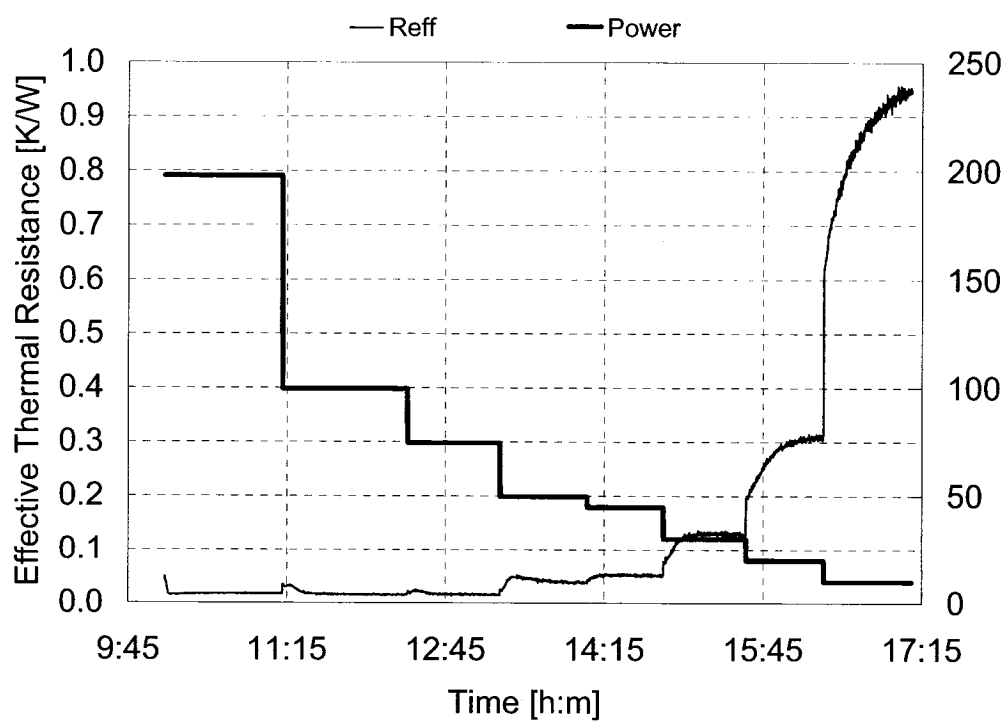

Figure 3.15: Effective Thermal Resistance During 101.0 W Start Power Cycle

From these figures it can be noted that, in general, the effective resistance of the LHP decreases as the heat load applied to the evaporator is increased. An interesting feature of these plots is that the effective resistance remains approximately constant at applied powers higher than 50 W. This corresponds to the transition between variable and fixed transition modes discussed in section 3.3.2. The minimum thermal resistance observed during ambient testing was 0.014 K/W occurring at approximately 100 W. The observed effective thermal resistance increased only slightly to 0.018 K/W as the power load was further increased to 300 W. It is presumed that there the LHP has an optimal operating condition where the thermal resistance is minimized; however, further testing in the high power region is needed to identify this point. The effective thermal resistance of each operating point in all ambient tests is plotted as a function of power in Figure 3.16.

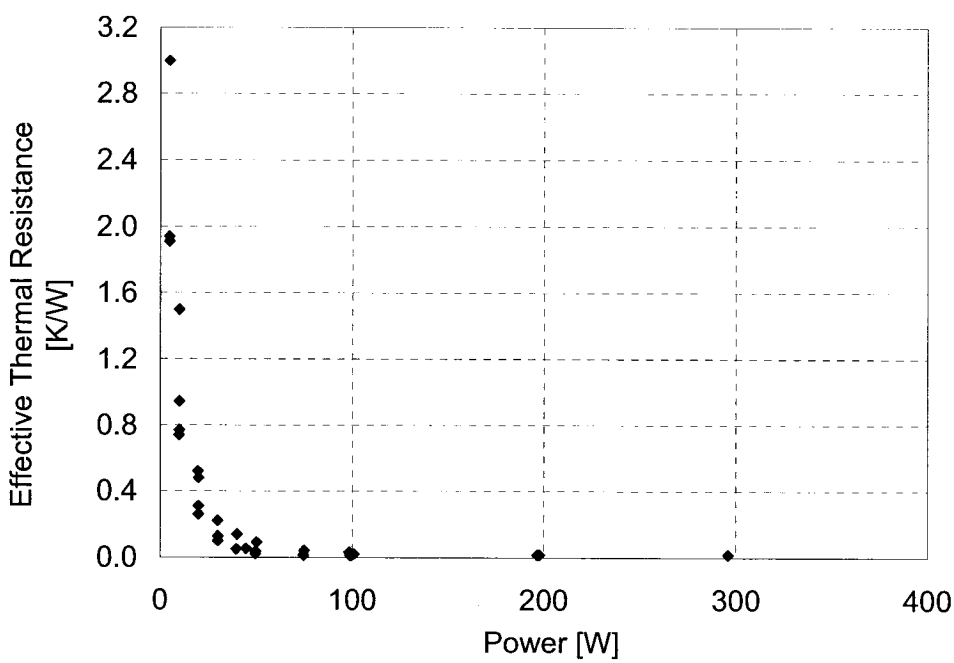

Figure 3.16: Effective Thermal Resistance as a Function of Power (Ambient Testing)

Because of the seemingly exponential relation between effective resistance and applied power, the log of the effective resistance is plotted against the log of the applied power in Figure 3.17.

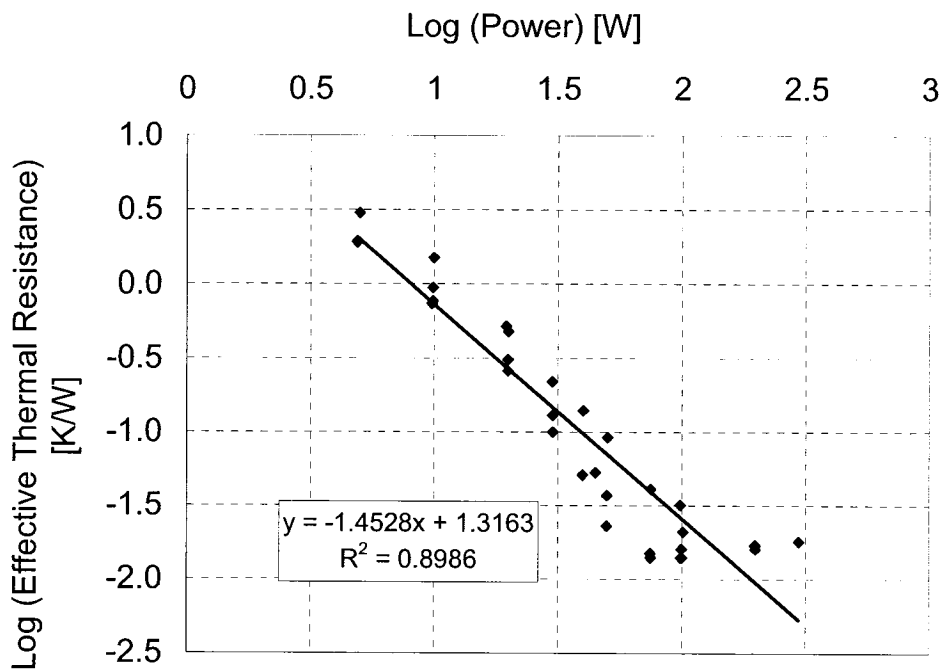

Figure 3.17: Log-Log Plot of Effective Thermal Resistance as a Function of Power (Ambient Testing)

Figure 3.17 shows a clear linear trend between the log of effective resistance and the log of applied power.

3.4 Vacuum Testing

A series of tests was conducted in the vacuum environment to investigate the characteristics of the LHP during both steady-state and transient operation. Specifically, start-up, steady operation, power cycling, and temperature hysteresis were investigated. Where possible, the vacuum data was compared with similar ambient data.

3.4.1 Start-up

Testing was performed to verify the start-up capabilities of the LHP under vacuum conditions. Reliability and time to start-up were compared at both high and low power levels under vacuum conditions. The characteristic start-up features including a sudden drop in liquid line temperature as cold liquid is pushed from the cooled condenser into the liquid line, and a sudden increase in vapour line temperature as warm vapour is pushed in from the evaporator, are clearly visible in the 10 W start-up presented as Figure 3.18.

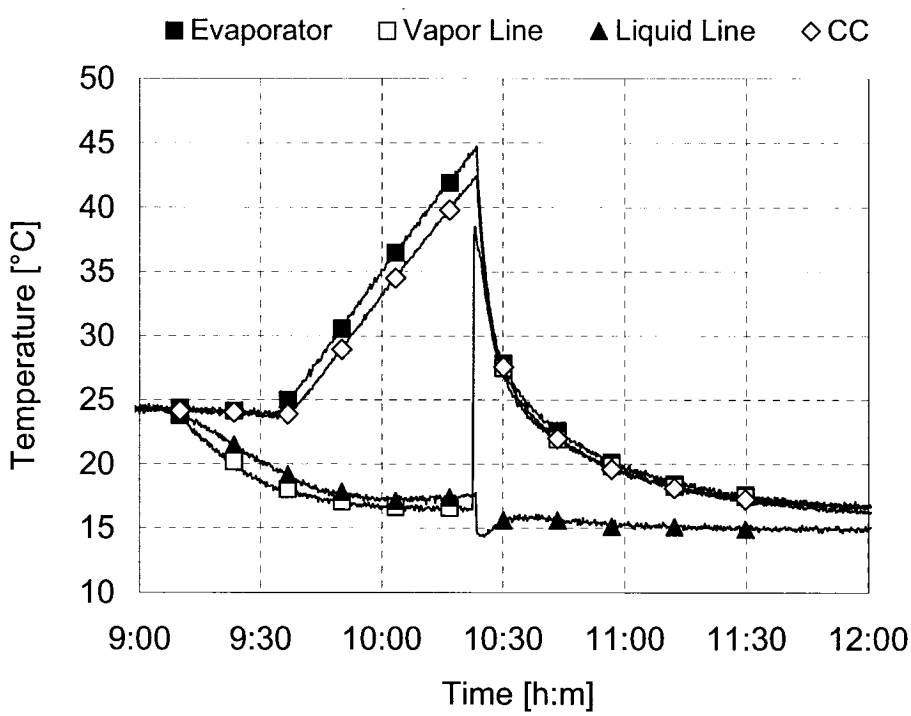

Figure 3.18: 10 W Start-up in Vacuum

In some cases however, the features of start-up are not clearly evident as is the case in figure 3.19.

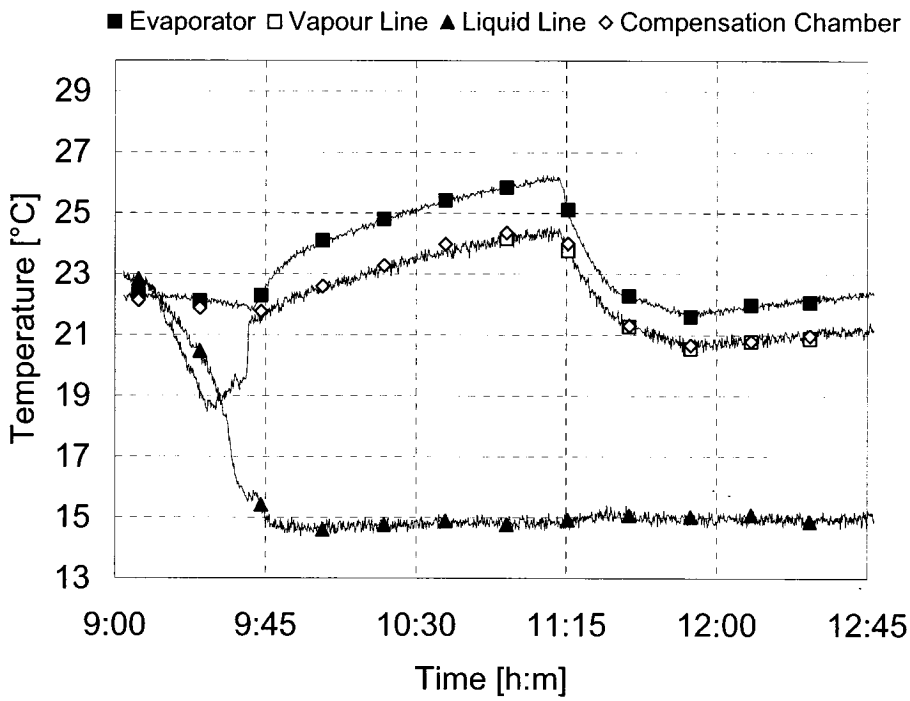

Figure 3.19: 10 W Start-up in Vacuum

In this case, the LHP starts as soon as power is applied to the evaporator. This is consistent with a start-up in which vapour exists in both the vapour grooves and the evaporator core prior to start-up. Under such conditions, evaporation will start immediately with the application of power as no superheat is required to initiate boiling in the grooves. However, the vapour in the evaporator core allows for a much larger heat exchange between the evaporator and the compensation chamber. In this case, the temperature of the evaporator and compensation chamber continues to increase after start-up until cool liquid from the condenser can compensate for the heat leak. The drop in temperature due to the return of cooled liquid returned from the condenser is clearly visible in Figure 3.19.

Table 3.3 summarizes the results of the vacuum start-up testing and provides a comparison of the start-up data generated during ambient testing. It can be noted from Table 3.3 that for the tests with similar conditions (i.e. same sink temperature, heat load, and ambient temperature) the time to start in vacuum was typically longer than the time to start in ambient conditions.

Table 3.3: Comparison of Start-up Times in Vacuum and Ambient Environments

Vacuum Environment				Ambient Environment			
Applied Power [W]	**Average Sink Temperature [°C]**	**Average Ambient Temperature [°C]**	**Time to Start-up [min:s]**	**Applied Power [W]**	**Average Sink Temperature [°C]**	**Average Ambient Temperature [°C]**	**Time to Start-up [min:s]**
193.6	14.8	24.4	2:17	196.6	15.1	25.0	0:33
192.7	14.8	24.4	0:57	197.7	14.6	24.7	0:34
103.1	14.7	24.1	1:44	98.2	14.4	24.8	1:33
95.5	14.7	24.2	2:28	98.8	15.1	24.5	0:46
95.7	14.7	24.1	2:26	99.6	14.5	23.7	1:44
9.6	14.5	24.4	0:16	9.8	14.8	24.5	11:20
9.6	14.4	24.6	52:34	9.8	15.6	24.8	7:06

As previously discussed, it is difficult to predict the time to start-up due to the statistical nature of the start-up mechanism. The start-up times are mostly influenced by the state of the evaporator core and the vapour groves. It was noted that for one test at approximately 10 W in vacuum environment, in one test, the start-up was very quick. In another test with the similar conditions, a significantly longer time was required to initiate start-up. This effect is related to the condition of the working fluid in the evaporator core. In this case the fluid in the evaporator core was most likely two-phase, resulting in a substantially higher heat transfer from the evaporator to the compensation

chamber. Because the LHP starts only when the temperature difference, and therefore pressure difference, between the evaporator and compensation chamber is adequate to initiate the circulation of the working fluid, this increased heat leak significantly increases the time to start-up.

The insulation method applied to the LHP can also play a role in the start-up behavior. In our tests, for the ambient test cases, the evaporator, heater saddle, and compensation chamber were insulated separately; therefore there was no external heat path from the evaporator to the compensation chamber. However, during vacuum testing a single sheet of MLI was used to shield the evaporator-compensation chamber assembly. As a result there was an external path for heat transfer from the evaporator to the compensation chamber. Insulation (MLI) is typically used to shield the evaporator and compensation chamber during vacuum operation to prevent and external radiative heat leak; however, this external heat leak is so small relative to the heat leak associated with a two-phase core condition, that use of MLI will not necessarily ensure a rapid start-up.

3.4.2 Temperature Hysteresis Investigation

A large step power cycle was applied to the LHP to investigate the possible presence of temperature hysteresis behavior in the vacuum environment. Table 3.4 provides a summary of the test. No evidence of temperature hysteresis was observed.

Table 3.4: Test Results Obtained Using Large Power Steps - Vacuum Conditions

Power [W]	Steady-state Operating Temperature [°C]
193.6	39.4
4.8	23.4
193.6	39.4
4.8	24.1

3.4.3 Stable Operation

The LHP was tested for operational stability in the vacuum environment under heat loads of 100 W and 10 W. In these tests the LHP was allowed to operate for six hours under a constant sink temperature of 15 °C and a constant applied power. The LHP demonstrated stable operation as the operating temperature of the LHP varied less than +/- 0.5 °C after reaching steady-state. It was noted however, that the time required to reach steady-state after the initial start was significantly longer in vacuum than in ambient. This is to be expected as the interactions with the surroundings provide increased damping during ambient operation allowing the system to reach equilibrium faster in that environment.

3.4.4 Effects of Convection

In the vacuum environment, the effects of ambient interactions are eliminated and their effects on LHP performance can be further examined by comparing data generated under similar conditions in each environment. Power cycling was performed to generate a performance curve for the LHP in the vacuum environment. A start-up power of 10 W was applied to the LHP vacuum chamber at a sink temperature of 15 °C. The power was successively decreased to obtain a performance curve for LHP operation in the vacuum environment. The LHP was allowed to reach steady-state before each decrease, and the criterion for steady-state was defined as a temperature change no grater that 0.5 °C over a period of 30 minutes. Figures 3.20 and 3.21 present the steady-state operating temperature as a function of applied power, and provide comparisons of data generated from same power start power cycles under similar conditions in the ambient environment.

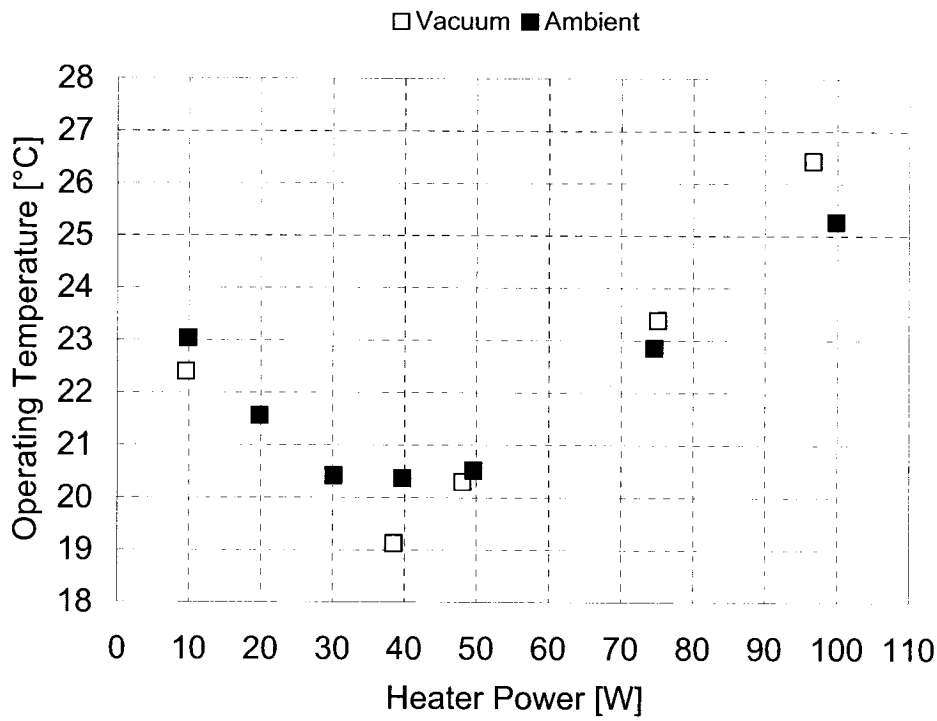

Figure 3.20: Comparison of the Thermal Performance in Ambient and Vacuum Environments – 10 W Start-ups

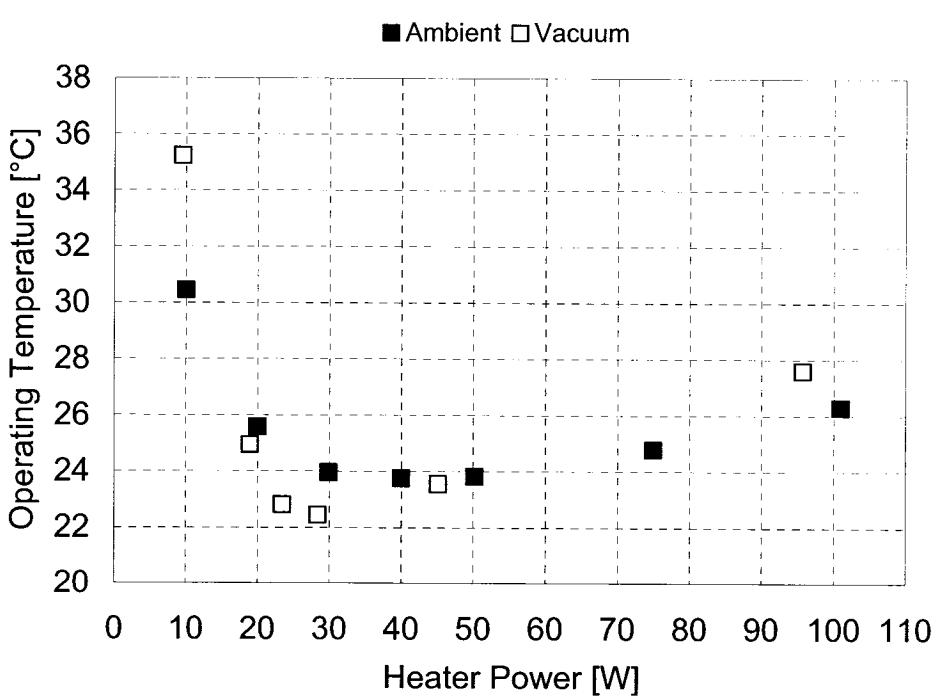

Figure 3.21: Comparison of the Thermal Performance in Ambient and Vacuum Environments – 100 W Start-ups

From Figures 3.20 and 3.21 is observed that the ambient operational temperatures exceed those observed in the vacuum environment lower powers; while at higher powers, vacuum operational temperatures exceed those observed under ambient conditions. Under ambient conditions, free convection cools the compensation chamber when the loop is operating at temperatures higher than the surroundings, thereby increasing the sub-cooling of the liquid returning from the condenser and lowering the operating temperature (Ku, 1999). Similarly, at operating temperatures lower than the surroundings, heat is transferred by convection from the surroundings to the liquid line and compensation chamber, raising the operating temperature. In the vacuum environment, as the LHP was covered by MLI, the heat exchange with the ambient was significantly reduced. As a result, the LHP operating temperatures are offset from those observed in the ambient test case.

3.4.5 Effective Thermal Resistance

Figures 3.22, 3.23, 3.24, and 3.25 show the thermal resistance of the LHP during the power cycles discussed in section 3.4.4.

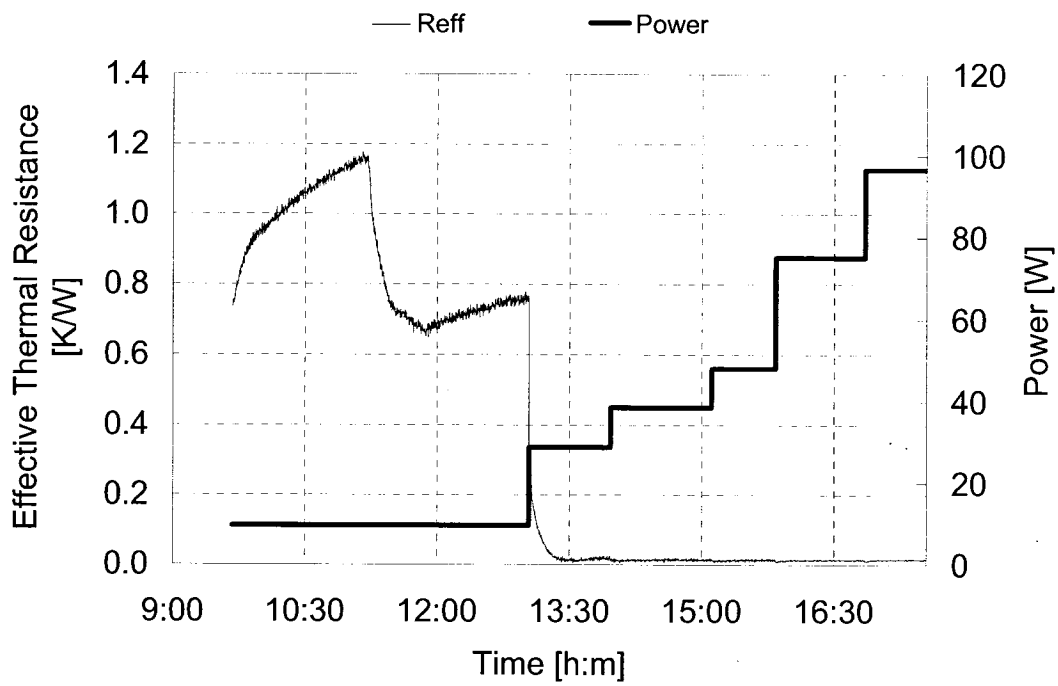

Figure 3.22: Effective Thermal Resistance During 96.6 W Start Power Cycle

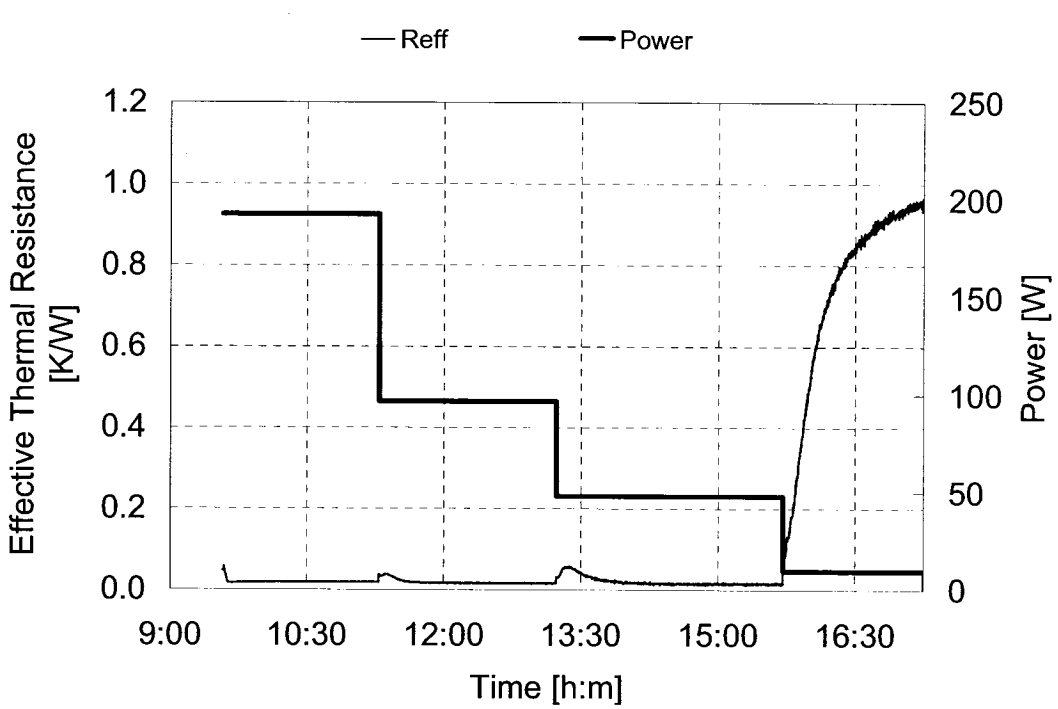

Figure 3.23: Effective Thermal Resistance During 9.7 W Start Power Cycle

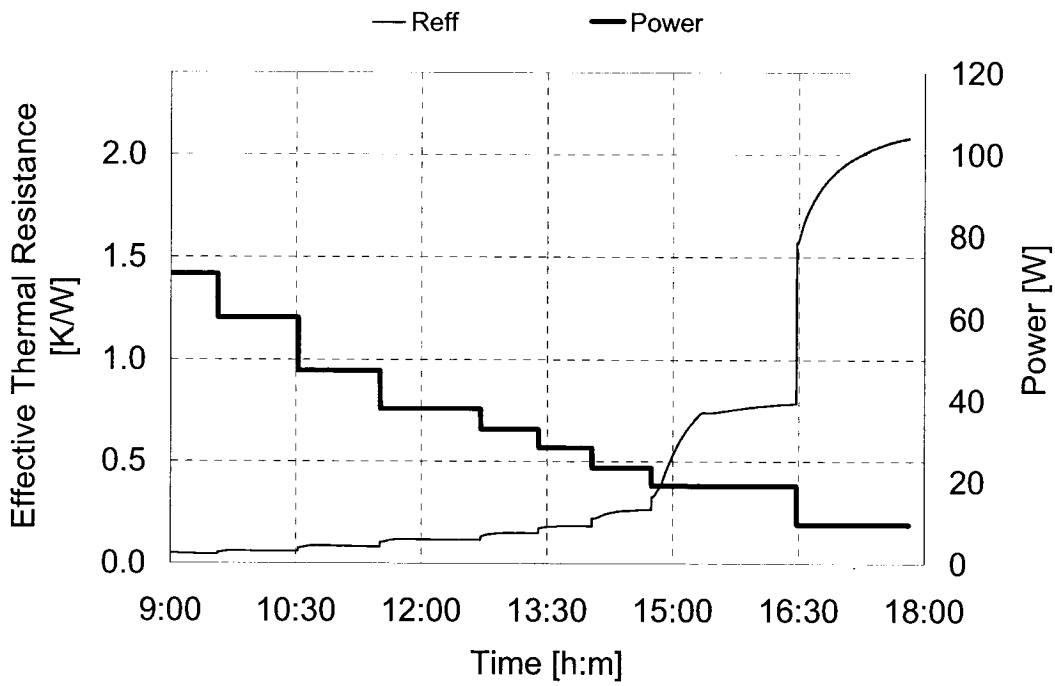

Figure 3.24: Effective Thermal Resistance During 95.5 W Start Power Cycle

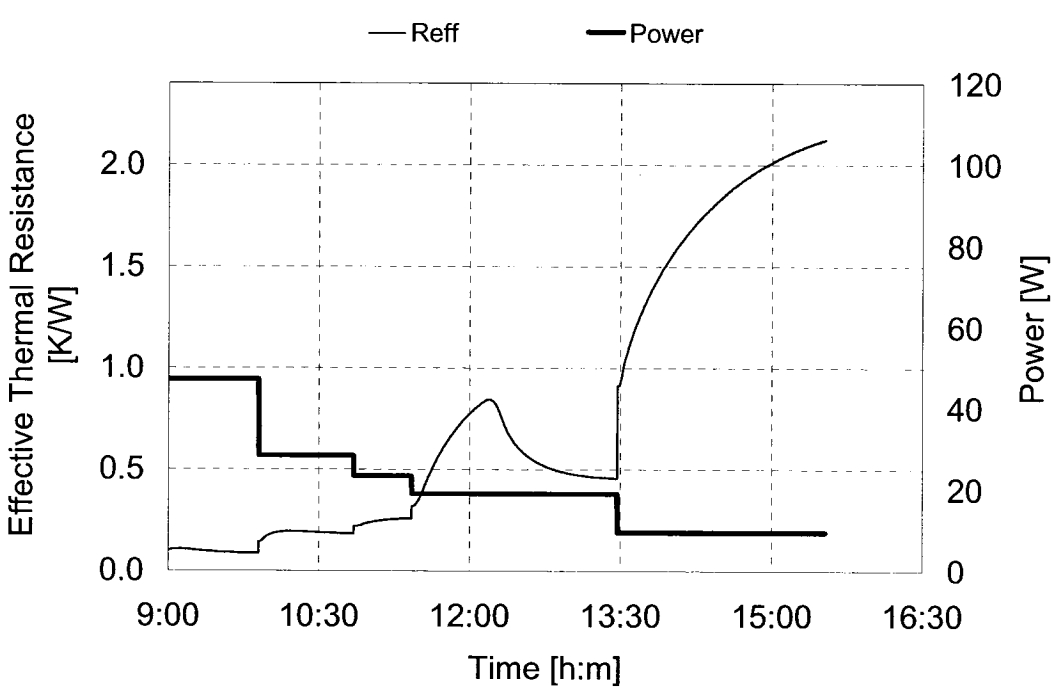

Figure 3.25: Effective Thermal Resistance During 95.7 W Start Power Cycle

From these figures it can be noted that, in general, the effective resistance of the LHP decreases as the heat load applied to the evaporator is increased. As previously discussed with respect to the ambient test results, the effective resistance remains approximately constant at applied powers higher than 50 W. The minimum thermal resistance achieved during vacuum testing was 0.014 K/W, and this is consistent with the value obtained during ambient testing. The effective thermal resistance of each operating point in all ambient tests is plotted as a function of power in Figure 3.26.

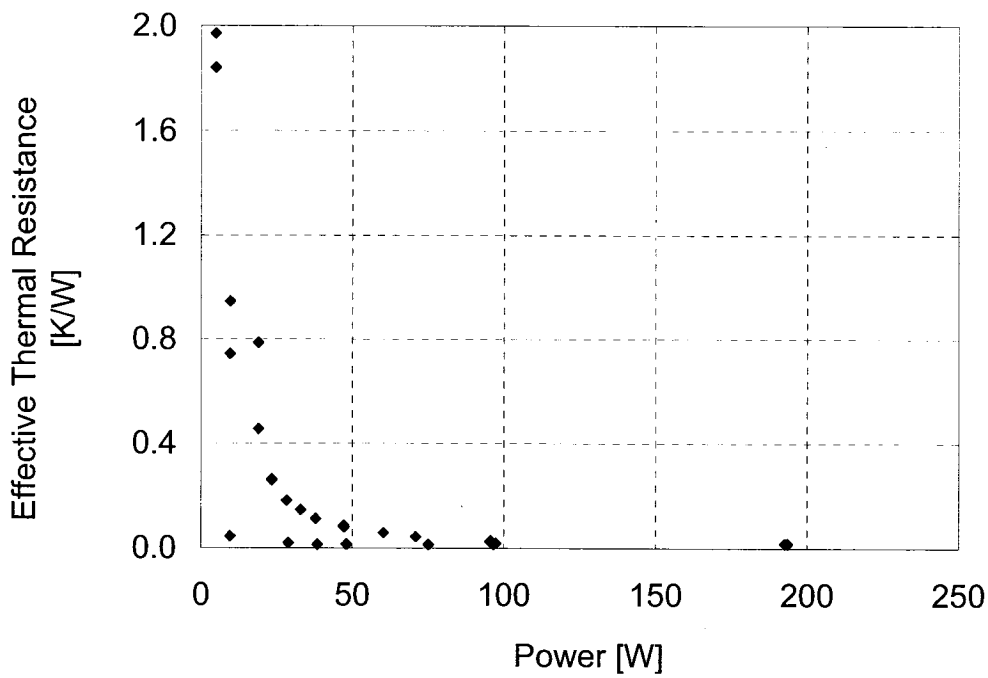

Figure 3.26: Effective Thermal Resistance as a Function of Power (Vacuum Testing)

As was the case during ambient testing, Figure 3.26 shows a seemingly exponential relation between effective resistance and applied power. A log-log plot of the 100 W start-up vacuum data is presented in Figure 3.27.

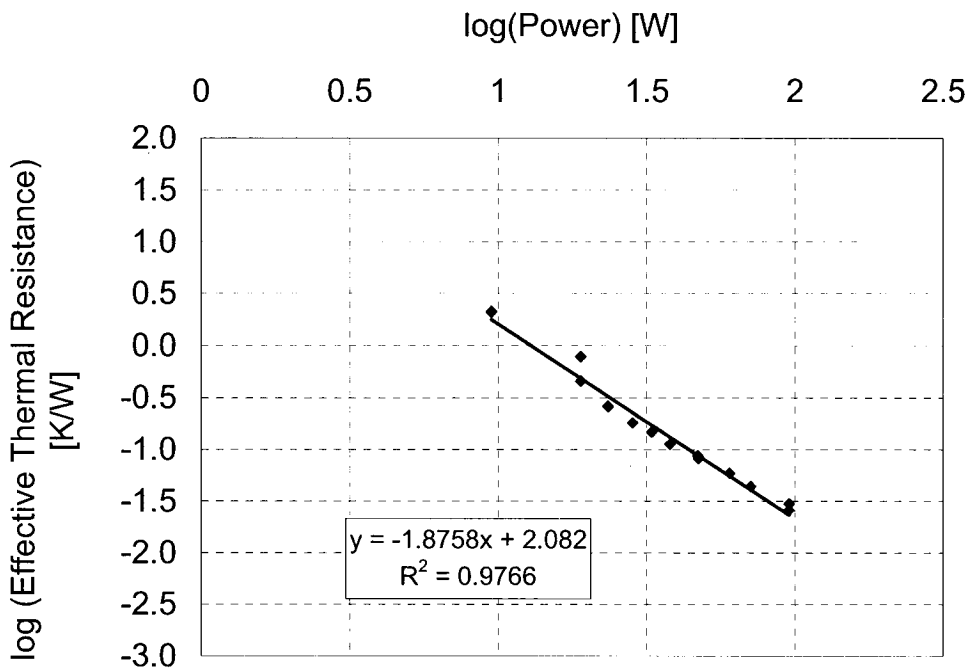

Figure 3.27: Log-Log Plot of Effective Thermal Resistance as a Function of Power (100 W Vacuum Start-ups)

Chapter 4

Computational Modeling

A finite element numerical model for LHP simulation was developed at Carleton University. The task of numerically modeling LHPs presents considerable challenges including the modeling of two-phase flows with heat transfer and phase change in porous media. The phenomena associated with the operation of the LHP, such as the evaporation of the working fluid that provides the driving force for the operation of the loop, are largely concentrated within the evaporator section of the loop. Successful modeling of an LHP is therefore highly dependant on the successful modeling of the evaporator. As such, preliminary development of the computational LHP model described in this work focused on the description of the behaviors and phenomena associated with the evaporator.

The numerical modeling was performed using the MMO Framework, an in-house software platform that uses the finite element method to perform analyses of mechanical and aerospace engineering applications that involve coupled or non-coupled heat transfer,

stress analysis, and fluid dynamics phenomena. The geometry and physical characteristics used in the numerical model were based on the manufacturer's specifications of the TAIS test unit described in Chapter 3. The following section describes the basic finite element theory for heat transfer analysis, and introduces relevant details of the MMO Framework environment. The creation of the LHP model within the framework is also discussed and results of the modeling efforts are presented.

4.1 Finite Element Theory for Thermal Analysis

The finite element method (FEM) is a numerical technique for obtaining approximate solutions to physical problems governed by differential and integral equations; in which a continuum domain is divided into a number of discretized elements. The solution is computed for each local element independently of the global geometry. These solutions are then assembled to produce a solution for the global domain. The FEM process is comprised of seven steps (Lewis and Morgan, 1996):

1. Domain Discretization

The domain is divided into a number of discrete elements, and the geometry of the elements is directly related to the interpolation function. The quantity and distribution of the elements are defined through engineering judgement and elements are generally focused in regions that are likely to contain large gradients. The mesh is usually designed to facilitate the application of boundary conditions and interpretation of results.

2. Interpolation Functions

Interpolation (shape) functions are chosen to approximate the field parameter within the local element. Polynomials are typically used because they are easily

integrated and differentiated. Nodes are assigned to the element and correspond to the number of coefficients to be determined in the interpolation function. Elemental quantities can be expressed as functions of the nodal values and the shape functions. Considering temperature as an example:

$$T(x,y,z,) = \sum_{j=1}^{n} N_j(x,y,z)\overline{T}_j \tag{4.1}$$

where:

T is the temperature at location *(x,y,z)*

n is the number of nodes in the element

N_j are the shape functions

$\overline{T}_j$ are the nodal temperatures

The interpolation functions also represent the basis of the finite element space and are used to map the global *(x,y,z)* space to the solution space *(r,s,t)*, i.e. the location of a point *(x,y,z)* can be described in terms of *(r,s,t)* as:

$$\begin{bmatrix} x(r,s,t) & y(r,s,t) & z(r,s,t) \end{bmatrix} = \begin{bmatrix} R \end{bmatrix} \begin{bmatrix} \overline{x}_1 & \overline{y}_1 & \overline{z}_1 \\ \overline{x}_2 & \overline{y}_2 & \overline{z}_2 \\ \vdots & \vdots & \vdots \\ \overline{x}_m & \overline{y}_m & \overline{z}_m \end{bmatrix} \tag{4.2}$$

where:

[R] is a 1xn matrix of shape functions

$\overline{x}\ \overline{y}\ \overline{z}$ are the coordinates of the nodes

3. Element Properties

Element stiffness matrices are constructed to represent the relationship between field (e.g. temperature) and flow (e.g. heat flux) variables at each node in the element. In heat transfer analysis, the stiffness matrix relates the temperature field to the heat flow, and is a function of material properties, element geometry, and interpolation function.

4. Assembly

The elemental stiffness matrices are assembled into a global stiffness matrix representative of the continuum domain:

$$\{F\} = [K]\{x\} \tag{4.3}$$

where:

$[K]$ is the global stiffness matrix

$\{F\}$ is the thermal load for each node in the domain

$\{x\}$ is the temperature variable for each node in the domain

The assembly process is governed by the physical characteristics of the problem, and generally must comply with either compatibility or continuity depending on the nature of the problem. In heat transfer analysis, continuity of temperature is typically employed.

5. Boundary and Initial Conditions

The global system of equations is modified to include the applied boundary conditions. Boundary conditions are classified as essential Neumann (natural) that represent a constraint on the flux variable or Dirichlet (essential) which represent a constraint on the field variable.

6. Solution

The global system of equations combined with the applied boundary conditions is solved for the field variable vector. Numerical techniques are typically employed in this process allowing for the solution of large practical problems.

7. Post Processing

During post processing the results are interpreted in a relevant and efficient format. This may require the calculation of further parameters.

4.1.1 Galerkin's Method

Galerkin's Finite Element Method, also known as the method of weighted residuals, represents one technique for obtaining approximate (numerical) solutions to partial differential equations. The method of weighted residuals involves essentially two steps. The first step involves the assumption of a general function that approximately satisfies the given differential equation and its applied boundary conditions. The substitution of an assumed approximated function into the equation results in a residual or variation from the real solution. In Galerkin's method this residual is required to vanish in an average sense over the domain of the solution. The second step is to solve the equations given by the first step yielding the approximate solution.

Galerkin's method of weighted residuals can be illustrated by considering the steady state form of the energy equation (SSEE) (Goldak, 2003):

$$\nabla \cdot (-k\nabla T) + \dot{Q} = 0 \tag{4.4}$$

where:

k is the coefficient of thermal conductivity

T is temperature

$\dot{Q}$ is rate of internal heat production

The SSEE is written in approximated form as:

$$\int_{\Omega}(\nabla\cdot(-k\nabla T)+\dot{Q})\phi_i\,d\Omega=\int_{\Omega}(\nabla\cdot(-k\nabla T)\phi_i\,d\Omega+\int_{\Omega}\dot{Q}\phi_i\,d\Omega=0 \tag{4.5}$$

where:

ϕ_i are the coefficients that will be used to minimize the residuals

Green's Divergence Theorem may then be applied to linearize the Laplacian term present in the first integral of equation (4.5). Green's Theorem states:

$$\int_{\Omega}f\nabla^2 g\,d\Omega=-\int_{\Omega}\nabla f\cdot\nabla g\,d\Omega\cdot\int_{\partial\Omega}f(n\cdot\nabla g)d\Gamma \tag{4.6}$$

where n is a unit vector in the outward normal direction. For the SSEE we can make the substitutions:

$$f=\phi_i$$
$$g=-kT$$

and the first integral in (4.5) may be rewritten:

$$\int_{\Omega}(-kT\nabla^2 T)\phi_i\,d\Omega=-\int_{\Omega}\nabla\phi_i\cdot-k\nabla T\,d\Omega+\int_{\partial\Omega}\phi_i(n\cdot(-k\nabla T)d\Gamma \tag{4.7}$$

Fourier's Law of conduction states that:

$$q=-k\nabla T \tag{4.8}$$

Therefore equation (4.5) becomes:

$$\int_{\Omega}\nabla\phi_i\cdot k\nabla T\,d\Omega+\int_{\partial\Omega}\phi_i(n\cdot q)d\Gamma+\int_{\Omega}\dot{Q}\phi_i\,d\Omega=0 \tag{4.9}$$

Given a 3D gradient operator and a generalized n node element ∇T may be written:

$$\nabla T = \begin{bmatrix} \frac{\partial \phi_1}{\partial x} & \frac{\partial \phi_2}{\partial x} & \cdots & \frac{\partial \phi_n}{\partial x} \\ \frac{\partial \phi_1}{\partial y} & \frac{\partial \phi_2}{\partial y} & \cdots & \frac{\partial \phi_n}{\partial y} \\ \frac{\partial \phi_1}{\partial z} & \frac{\partial \phi_2}{\partial z} & \cdots & \frac{\partial \phi_n}{\partial z} \end{bmatrix} \begin{bmatrix} T_1 \\ T_2 \\ \vdots \\ T_n \end{bmatrix} = [B][T] \tag{4.10}$$

where

$$[B] = \nabla \phi$$

Equation (4.5) now takes the form:

$$\int_{\Omega} [\dot{B}]^T k[B][T] d\Omega + \int_{\partial\Omega} \phi_i (n \cdot q) d\Gamma + \int_{\Omega} \dot{Q} \phi_i \, d\Omega = 0 \tag{4.11}$$

Which has the same form as equation (4.3):

$$\{F\} = [K]\{x\} \tag{4.12}$$

where:

$$\{F\} = -\int_{\partial\Omega} \phi_i (n \cdot q) d\Gamma - \int_{\Omega} \dot{Q} \phi_i \, d\Omega$$

$$[K] = \int_{\Omega} [B] k \{B] d\Omega \tag{4.13}$$

$$\{x\} = [T]$$

4.2 MMO Framework

Developed at Carleton University, the MMO Framework uses FEM to perform analyses of mechanical and aerospace engineering applications that involve coupled or non-coupled heat transfer, stress analysis, and fluid dynamics issues. The framework contains full meshing, analysis, and visualization/post-processing modules.

The MMO software is object oriented and written in C++. The software is organized into a series of classes used to define objects that contain both data and data operators. As such, the details of the implementation of the object remain hidden, and the qualities of the finite element method are abstracted. The objects become the building block of the software and contain essential project information including material properties, input geometry, solver parameters, solution timing, as well input and output of data. Some example classes include:

1. Material Class

This class contains the various material properties including enthalpy, specific heat, and thermal conductivity which will be required during the solution process.

2. Meshing Class

Comprises the fundamental information about element and node type, position, ID number, gauss point number etc.

3. Equation Solver Class

Contains the solver to be used in the solution process e.g. Convection Diffusion, Potential Flow, etc.

4. Design File Class

Contains the process planning and supplemental information required for the solver process including, object geometry, boundary conditions, solver parameters etc.

5. Data Dictionary Class

Data structure that controls the input and output of data during the solver process.

Each class defines a number of data operators known as methods that may be available either publicly (available to the user of the class) or privately (available only to the implementer of the class). Table 4.1 lists several publicly available methods frequently employed by the users of the framework. The arguments and return types are given as a non-language specific description of the arguments and return types required and returned by the object (Wang, 2001).

Table 4.1: Sample Public Methods

Method	***Arguments***	***Return and Purpose***
GetPartId	element Id	part Id of the part in the mesh
GetElementPostion	element Id	position of the element
GetNodeIds	element Id	node Id in the element
GetFaceIds	element Id	face Id in the element
GetFacePosition	face Id	position of the face
BoundingBox	minX, minY, minZ maxX, maxY, maxZ	all elements with centres in this range
SetData	data name and values	write data in local dictionary
GetData	data name and values	get data from local dictionary

4.2.1 Design Files

User defined design files contain information to be used by the framework including input mesh information, solution domain, initial and boundary conditions, solution procedure, and visualization strategy etc. The files stipulate the solver to be used in the analyses and also control the flow of data between solvers. In this way, the user of the framework can create a model tailored to simulate the physics of the application.

The design files are organized in a parent-child hierarchy with at least one parent file per project. The parent file contains global information for the project, while the child files contain information to be used by a specific solver or during a specific process. Within the parent file, parts may be declared and assigned part numbers. Each part type can be assigned a material and each part may be assigned initial and boundary conditions. The parent file also defines the path to the child files, and designates each child file as part of the mesh, solver, or visualization modules.

4.2.3 Mesh Module

Within the MMO framework, the mesh module is first used to create the mesh that defines the geometry of the object to be analyzed. Although the framework supports the input of geometry defined by external CAD software, the mesh is typically generated through the use of one or several mesh files that draw on the use of primitives to specify geometric parameters. Frequently employed primitives include hexahedron, prism, cylinder, and sphere, and may be used alone or in combination to define the geometry of the parts.

There are several element types available within the MMO framework but the most frequently used are the 8 and 20 node brick elements. The software also allows for

the creation of contact element whereby adjacent elements retain their own nodes rather than "sharing" coincident nodes with neighboring elements.

4.2.4 Analysis Module

Within the analysis module the partial differential equations describing the physics of the problem are discretized and transformed to a system of algebraic and/or ordinary differential equations to be solved. The analysis module is controlled by a series of user defined design files, with the global parameters contained in the parent file.

Depending on the physics of the problem, one or more solvers may be required to describe its behavior. The solver list in the parent file specifies the solvers to be used in the project and specifies the order in which they are called. Typically, there is one child file per solver that inputs the boundary and initial conditions and specifies the input and output of data to and from the other solvers. A log file created for each solver monitors the convergence of the solution and prints error messages should they arise. Upon convergence, the framework prints the solution to a series of results files.

4.2.5 Visualization Module

Given a complete set of results, the visualization module creates a series of visualization files that can be viewed using the visualization software such as VTK, Ensight, or Gunplot. Typically, the visualization files include both the mesh included in the solution domain and the results of various field variables such as temperature, velocity or pressure. The results can then be further post processed visualizing the results by colour, contour, isosurface, particle trace, vector fields, animations, plots, etc.

4.2.2 Material Library

The MMO material library is a specialized series of user defined files that contain the properties of a set of material types to be called during the solution process. Properties

including density, enthalpy, specific heat, thermal conductivity etc. are assigned to a material name, and the material name may then assigned to a part type in the parent file. The material name associated with each part type can be easily changed, allowing the solver strategy to be easily run using different materials.

Within the material library, the materials may be defined by constant values, tables of values, or by polynomials. For some material properties, such as latent heat, the framework will accept only a constant value. For other more complex properties, more than one value may be assigned in the form of a table. The table lists the material property values to be applied over a range specified by either temperature or specific enthalpy. If a more accurate material property values are required, a continuous or piecewise polynomial may be used; in which case the material property is defined by one or more polynomials over one or more ranges. For example, a material property f may be a function of x, and may be valid over a range from x_1 to x_2:

$$f(x) = a_0 + a_1 x + a_2 x^2 + \cdots + a_n x^n \quad (x_1 \le x \le x_2) \tag{4.14}$$

The independent variable is typically temperature or specific enthalpy and a set of coefficients $a_0 \ldots a_n$ can be specified for several ranges.

4.3 MMO Solvers

This section provides a description of MMO solvers relevant to the LHP and heat pipe problems including Convection Diffusion, Interface, Potential Flow, and Darcy Flow.

4.3.1 Convection Diffusion Solver Equations

The Eulerian form of the Convection-Diffusion equation is defined as:

$$\rho\frac{\partial h}{\partial t}+\upsilon\nabla(\rho h)+\nabla\cdot q+\dot{Q}=0 \tag{4.15}$$

$$q=-k\nabla T \tag{4.16}$$

where:

h is enthalpy

$\rho\frac{\partial h}{\partial t}+v\nabla(\rho h)$ is the rate of change of specific enthalpy of a material point

$\nabla\cdot q$ is the energy diffused into/out of a control volume

k is thermal conductivity

$\dot{Q}$ is the rate at which energy is generated per unit volume of medium

Assuming inviscid flow, and the absence of chemical reactions, there is no heat generated within the medium and $\dot{Q}=0$. The Convection Diffusion equation is then reduced to:

$$\rho\frac{\partial h}{\partial t}+v\nabla(\rho h)+\nabla\cdot q=0 \tag{4.17}$$

4.3.2 Interface Solver Equations

The interface solver was used in the LHP model to simulate the interfaces between the liquid and vapour phases and to model the phase change associated with these interfaces. The mass flux at the liquid vapour interfaces is defined as:

$$\dot{m}=\frac{-k\nabla T}{h_{fg}}=\frac{q_L}{h_{fg}} \tag{4.18}$$

where:

k is thermal conductivity

h_{fg} is latent heat of vaporization

q_L is the heat flux transferred from the liquid

Because the temperature gradient in the vapour is small, we assume that the heat flux transferred from the vapour to the interface is zero. The application of conservation of mass applied across the interface yields the following equation:

$$\dot{m} = \rho_L(\overline{V}_L - \overline{V}_I)\cdot\hat{n} = \rho_G(\overline{V}_G - \overline{V}_I)\cdot\hat{n} \tag{4.19}$$

where:

$\overline{V}_L, \overline{V}_G$ and $\overline{V}_I$ are liquid, vapour, and interface velocities

$\dot{m}$ is mass flux across the interface

$\hat{n}$ is a unit vector perpendicular to the interface

ρ_G and ρ_L are the vapour and liquid densities

Conservation of mass may be rearranged to give the liquid and vapour velocities at the interface:

$$\overline{V}_L = \frac{\dot{m}\cdot\hat{n}}{\rho_L} + \overline{V}_I \tag{4.20}$$

$$\overline{V}_G = \frac{\dot{m}\cdot\hat{n}}{\rho_G} + \overline{V}_I \tag{4.21}$$

These equations are solved by the interface solver.

4.3.3 Darcy Flow Solver Equations

Darcy Flow, a mathematical model for flow in porous media, characterizes flow of the liquid phase of the working fluid through the wick material. Darcy flow states that the flow rate of a liquid through a porous medium is proportional to the hydrostatic pressure gradient across the material:

$$q = \frac{\kappa}{\mu}(\nabla P + \rho g \nabla \eta) \tag{4.22}$$

where:

q is volumetric flow rate per unit area

κ is permeability of the porous material

μ is dynamic viscosity of the liquid

∇P is the pressure gradient across the material

ρ is liquid density

g is acceleration due to gravity

η is the elevation of the interface

The Darcy flow relation may be applied to the incompressible form of the continuity equation:

$$\rho \nabla \cdot \overline{V} = 0 \tag{4.23}$$

to give:

$$\nabla \cdot \left(-\frac{\rho \kappa}{\mu}(\nabla P + \rho g \nabla \eta \right) = 0 \tag{4.24}$$

4.3.4 Potential Flow Solver Equations

The Potential Flow model is used to describe the movement of the working fluid through the LHP. By definition, a flow is irrotational if the vorticity is zero at all points within the flow; that is: the curl of the velocity is zero at all points in the flow field:

$$\nabla \times \overline{V} = 0 \tag{4.25}$$

Defining ϕ as an arbitrary scalar function gives:

$$\nabla \times (\nabla \phi) = 0 \tag{4.26}$$

where the curl of the gradient of a scalar function must be zero. Combining these equations yields:

$$\overline{V} = \nabla \phi \tag{4.27}$$

Therefore, for an irrotational flow, there exists a scalar function ϕ such that the velocity of the flow may be expressed entirely as the gradient of the function. For an incompressible flow, conservation of mass is expressed as follows:

$$\nabla \cdot \overline{V} = 0 \tag{4.28}$$

Therefore for a flow that is both irrotational and incompressible, Laplace's equation applies:

$$\nabla \cdot (\nabla \phi) = \nabla^2 \phi = 0 \tag{4.29}$$

4.4 Numerical Model of LHP

The creation of the LHP model involved three distinct processes. First a mesh was created to represent the LHP geometry. A material library was then created to describe

the material properties of the constituent LHP parts, which were then linked to the LHP mesh. Finally, design files were created to define the solution strategy. These design files regulated the flow of data between the solvers and also contained the initial and boundary conditions to be applied during the solution process. The following sections describe the each process in the creation of the model.

4.4.1 LHP Mesh

A mesh was created to represent the LHP geometry during the analysis process. The geometric parameters input in the mesh corresponded to the test unit described in Section 3.1. Key geometric specifications are summarized in table 4.2.

Due to the need to simplify the model, several assumptions about the geometry of the LHP and the condition of the working fluid at various locations within the unit were made. To reduce the geometric complexity of the mesh, the secondary wick was omitted from the model. Instead, the primary wick was modelled to run the full length of the evaporator and compensation chamber. In addition, the compensation chamber was assumed to contain half liquid and half vapour phases at all times; and phase change of the working fluid in the compensation chamber was not modelled. The evaporator core was also assumed to be entirely liquid filled at all times.

Table 4.2 Geometric Specifications Used in LHP Mesh

Component	*Geometric Parameter*	*Value [m]*
Wick	Outer Diameter	1.4E-2
	Inner Diameter	6.0E-3
	Length	1.9E-1
	Pore Radius	9.0E-7
Vapour Line	Outer Diameter	3.0E-3
	Inner Diameter	2.0E-3
	Length	5.2E-1
Condenser	Inner Diameter	3.0E-3
	Outer Diameter	2.0E-3
	Length	2.5E-1
Condenser Saddle	Outer Diameter	3.0E-2
Liquid Line	Inner Diameter	3.0E-3
	Outer Diameter	2.0E-3
	Length	8.4E-2
Evaporator	Outer Diameter	1.8E-3
	Inner Diameter	1.4E-3
	Length	2.0E-1
Evaporator Saddle	Outer Diameter	2E-2
Compensation Chamber	Outer Diameter	2.4E-2
	Inner Diameter	1.4E-2
	Length	1.0E-1
End Caps	Thickness	3.0E-3

The components within the LHP mesh were designated part numbers and assigned part types. Seven part types were used in the project:

1. Saddle

The blocks surrounding the evaporator and condenser casings were designated as "Saddle", and were used in the model to apply boundary conditions on the outer surfaces of the evaporator and condenser casings. The material "Al_380" was assigned to the saddle parts.

2. Wall

Several components of the LHP structure were designated as "Wall". These included the fluid transport lines, the bayonet, the casing of the evaporator, and the outer wall of the compensation chamber. The material "Al_380" was assigned to the wall parts.

3. Wick

The cylinders constituting the formation of the wick were assigned the part type "Wick". Because the wick is a porous material flooded with liquid working fluid, the "Wick" part type was assigned the composite material properties of liquid water and copper. A discussion of how these properties were determined is provided in Section 4.4.2.

4. Vapour

Water was chosen as the working fluid and the part type of regions containing water in vapour form were designated as "Vapour". Theses included the vapour grooves, vapour line, and the first portion of the condenser.

5. Liquid

The part type of regions containing liquid water was designated as "Liquid". These regions included the liquid line, bayonet, and evaporator core, as well as part of the condenser. The total volume within the compensation chamber was also designated as "Liquid"

6. Interface

The part type of the single element layers separating the vapour in the evaporator grooves from the wick was designated as "Interface". The interface parts were assigned the material properties of liquid water.

7. Ambient

This part type was applied to an artificial enclosure that surrounded the vapour line of the LHP allowing for the application of convective boundary conditions to the outside of the line. The ambient part type was assigned the "air" material.

Twelve mesh design files were needed to create the LHP mesh. "MeshEctrCyl" was used to create the cylinder primitives that formed the geometry of the mesh. Within the framework cylinder primitives are composed of four discrete regions, an inner square, inner cylinder, outer cylinder, and outer square. The cylinder is also separated into four quadrants. This geometry is illustrated in Figure 4.1.

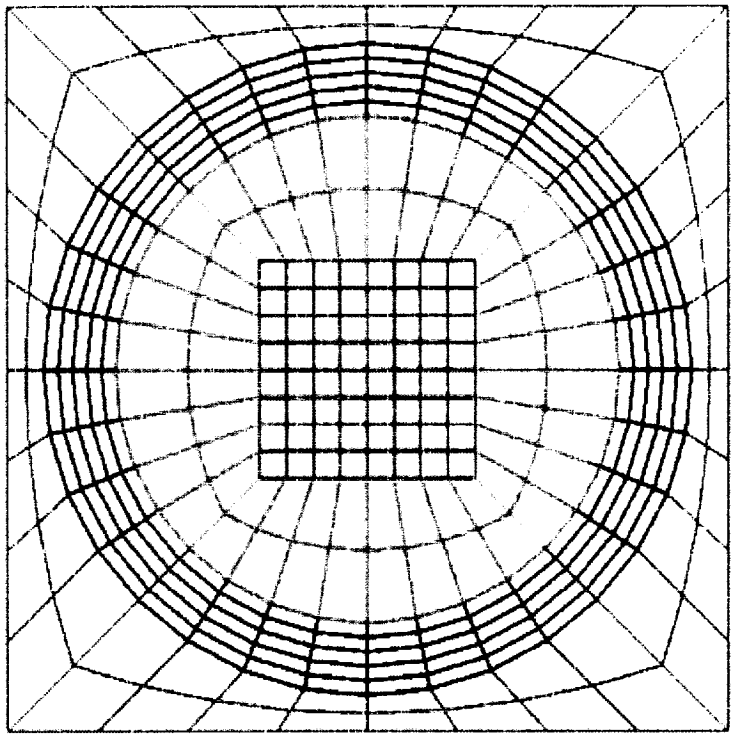

Figure 4.1: Geometry of MMO Cylinder Primitive

The cylinder primitives illustrated in Figure 4.1 are created in the MMO Framework as follows:

```
.START_CYLINDER
CYL1 cyl  4 0.003 401    2 0.007 402    4 0.009 403    2 0.010 404
1 1 1 1
2  0 0 0
2
0 0 0
0.1 0.1 0.1
.END_CYLINDER
```

Where Line 1 designates the start of data input to be used in a single cylinder. Line 2 gives the name of the cylinder, and contains four sets of three numbers. Each set corresponds to one layer of the cylinder: inner square, inner cylinder, outer cylinder, and outer square. The first number in each group represents the number of elements in the radial direction, the second number denotes the "radius" of the layer, and the last number assigns a part number to the region. Each part number corresponds to a part type and specified material properties. Line 3 contains a list of four flags, each of which corresponds to one quadrant of the cylinder. Setting the flag to "1" creates a mesh in the quadrant, while setting the flag to "0" leaves the quadrant empty. The first number on Line 4 designates the number of points to be used in the extrusion of the cylinder; for example, if two points are designated than the cylinder will be created in a single extrusion. The following three numbers give a point on the axis of the cylinder. Line 5 gives the number of elements to be created in the extruded direction, and there must be a value specified for each extrusion. The following lines designate the coordinates of the start and end points of each extrusion, and the number of coordinates specified must correspond with the value indicated on Line 4. The last line designates the end of data input to be used in a single cylinder. The LHP mesh was composed of 62 cylinder primitives. The corners in the fluid transport lines were created using single cylinders extruded in six increments. To accomplish this within the MMO framework the following syntax is used:

```
.START_CYLINDER
CYL2 cyl  4 0.003 401    2 0.007 402    4 0.009 403    2 0.010 404
1 1 1 1
7  0.383 0.014 0.045
1 1 1 1 1 1
0.031 0.014 0.05
0.03 0.014 0.05
0.0291 0.014 0.0496
0.0275 0.014 0.0485
0.0264 0.014 0.0469
0.026 0.014 0.046
0.026 0.014 0.045
.END_CYLINDER
```

Where lines 6 through 12 represent the coordinate end points for the six extrusions.

After the cylindrical components of the LHP mesh were created, a second mesh design file "MeshRemDupNod" was used to apply the "removeDuplicateNodes" method to the mesh to remove duplicate nodes created by layering adjacent and coaxial cylinders.

Four mesh design files were used then employed to create the axial vapour grooves situated in the casing of the evaporator. These features were created by specifying a number of elements and subsequently changing the part type associated with those elements. The "boundingBox" method accepts maximum and minimum X, Y, and Z values and creates a box containing all elements whose centres are situated within these ranges. The "changePartNumbersInBoundingBoxFlag" then allows the part numbers within the bounding box to be respecified. In the case of the vapour grooves, the part type "wall" was re-designated as "vapour" allowing for a groove of vapour to exist within the evaporator wall. The syntax used in the "MeshGroove" design files is as follows:

```
@MeshSection
meshBuilderType$ "Read"
cdfFileName$ "cyl.cdf"
meshType$ "U"
changePartNumbersInBoundingBoxFlag% 1
boundingBox! 0.025 0.0213 -0.195 0.027 0.0225 -0.005
changePartNumbers% 901 201 911 211
outCDFFileName$ "cyl.cdf"
visualizeFlag% 1
visualizerType$ "vtk"
visualizerName$ "cyl-vtk"
@ENDOFSECTION
```

The shape of the grooves is therefore directly related to the geometry of the evaporator mesh created by "MeshExtrCyl". The size of the bounding box, and therefore the size of the grooves, was chosen such that the total volume of the four grooves approximated the value given in the test unit specifications. The total volume of the vapour grooves was approximately 1.8 cc. This was slightly larger than the manufacturer's specification of 1.5 cc; however, because the circumferential vapour grooves were omitted from the mesh, this was deemed an acceptable approximation. One shortcoming of the use of the bounding box technique for the modeling of the vapour grooves is that the density of elements within the mesh cannot be easily altered, because the size and shape of the groove is dependant on the size and location of the original mesh elements.

Four more mesh design files were used to create the interface elements located at contact between the vapour grooves and the wick. The "boundingBox" technique was again used in this case to change "Vapour" elements to elements with part type "Interface".

The design file "MeshCont" was subsequently used to create contact elements at various locations within the mesh. The final mesh file "MeshTotal" was used to specify the partial set to be included in the final mesh output file. This allowed meshes of

the various LHP components to be created easily by altering only one design file. "MeshTotal" created visualization files used for mesh and geometry verification prior to analysis, and also wrote the final mesh output "cdf" files used during the solution process. Within this file, the "removeDuplicateNodes" flag was applied to remove the duplicate nodes that resulted from the use of multiple coaxial and collinear cylinders to define the mesh.

All elements contained in the LHP mesh were either 8 node bricks or contact elements. A generic 8 node brick element is illustrated in Figure 4.2, where the number of each node is given along with the coordinates of the node in the *(r, s, t)* reference frame. Each face of the 8 node brick is a four node quadrilateral element such as the one illustrated in Figure 4.3.

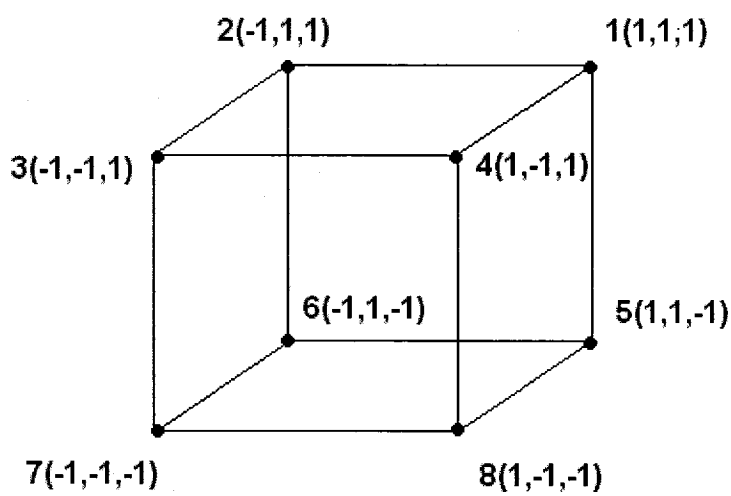

Figure 4.2: 8 Node Brick Element

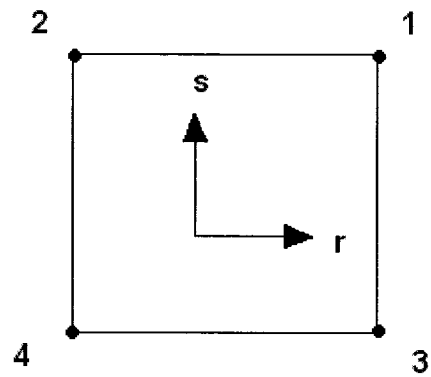

Figure 4.3: 4 Node Quadrilateral Element

The basis (shape) functions for each node must equal 1 at the corresponding node and equal 0 at all other nodes. For the 8 node brick, the basis functions are given by:

$$
\begin{aligned}
N_1(r,s,t) &= \frac{1}{8}(1+r)(1+s)(1+t) \\
N_2(r,s,t) &= \frac{1}{8}(1-r)(1+s)(1+t) \\
N_3(r,s,t) &= \frac{1}{8}(1-r)(1-s)(1+t) \\
N_4(r,s,t) &= \frac{1}{8}(1+r)(1-s)(1+t) \\
N_5(r,s,t) &= \frac{1}{8}(1+r)(1+s)(1-t) \\
N_6(r,s,t) &= \frac{1}{8}(1-r)(1+s)(1-t) \\
N_7(r,s,t) &= \frac{1}{8}(1-r)(1-s)(1-t) \\
N_8(r,s,t) &= \frac{1}{8}(1+r)(1-s)(1-t)
\end{aligned}
\tag{4.30}
$$

Figure 4.4 illustrates the exterior features of the LHP mesh.

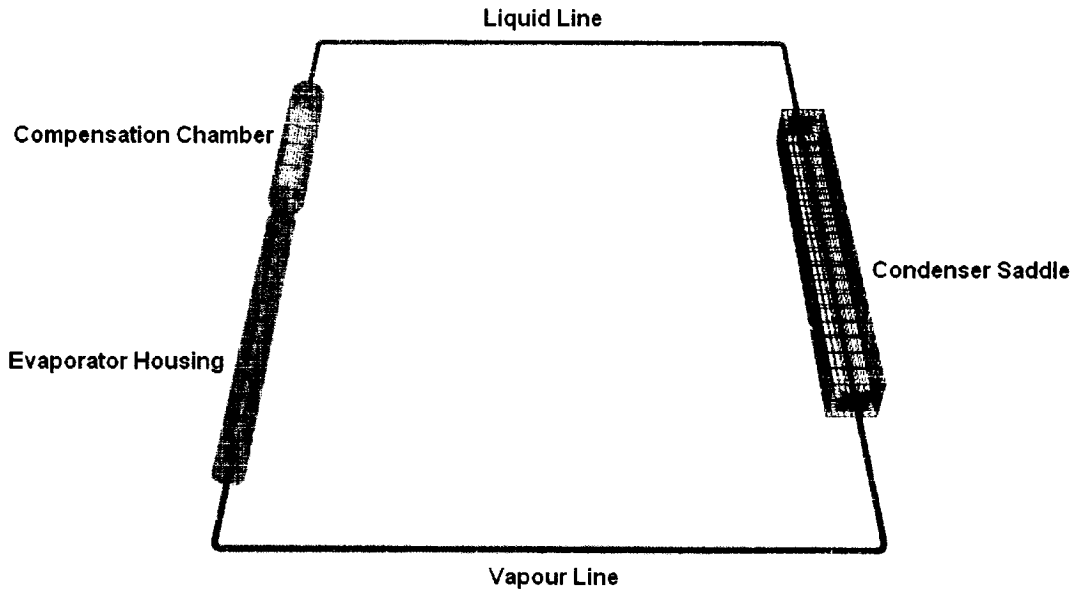

Figure 4.4: Exterior View of LHP Mesh

The internal structure of the evaporator can be viewed in Figure 4.5 which illustrates a cross section of the evaporator. Visible features include the saddle, evaporator casing, wick, vapour grooves, core liquid, and bayonet.

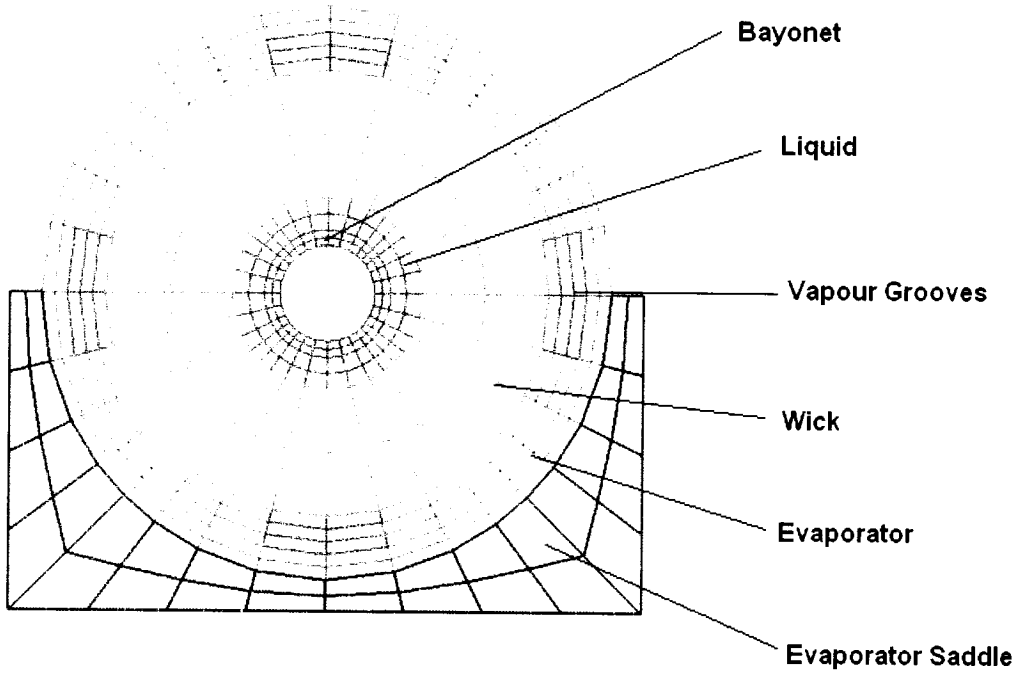

Figure 4.5: Cross Section of Evaporator Mesh

4.4.2 Material Library

The MMO material library is a specialized series of user defined files that contain the properties of a set of material types to be called during the solution process. Properties including density, enthalpy, latent heat, specific heat, melting temperature, thermal density, thermal conductivity, and viscosity are assigned to a material name, and the material name may then assigned to a part type in the parent file. Because the equations in the Convection Diffusion solver are enthalpy based, the enthalpy values for each material must be defined as a linear function of temperature. Initial and boundary conditions are input by the user as temperature values which are then converted to enthalpy values by the solver using the enthalpy relation specified in the material library. If the material undergoes phase change within the specified range, the enthalpy relation will comprise two line segments separated by a jump in enthalpy. This discontinuity

occurs at the melting temperature of the material and the value of the jump corresponds to the latent heat associated with the change of phase. The highest enthalpy value on the lower line in defined as "EnthalpySolid" while the lowest value on the upper line is defined as "EnthalpyLiquid", although physically these values may be associated with other phases.

Because the wick was composed of sintered metal flooded with liquid, "composite" material properties were defined for the wick. For the propose of preliminary modeling, the wick was assumed to be composed of copper and liquid water, and material properties were calculated as a weighted average of solid and liquid properties based on the porosity (void fraction) of the wick as follows:

$$x_{composite} = x_{liquid}\phi + (1-\phi)_{solid} \tag{4.31}$$

where:

x is a given material property

ϕ is the porosity of the wick material

Porosity of the wick was assumed to be 0.594. Table 4.3 summarizes the material properties used in the LHP model.

Table 4.3: Material Properties Used in LHP Model

Material Properties	*Al_380*	*Air*	*WaterLiquid*	*WaterVapor*	*Composite*
Density [kg]	2760.0	1.2	1000.0	0.3	4090.0
Enthalpy [J/m^3]	Figure 4.6	Figure 4.7	Figure 4.8	Figure 4.9	Figure 4.10
Enthalpy Solid [J/m^3]	2.377E9	Not Applicable	1.2296E9	6.0E5	2.0E10
Enthalpy Liquid [J/m^3]	3.297E9	Not Applicable	3.629E9	7.0E5	2.1E10
Latent Heat [J/m^3]	9.20E8	Not Applicable	2.4E9	1.0E5	1.0E9
Specific Heat [J/kgK]	1013.0	1005.0	4200.0	2000.0	2700.0
Melting Temperature [K]	850.0	Not Applicable	373.0	1000.0	850.0
Thermal Conductivity [W/m]	109.0	0.04	0.6	0.024	160.79
Thermal Density [kg/m^3]	2760.0	1.2	1000.0	0.3	4090.0
Kinematic Viscosity [N/m^{2}s]	0.00178	0.00003	0.0006	0.0006	0.0006

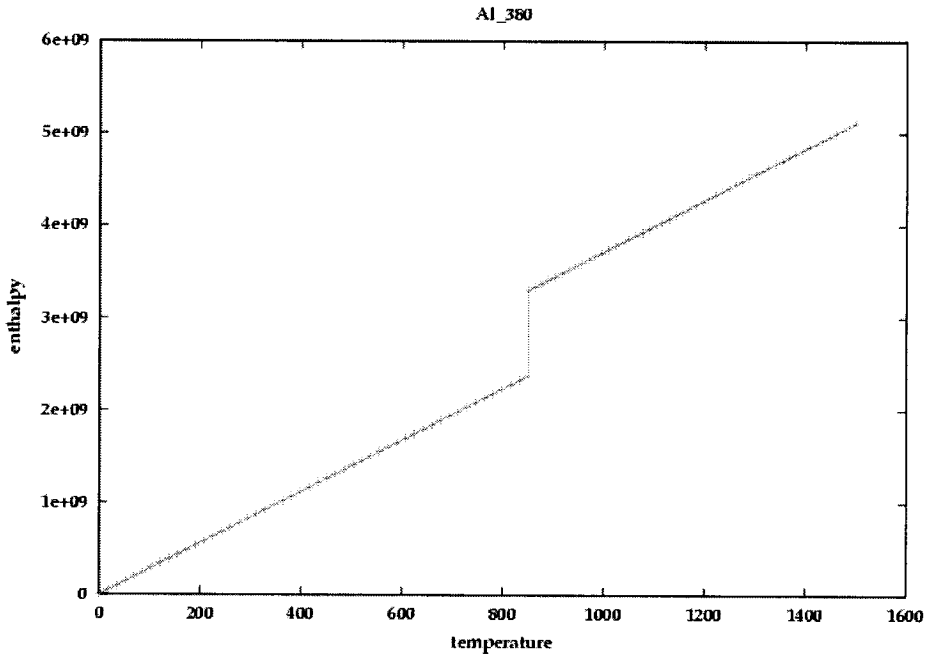

Figure 4.6: Enthalpy Relation for "Al_380"

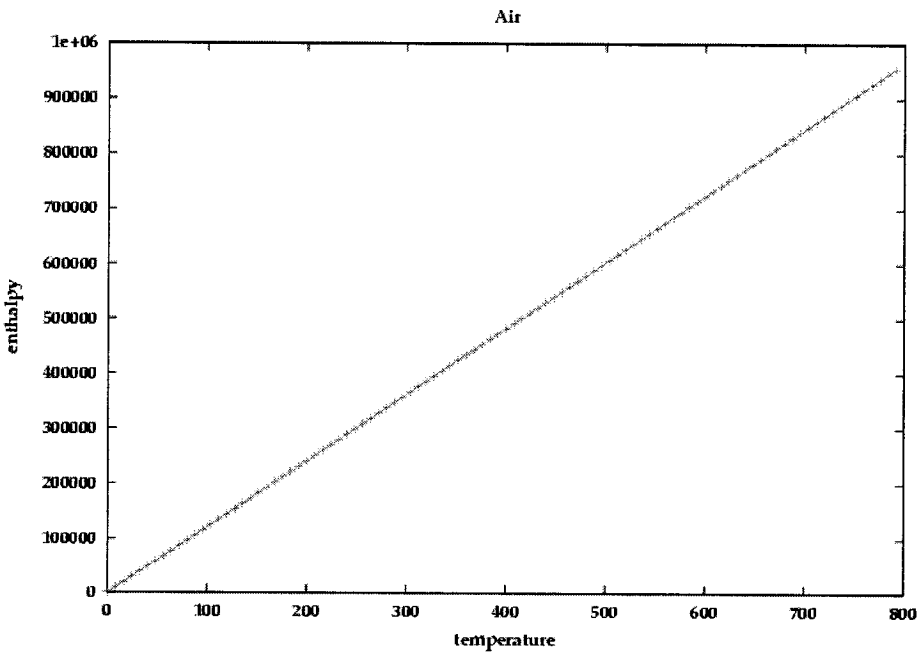

Figure 4.7: Enthalpy Relation for "Air"

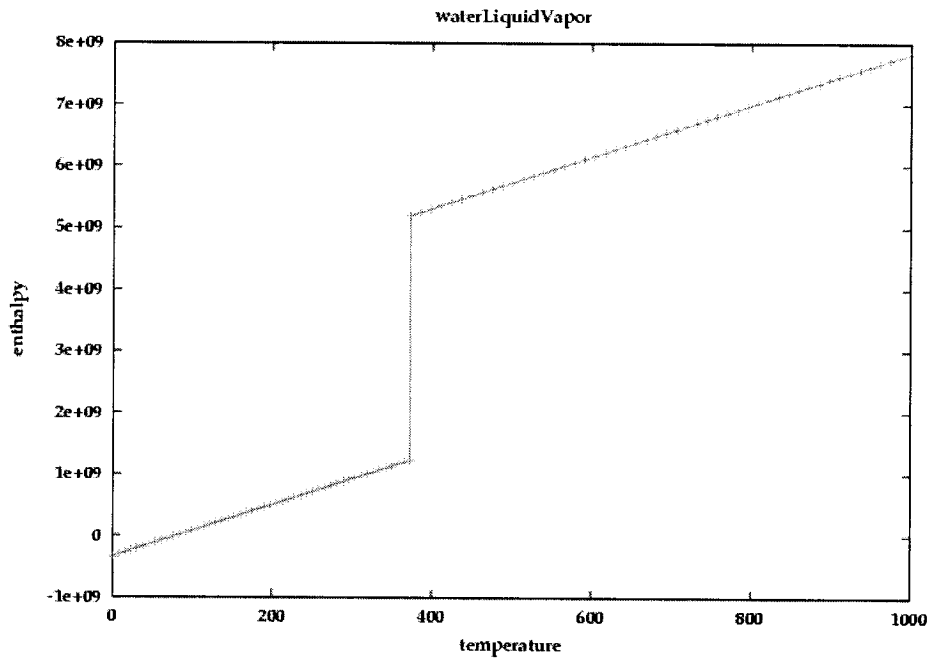

Figure 4.8: Enthalpy Relation for "WaterLiquidVapor"

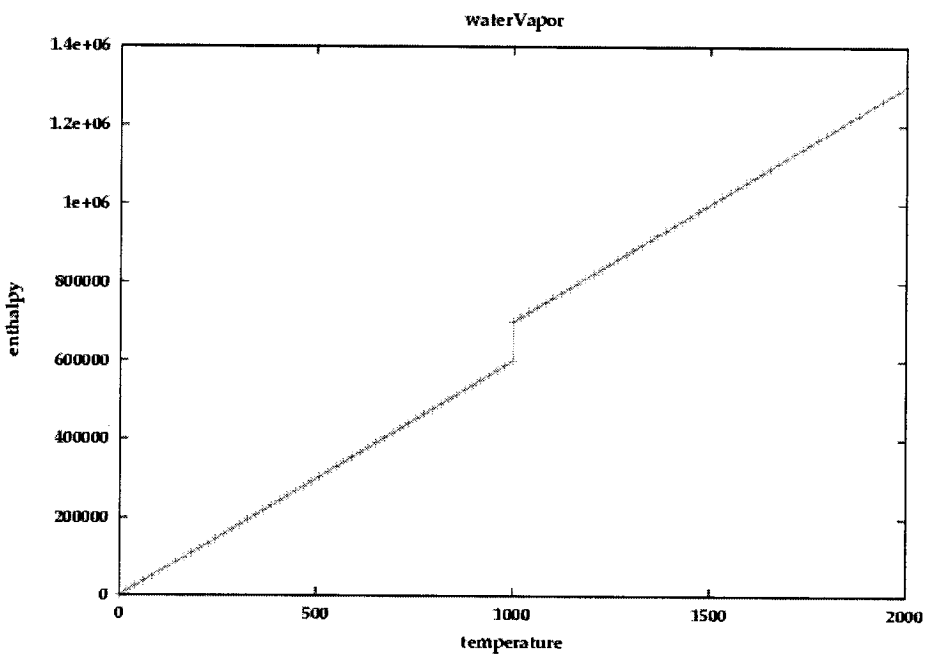

Figure 4.9: Enthalpy Relation for "WaterVapor"

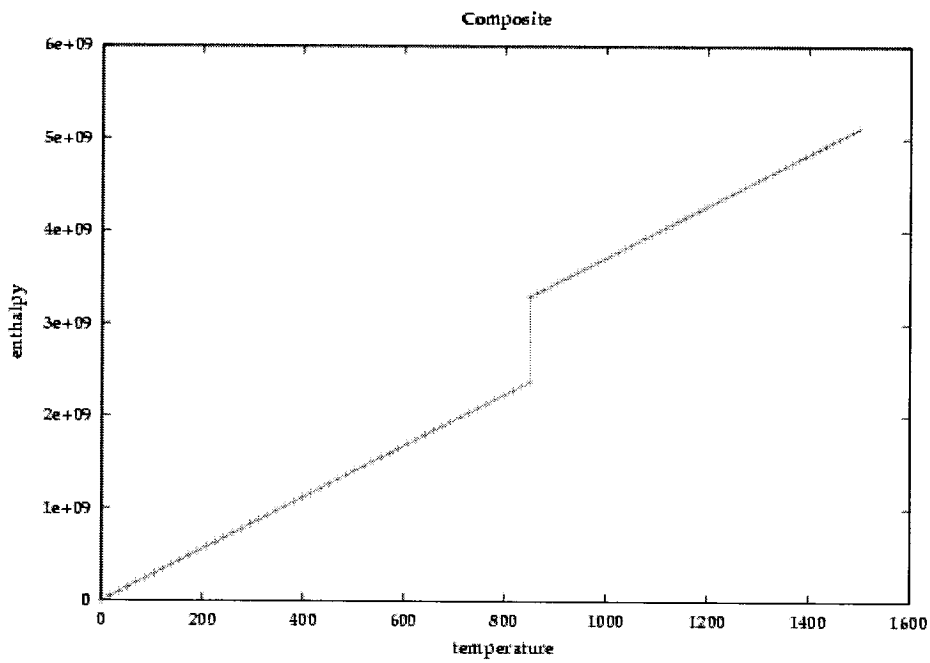

Figure 4.10: Enthalpy Relation for "Composite"

4.4.3 LHP Solver Parameters and Data Flow

The LHP was divided into domains to which individual solvers were applied. The Convection Diffusion solver was used to solve the temperature distribution and thermal fluxes within the LHP. The interface solver was then used to predict the evaporation of the working fluid at the interface between the evaporator vapour grooves and the outer surface of the wick. The interface solver computed the velocities of the vapour and liquid entering and exiting the interface. The Potential Flow solver was then used to predict the velocity of vapour as it travels through vapour grooves into the vapour line.

4.4.3.1 Convection Diffusion

The domain for the Convection Diffusion solver included the wick, evaporator casing and evaporator saddle. The condenser saddle, liquid and vapour line casings, as well as the working fluid were also included in the Convection-Diffusion domain.

Dirichlet (temperature) boundary conditions were applied to the Convection Diffusion model of the vapour. Temperatures of 20°C were constrained at the vapour-wall interfaces in the evaporator grooves.

A Neumann (heat flux) boundary condition was applied between the evaporator saddle and the outer casing of the evaporator to represent the heat applied by the payload (heater). The heat flux is defined as heat transfer per unit area between the applied components:

$$q'' = q / A \tag{4.32}$$

In order to simulate the ambient interactions between the liquid line and the surroundings, it was necessary to apply a convective boundary condition to the outer surface of the liquid line. Within the MMO framework, convective boundary conditions are applied as ambient temperature T_∞, and a constant convective heat transfer coefficient h_c. For the LHP model, a convective boundary condition was imposed between the liquid line and the surroundings assuming an ambient temperature of 20 °C. The convective coefficient was determined using a correlation for free convection from a horizontal cylinder in air at atmospheric pressure (Holman, 1997):

$$h_c = 1.32\left(\frac{\Delta T}{d}\right)^{\frac{1}{4}}$$

$$\Delta T = T_\infty - T_s \tag{4.33}$$

where:

h_c is the convective heat transfer coefficient in W/m^2 °C

d is the outer diameter of the liquid line

T_∞ is the assumed ambient temperature

T_s is the surface temperature of the liquid line

The temperature of the liquid line is unknown until after the solution, and the convective heat transfer coefficient is therefore a function of the solution. However, the coefficient must be input by the user before the solution process is begun. This difficulty was avoided by first running the Convection Diffusion solver on the domain without the convective boundary condition. The average liquid line temperature was then used to compute the convective heat transfer coefficient and the convective condition was then applied for a second iteration of the Convection Diffusion solver.

To simulate a sink for the LHP, the initial temperature of the condenser saddle was set to 0°C. An ambient temperature of 20 °C was assumed, and an initial temperature of 20°C was applied to all other components of the model. The initial velocity of all material points of the model was set to zero.

4.4.3.2 Interface

Within the present model, the liquid/vapour interfaces are assumed to be stationary, and are assigned assumed locations within the model. Four liquid/vapour interfaces were

created at the boundaries between the wick and the vapour grooves set in the evaporator casing. These four locations were treated as a single domain. The interface solver was applied to model the evaporation occurring at edge of the wick, and to calculate the liquid and vapour velocities of the fluid entering and exiting the interfaces.

As the interfaces are assumed to be stationary, the interface velocities were set to zero, and equations (4.20) and (4.21) become:

$$\overline{V}_L = \frac{\dot{m} \cdot \hat{n}}{\rho_L} \tag{4.34}$$

$$\overline{V}_G = \frac{\dot{m} \cdot \hat{n}}{\rho_G} \tag{4.35}$$

Because the thermal gradient in the vapour grooves was assumed to be small, the mass flow rate was determined as follows:

$$\dot{m} = \frac{q_L}{h_{fg}} \tag{4.36}$$

where q_L is the heat flux from the liquid side of the interface obtained during the Convection Diffusion solution process. This heat flux becomes the initial condition for the Interface solution process.

4.3.3.4 Potential Flow

The Potential Flow solver was used to predict the flow of vapour from the interface through the vapour grooves in the evaporator casing and into the vapour line.

Because the Laplace equation is parabolic, boundary conditions must be applied at all points on the boundary of the domain. A zero flux condition was applied everywhere between the vapour and walls, ensuring that the component of vapour velocity normal to the boundaries was zero. The Interface Solver predicted the velocity

of the vapour at the liquid-vapour interfaces in the evaporator grooves and these values were applied as a Neumann boundary condition in the Potential Flow domain. A potential (Dirichlet) condition must be applied to at least one node in the liquid-vapour interface to constrain the null space of the potential, and ensure a unique solution.

Although not required mathematically, initial conditions were applied to the Potential Flow solver. The initial velocity was set to zero, and the initial pressure was set to stagnation pressure.

4.3.3.5 Data Flow

The data flow for the solution of the evaporator is illustrated in Figure 4.11.

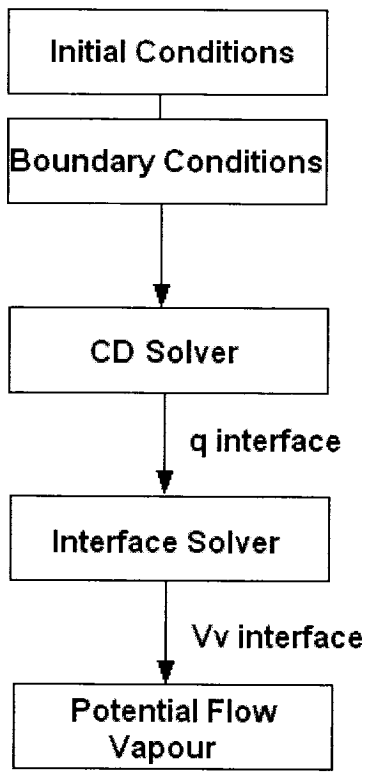

Figure 4.11: Data Flow Diagram for the Solvers in the Evaporator Model

4.4.4 Results

Convection Diffusion Results

A temperature distribution of the evaporator housing, wick, compensation chamber, fluid lines, saddles, as well as the working fluid was obtained from the Convection Diffusion solver. An initial solution showed an average liquid line temperature of approximately 23 °C. This value was used in equation (4.12) to obtain a convective heat transfer coefficient of 8.43 W/m^2 °C which was then applied to the model in the form a convective boundary condition on the outer surface of the liquid line. Figure 4.12 shows this predicted temperature distribution including the convective effect on the liquid line. In order to simulate payload heating, a heat flux was applied at the contact between the evaporator saddle and the evaporator casing; as a result this area possesses the highest temperature in Figure 4.12. A marked thermal gradient between the evaporator housing and the compensation chamber can be noted. This represents the conductive contribution of heat leak. As a Dirichlet condition was applied to the condenser saddle to simulate sink conditions, this area appears cold in the figure. Due to the applied convective boundary condition, the liquid line possesses less of a thermal gradient and is on average warmer than the vapour line. Because the initial condition for the velocity of the working fluid was zero, the thermal gradient visible in Figure 4.12 is due to conduction only, and no heat pipe effect is present.

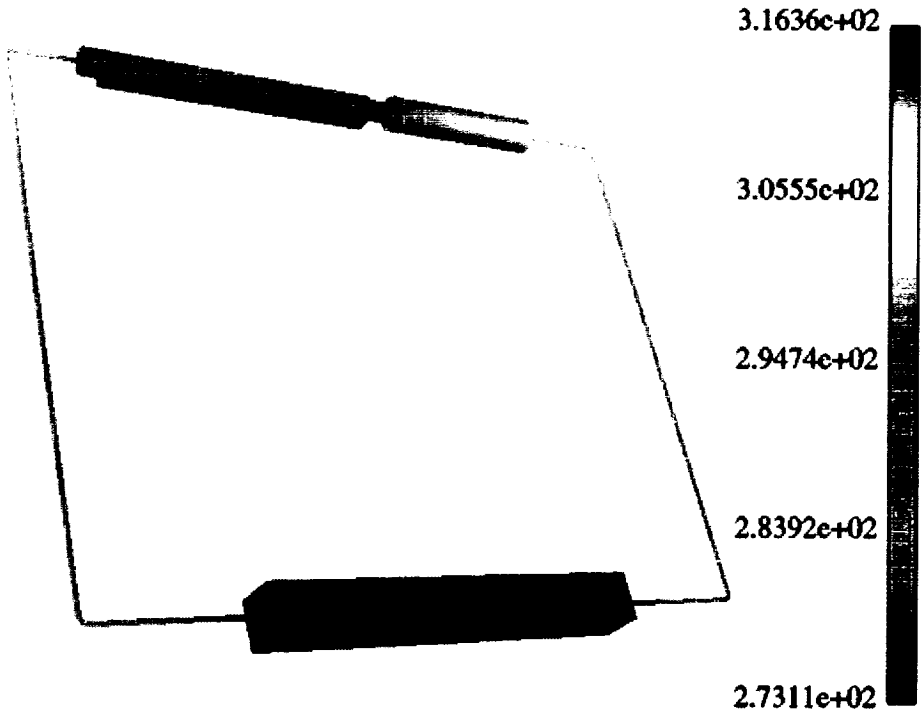

Figure 4.12: Predicted Temperature Distribution for the LHP [Temperature in K]

The temperature distribution within the evaporator section is best viewed in cross section. Figure 4.13 shows the predicted temperature distribution of the evaporator section of an xy cut plane located at z = -0.018 m. The hottest region is located at the contact between the evaporator housing and saddle. The visible cool patches reflect the Dirichlet constraints placed on the vapour in the vapour grooves.

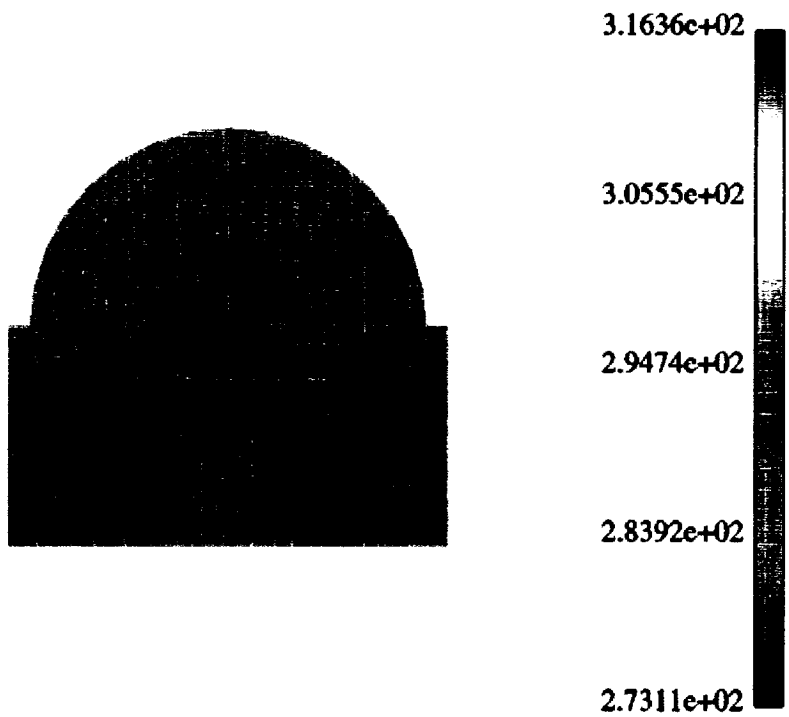

Figure 4.13: Predicted Temperature Distribution Evaporator xy Plane at z= 0.018 m [Temperature in K]

The Convection Diffusion solver also predicted heat flux distribution within the domain. Figure 4.14 shows the heat flux in the evaporator section on an xy cut plane located at z = - 0.018 m. Again, the area with the highest flux concentration is at the contact between the evaporator saddle and the evaporator housing. These heat flux values were supplied to the interface solver in order to model the mass flux across the liquid-vapour interfaces.

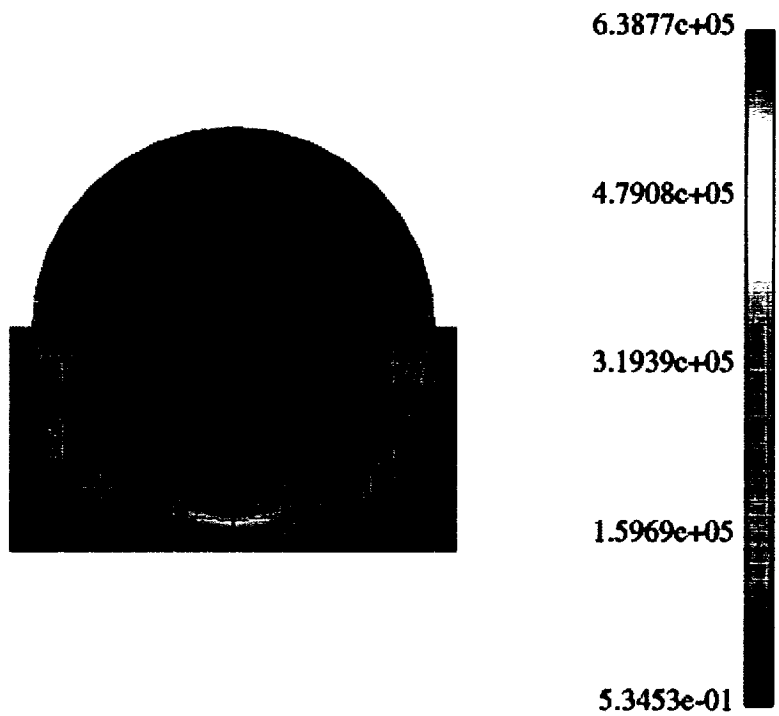

Figure 4.14: Predicted Heat Flux Evaporator Cross Section [Heat Flux in W/m2]

Interface Results

The interface solver was applied to the four liquid/vapour interfaces located at the boundaries between the wick and the vapour grooves set in the evaporator casing, and was used to obtain a mass flow rate across the interface.

The solver also predicted values for liquid and vapour velocities at the interface. Figure 4.15 shows the predicted values for vapour velocity at the four liquid-vapour interfaces. As previously discussed, the fluid velocities calculated by the interface solver are directly proportional to the heat flux. From Figure 4.15 it can be noted that the largest velocities occur in the lower interface situated closest to the evaporator saddle; while the lowest velocities occur in the upper interface situated furthest from the saddle.

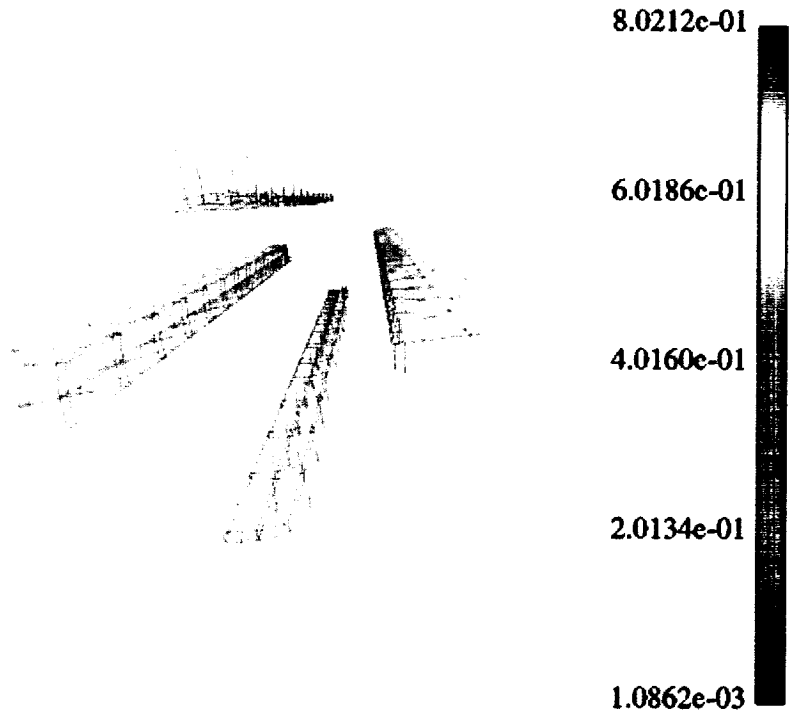

Figure 4.15: Vapour Velocity at Interface
[Velocity in m/s]

Potential Flow Results

The Potential Flow solver was used to predict the velocity and pressure distribution of the vapour inside the vapour grooves and at the entrance to the vapour line. Figure 4.16 illustrates the predicted vapour velocity within the domain. The radial velocity of the vapour entering the grooves from the interface, and the development of some axial velocities are apparent in this Figure.

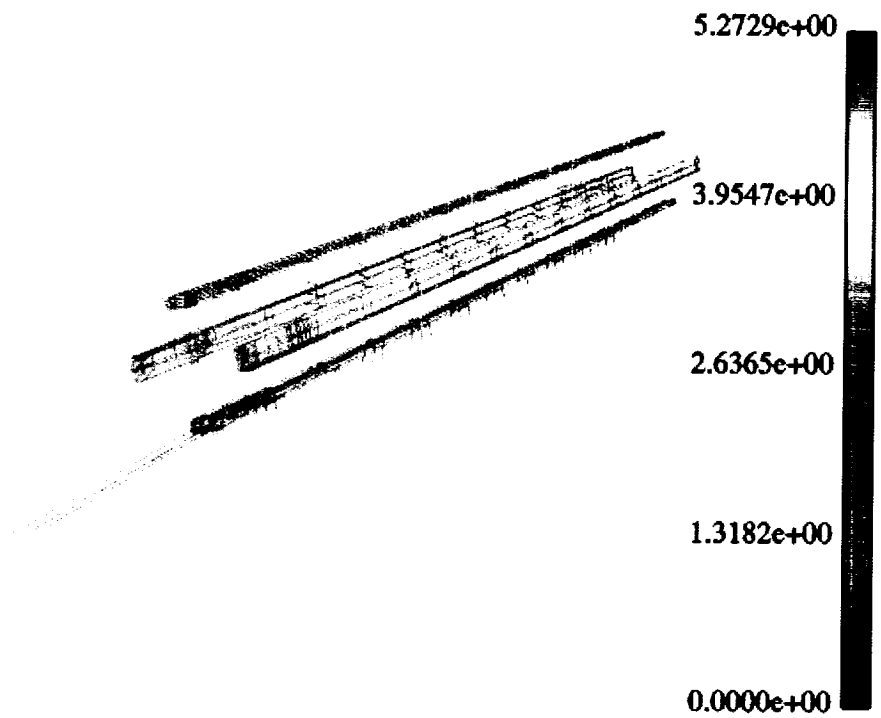

Figure 4.16: Vapour Velocity in Vapour Grooves and Vapour Line [Velocity in m/s]

Chapter 5

Conclusions and Recommendations

5.1 Conclusions

Performance Testing

An experimental investigation of LHP performance characteristics comprising of a series of tests conducted in ambient and vacuum environments was performed. The LHP operating characteristics during both steady-state and transient operation including start-up and constant power operation were examined. The LHP showed reliable start-up and steady operation at various heat loads in both ambient and vacuum environments. Power cycling was used to generate LHP performance curves, where operating temperature was plotted against applied power. The performance curves indicated that operating temperature increases with input power at high power loads, while at low power loads operating temperature decreases as input power is increased. This is consistent with the expected behavior of an LHP operating with a sink temperature lower than that of the

surroundings. The LHP operation was also examined for possible temperature hysteresis behaviors during large power changes. No such temperature hysteresis was observed in both ambient and vacuum conditions. The LHP showed reliable start-up in vacuum conditions. It was noted that at lower powers, a significantly longer time was required to initiate start-up during vacuum testing. This effect was likely caused by the presence of two-phase fluid in the evaporator core, resulting in a substantially higher heat transfer from the evaporator to the compensation chamber. In the vacuum environment, the effects of ambient interactions are eliminated and their effects on LHP performance was further examined by comparing data generated under similar conditions in each environment. It was observed that the ambient operational temperatures exceeded those observed in the vacuum environment lower powers; while at higher powers, vacuum operational temperatures exceeded those observed under ambient conditions. This was concluded to be caused by the absence of free convection mechanism in the vacuum case which heats/cools the LHP in the ambient case. The effective resistance of the LHP was defined as the ratio of the difference in average evaporator and average condenser temperature to the power applied to the evaporator. The effective resistance as a function of applied power was examined for each power cycle performed in both the ambient and vacuum environments. When this relation was examined for each power cycle, a clear exponential correlation was noted. Overall, the performance testing showed the LHP to reliable start-up and robust, stable operation with no temperature hysteresis effects during power cycling, proving the LHP to be a promising device for use in space craft thermal control.

Computational Modeling

A finite element numerical model for LHP simulation was developed at Carleton University using the existing MMO Framework platform. The task of numerically modeling LHPs presents considerable challenges including the modeling of two-phase flows with heat transfer and phase change in porous media. The phenomena associated with the operation of the LHP, such as the evaporation of the working fluid that provides the driving force for the operation of the loop, are largely concentrated within the evaporator section of the loop. Preliminary development of the computational LHP model described in this work therefore focused heavily on the description of the behavior and phenomena associated with the evaporator. The evaporator model described in this work constitutes the foundation for a future detailed LHP model.

Numerical modeling was performed using the MMO Framework, an in-house software platform that uses the finite element method to perform analyses of mechanical and aerospace engineering applications that involve coupled or non-coupled heat transfer, stress analysis, and fluid dynamics phenomena. The geometry and physical characteristics used in the numerical model were based on the manufacturer's specifications of the TAIS test unit used for the experimental potion of the work. Drawing heavily on the use of primitives, a mesh was generated to describe the geometry of the LHP. A material library was developed to describe the constituent materials of the test unit including the composite properties associated with the porous wick. Solver parameters were applied and a data flow scheme was developed for the solvers employed by the evaporator model. The Convection Diffusion solver was used to solve the

temperature distribution and thermal fluxes within the LHP. The Interface Solver was then used to predict the evaporation of the working fluid at the interface between the evaporator vapour grooves and the outer surface of the wick. The Interface Solver computed the velocities of the vapour and liquid entering and exiting the interface. The Potential Flow solver was then used to predict the velocity of vapour as it travels through vapour grooves into the vapour line. The numerical model of the evaporator was shown to be a promising foundation for further development of a computational LHP model.

5.2 Summary of Contributions

The objectives of this study were to gain an overall understanding of LHP technology as well as the ability to numerically simulate LHP behavior during normal operation. Three primary activities were targeted to achieve this goal: Establishment of and LHP laboratory, performance testing of a breadboard LHP, and the preliminary development of a computational LHP model. The following section summarizes the contributions made during the course of the project.

LHP Laboratory at Canadian Space Agency

After an initial assessment of the existing facilities at CSA, a test frame was designed to support the LHP during testing and to serve as an interface between the condenser saddle and the sink plate. A LabVIEW Virtual Instrument (VI) was created to support the data acquisition system and log the data. The VI also visualized the data in real-time plot to allow for the verification of start up and proper operation of the LHP during testing. Instrumentation for the tests was devised and thermocouples were applied to the surface of the LHP using Kapton and aluminum tapes. The test unit was installed

in the vacuum chamber prepared for ambient and vacuum testing using a vacuum rated epoxy and carbon gaskets in all joints between the test unit, saddles, and interface. Insulation and shielding were applied to the LHP for ambient and vacuum testing respectively. Integration of the LHP heater, power supply, chiller, vacuum chamber, and data acquisition was performed and verified prior to testing.

Performance Testing

A series of tests to investigate the performance characteristics of the LHP was developed; including detailed test and safety procedures. Testing of the breadboard LHP was performed in both ambient and thermal vacuum environments and sought to identify the critical performance issues including heat transport capabilities, unsteady heat transfer during power cycles, start-up transients, presence of hysteresis behaviors, and the effects of ambient interactions on LHP performance. The testing and data analysis was carried out over a period of six months.

Computational Modeling

A finite element numerical model for LHP simulation was developed at Carleton University using the existing MMO Framework platform. The creation of the LHP model involved three distinct processes. First a mesh was created to represent the LHP geometry. A material library was then created to describe the material properties of the constituent LHP parts, which were then linked to the LHP mesh. Finally, design files were created to define the solution strategy. These design files regulated the flow of data between the solvers and also contained the initial and boundary conditions to be applied during the solution process. Solutions were obtained for the LHP temperature

distribution due to conduction, the mass flux of vapour due to evaporation in the evaporator, as well as the velocity of vapour flowing through the evaporator grooves.

5.3 Recommendations for Future Work

There are several opportunities for future work in this project in each aspect of this project.

LHP Laboratory at Canadian Space Agency

The LHP laboratory is sufficient for various types of LHP testing however; several options exist for improvements in the test set-up. The present test interface does not allow for testing at various tilts and elevations. If the effect of gravity on LHP performance is to be examined a new test frame will need to be designed and manufactured. The current power supply used to support the evaporator heater possesses a GPIB interface. There is therefore an opportunity to automate the test processes through modification of the existing support software using LabVIEW.

Performance Testing

The experimental investigation performed in this work examined the LHP performance in the broad sense; further detailed testing could therefore be performed in a number of areas. Because spacecraft heat loads can vary due to fluctuating payload power dissipations, experiments involving periodical heating would be of particular interest. An in depth examination of the transients associated with start-up and power cycling, as well as the active control measures associated with them would also be of interest. The effects of gravity and sink temperature on LHP performance might also be investigated.

Computational Modeling

The numerical work presented in this study represents a foundation for the creation of a future detailed LHP model. The solution domain will eventually be expanded to include the rest of the LHP geometry including the condenser, liquid line, and compensation chamber. This would also require the modeling of the liquid-vapour interfaces within the condenser and the compensation chamber, and the solution of Darcy Flow to model the passage of liquid through the wick.

Upon completion of the initial LHP model, several geometric updates can be made; for example, the secondary wick might be included in later models. Also the condition of the working fluid in the compensation chamber and evaporator core may eventually become a function of the solution rather than a user defined input.

The solvers used in the model will also increase in complexity as the project progresses. The Interface solver will be altered to include the heat flux from both sides of the interface in order to produce a better prediction of the mass flux across the interface. The interface will also eventually be able to predict and track moving interfaces. This will allow for a far more accurate LHP model, particularly in the modeling of the condenser section. Presently, a Potential Flow model was used to solve the liquid and vapour in the domain; and the fluid was therefore implicitly assumed to be inviscid, irrotational, and incompressible. Future models may incorporate viscous effects by employing a Navier Stokes solver to model the working fluid. Finally, if the LHP is to be readily used in spacecraft thermal control, a reliable means of numerically modeling these devices is required. The ultimate goal of any LHP modeling effort will therefore be experimental validation.

References

Bai, L. (2004). *The FEM analysis of a heat pipe,* MASc Thesis, Carleton University.

Baturkin, V., Friedrichson, Yu., Khmelev, Yu., and Zhuk, S. (2002). Experimental Results on Heat Transfer Phenomena in a Miniature Loop Heat Pipe with a Flat Evaporator. *12th International Heat Pipe Conference*, Moscow, Russia, May, National Aerospace Library, No. NLR-TP-2002-73.

Chi, S. W., (1976). *Heat Pipe Theory and Practice: A Sourcebook.* New York: McGraw-Hill.

Cullimore, B., and Baumann, J. (2000). Steady State and Transient Loop Heat Pipe Modeling. *30th International Conference on Environmental Systems*, Toulouse, France, July, Society of Automotive Engineers, No. 2000-001-2316

Cullimore, B., and Johnson, D.A. (2003). Adding Heat Pipes and Coolant Loop Models to Finite Element and/or Finite Difference Thermal/Structural Models. *33rd International Conference on Environmental Systems*, Vancouver, Canada, July, Society of Automotive Engineers, No. 2003-01-2663.

Delil, A.A.M., and Baturkin, V. (2002). Modeling of a Miniature Loop Heat Pipe With a Flat Evaporator. *32nd International Conference on Environmental Systems*, San Antonio, USA, July, Society of Automotive Engineers, No. 2002-01-2506.

Dickey, J.T., and Peterson, G.P., (1994). An Experimental and Analytical Investigation of the Operational Characteristics of a Capillary Pumped Loop, *Journal of Thermophysics and Heat Transfer*, Vol. 8, No. 3, pp. 602 – 607.

Goldak, J. (2003). Lecture Notes, Finite Element Method II, Carleton University.

Hoang, T.T., and Kaya, T. (1999). Mathematical Modeling of Loop Heat Pipes with Two-phase Pressure Drop. *33rd Thermophysics Conference,* Norfolk, U.S.A, 28 June – 1 July, American Institute of Aeronautics and Astronautics.

Holman, J.P. (1997). *Heat Transfer*, McGraw-Hill, 1997.

Kaya, T., and Ku, J. (2003). Thermal Operational Characteristics of a Small-Loop Heat Pipe, *Journal of Thermophysics and Heat Transfer*, Vol. 17, No. 4, pp. 464 – 470.

Kaya, T., and Ku, J. (1999). Investigation of the Temperature Hysteresis Phenomenon of a Loop Heat Pipe. *33rd National Heat Transfer Conference*, Albuquerque, USA, August, Society of Automotive Engineers.

Ku, J. (1999). Operating Characteristics of Loop Heat Pipes. *29th International Conference On Environmental Systems*, Denver, USA, July, Society of Automotive Engineers, No. 1999-01-2007.

Lashley, C., Krein, S., and Barcomb, P. (1998). Deployable Radiators – a Multi-Discipline Approach. *29th International Conference on Environmental Systems*, Denver, USA, July, Society of Automotive Engineers, No. 981691.

Lewis, R.W., Morgan, K. (1996). *The Finite Element Method in Heat Transfer Analysis*, New York: John Wiley and Sons.

Lin, L., Ponnappan, R., and Leland, J. (2002). High Performance Miniature Heat Pipe, *International Journal of Mass and Heat Transfer*, Vol. 45, pp. 3131-3142.

Maidanik, Y.F., Vershinin, S., Kholodov, and Dolggirev, J. (1985). Heat Transfer Apparatus, U.S. Patent 4515209.

Maidanik, Y.F., Fershtater, Y.G., and Goncharov, K.A. (1991). Capillary Pumped Loop for the Systems of Thermal Regulation of Spacecraft. *Proceedings of the 4th European Symposium of Environmental Space and Control Systems*, ESA SP-324.

Maidanik, Y.F., Fershtater, Y.G., and Solodovnik, N.N. (1994). Design and Investigation of Methods of Regulation of Loop Heat Pipes for Terrestrial and Space Applications, Society of Automotive Engineers, No. 941407.

Nikitkin, N., and Cullimore, B. (1998). CPL and LHP Technologies: What are the Differences, What are the Similarities? *28th International Conference on Environmental Systems,* Danvers, USA, July, Society of Automotive Engineers, No. 981587.

Pastukhov, V.G., Maidanik, Y.F., and Chernyshova, M.A. (1999). Development and Investigation of Miniature Loop Heat Pipes. *29th International Conference on Environmental Systems,* Denver, USA, July, Society of Automotive Engineers, No. 1999-01-1983.

Pastukhov, V.G., Maidanik, Y.F., Vershinin, C.V., and Korukov, M.A. (2003). Miniature Loop Heat Pipes for Electronics Cooling, *Applied Thermal Engineering*, Vol. 23, pp. 1125 – 1135.

Wang, B. (2001). *Prediction of Low Cycle Fatigue for Die Casting With FEM,* MEng thesis, Carleton University, Ottawa, Canada.

Wirsch, P.J., and Thomas, S.K. (1996). Performance Characteristics of a Stainless Steel/Ammonia Loop Heat Pipe, *Journal of Thermophysics and Heat Transfer*, Vol. 10, No. 3, pp. 326 – 333.

Wrenn, K.R., and Krein, S.J. (1999). Verification of a Transient Loop Heat Pipe Model. *29th International Conference on Environmental Systems,* Denver, USA, July, Society of Automotive Engineers, No. 1999-01-2010.